THE $(n,n'\gamma)$ REACTION

A STUDY OF
THE $(n,n'\gamma)$ REACTION
USING FISSION NEUTRONS

by

LIONEL WILLIAM NICHOL, B.A.

A Thesis

Submitted to the Faculty of Graduate Studies

in Partial Fulfilment of the Requirements

for the Degree

Doctor of Philosophy

McMaster University

May, 1971

DOCTOR OF PHILOSOPHY (1971)
(Physics)

McMASTER UNIVERSITY
Hamilton, Ontario.

TITLE: A Study of the (n,n'γ) Reaction Using Fission Neutrons

AUTHOR: Lionel William Nichol, B.A. (McMaster University)

SUPERVISOR: Dr. T. J. Kennett

NUMBER OF PAGES: ix , 118

SCOPE AND CONTENTS:

The total cross section of the (n,n'γ) reaction for each level of various nuclides (^{11}B, ^{14}N, ^{19}F, ^{23}Na, ^{27}Al, ^{28}Si, ^{31}P, and ^{40}Ca) was studied using a fission source of neutrons. The gamma ray spectra were obtained using a Ge(Li)-NaI annulus multiple spectrometer system. A model based on the Hauser Feshbach formalism was used to predict spins and parities of various levels. A model was derived to explain Doppler broadening effects and was used to measure stopping powers of various media and lifetimes of several states in ^{19}F.

ACKNOWLEDGEMENTS

I wish to express my appreciation to my Research Director, Dr. T. J. Kennett, who provided guidance, insight and encouragement during the course of this work. To the other members of my supervisory committee, Dr. W. V. Prestwich and Dr. K. Fritze, I also wish to express my gratitude for their helpful criticism.

Numerous members of the neutron capture gamma ray group provided valuable assistance at various times during the course of this work. In particular, I wish to thank A. H. Colenbrander for his computer programs and assistance which was invaluable in handling the large amount of data involved.

The assistance given by P. Ernst, Dr. H. Brunnader and J. MacDougall of the McMaster Reactor staff was of great value during the design and construction of the tangential irradiation facility used in this work.

To my family, I owe a special thanks for their understanding and patience during my years of study at university.

Gratitude must also be expressed to the Ontario Provincial Government and the National Research Council for their financial support.

TABLE OF CONTENTS

		Page
CHAPTER 1 -	INTRODUCTION	1
1-1	Reaction Mechanism	1
1-2	Optical Model	5
1-3	Hauser Feshbach Theory	7
1-4	Previous Work	10
CHAPTER 2 -	EXPERIMENTAL FACILITIES	15
2-1	Reactor Facility	15
2-2	Tangential Irradiation Facility Versus A Beam Port Facility	17
2-3	Description of Tangential Irradiation Facility	18
2-4	Neutron Flux Measurements and System Sensitivity	24
2-5	The Ge(Li) Detector	28
2-6	NaI Split Annulus Detection System	32
2-7	Performance of Tangential Irradiation Facility	38
2-8	Doppler Broadening Effects	42
2-9	Sample Position and Energy Shift	46
2-10	Sample Form	50
CHAPTER 3 -	TYPICAL HAUSER FESHBACH CALCULATIONS	51
3-1	Introduction	51
3-2	Predicted Population Values for ^{28}Si	53
3-3	Experimental Data Handling	57
3-4	^{28}Si Results	59
3-5	Non-zero Ground State Spin Cases	63
CHAPTER 4 -	RESULTS OF CROSS SECTION MEASUREMENTS	65
4-1	Calcium Results	66
4-2	Phosphorus Results	70
4-3	Aluminum Results	76
4-4	Sodium Results	84
4-5	Fluorine Results	90
4-6	Nitrogen Results	94
4-7	Boron Results	98
CHAPTER 5 -	STOPPING POWER CALCULATIONS	103
5-1	Introduction	103
5-2	Experimental Results	106
5-3	Discussion of Stopping Power Results	109

CHAPTER 6 - DISCUSSION OF RESULTS

6-1 General Conclusions 110
6-2 Limitations of the Experiment 111

REFERENCES 114

LIST OF TABLES

Number	Title	Page
2-1	System Background	41
3-1	Neutron Angular Momenta for a 0+ to 2+ Excitation	54
3-2	Gamma Rays Produced by the $^{28}Si(n,n'\gamma)^{28}Si$ Reaction	61
3-3	Branching Ratios for ^{28}Si Levels	61
3-4	Experimental Population Values and Hauser Feshbach Results for ^{28}Si	62
3-5	Formation of Intermediate State Spins in Aluminum	64
4-1A	Gamma Rays Produced by the $^{40}Ca(n,n'\gamma)^{40}Ca$ Reaction	67
4-1B	Branching Ratios for ^{40}Ca Levels	68
4-1C	Experimental Population Values and Calculated Values for ^{40}Ca	69
4-2A	Gamma Rays Produced by the $^{31}P(n,n'\gamma)^{31}P$ Reaction	72
4-2B	Branching Ratios for ^{31}P Levels	73
4-2C	Experimental Population Values and Calculated Values for ^{31}P	74
4-3A	Gamma Rays Produced by the $^{27}Al(n,n'\gamma)^{27}Al$ Reaction	79
4-3B	Branching Ratios for ^{27}Al Levels	80
4-3C	Experimental Population Values and Calculated Values for ^{27}Al	81
4-4A	Gamma Rays Produced by the $^{23}Na(n,n'\gamma)^{23}Na$ Reaction	85
4-4B	Branching Ratios for ^{23}Na Levels	86
4-4C	Experimental Population Values and Calculated Values for ^{23}Na	87
4-5A	Gamma Rays Produced by the $^{19}F(n,n'\gamma)^{19}F$ Reaction	91
4-5B	Branching Ratios for ^{19}F Levels	91
4-5C	Experimental Population Values and Calculated Values for ^{19}F	92
4-6A	Gamma Rays Produced by the $^{14}N(n,n'\gamma)^{14}N$ Reaction	95
4-6B	Branching Ratios for ^{14}N Levels	96
4-6C	Experimental Population Values and Calculated Values for ^{14}N	97
4-7A	Gamma Rays Produced by the $^{11}B(n,n'\gamma)^{11}B$ Reaction	99

Number	Title	Page
4-7B	Branching Ratios for ^{11}B Levels	99
4-7C	Experimental Population Values and Calculated Values for ^{11}B	101
5-1	Stopping Power Results	107
5-2	Lifetime Measurements	108
6-1	Comparison of Calculated and Experimental Population Values	110

LIST OF ILLUSTRATIONS

Figure No.	Caption	Following Page Number
2-1	The Physical Arrangement of the Through Tube Facility	15
2-2	Neutron Flux Distribution	16
2-3	Alignment of Collimation System	21
2-4	Capture Rate Reduction using Boron Filter	24
2-5	Effect of Filters on Neutron Flux	24
2-6	Neutron Flux Distribution	25
2-7	A Schematic Representation of the Electronic Logic and Linear Circuits Used for the Detection System	29
2-8	A Typical Ge(Li) Detector Response	31
2-9	Detection System	33
2-10	NaI Annulus Count Rate	34
2-11	Detector Response to ^{22}Na	35
2-12	Response of Detection System to Thorium	36
2-13	Pair Response Spectrum of $^{14}N(n,\gamma)^{15}N$	38
2-14	Pair and Photoefficiency of the Ge(Li) Detectors	39
2-15	System Background	40
2-16	Portions of the Aluminum Spectrum Expanded	42
2-17	Doppler Broadening	46
2-18	Singles Mode Spectrum for an Aluminum Sample	47
2-19	Pair Mode Spectrum for an Aluminum Sample	47
2-20	Algebraic Difference of Singles Spectra in Figure 2-18	48
2-21	Energy Shift due to Doppler Effects	49
3-1	The Calculated Cross Section (A) and Rate(B) Versus Energy for the 2+, 1778 keV Level in ^{28}Si	55
3-2	The Calculated Cross Section (A) and Rate(B) for Various Choices of Spin, Versus Energy for the 1778 keV Level in ^{28}Si	56
3-3	The Calculated Cross Section (A) and Rate (B) for Typical Higher Energy Levels in ^{28}Si	56
3-4	^{28}Si Decay Scheme	59
3-5	Calculated Cross Section Versus Energy for the 845 keV Level in Aluminum	64
4-1	^{40}Ca Decay Scheme	67
4-2	^{31}P Decay Scheme	71
4-3A	^{27}Al Decay Scheme	78
4-3B	^{27}Mg Contribution to ^{27}Al Spectrum	83
4-3C	35 keV Aluminum Resonance Reaction	83

4-4	^{23}Na Decay Scheme	84
4-5	^{19}F Decay Scheme	90
4-6	^{14}N Decay Scheme	95
4-7	^{11}B Decay Scheme	99
5-1	$F = 1 - \frac{1}{\beta} + \frac{1}{\beta}\exp(-\beta)$	105
5-2	Peak Shape	107
5-3	Detector Resolution Versus Energy	107

CHAPTER I

INTRODUCTION

When neutrons of moderate energy interact with complex nuclei, one of the chief reactions which occurs is the $(n,n'\gamma)$ reaction. This reaction is of interest because of the information it gives concerning the target nucleus. The reaction also can be used to study the scattering mechanism itself and the optical model. For moderate neutron energies, up to 10 MeV, the total cross section as well as the energy and angular distribution of the emitted neutrons is sensitive to the energy, angular momentum and parity differences which occur between the ground state and the excited levels of the target nucleus.

1-1 Reaction Mechanism

Inelastic scattering processes have been explained in the past by two different mechanisms. In a compound nucleus type reaction an incident particle (neutron) is absorbed into a target nucleus and remains for an appreciable amount of time (10^{-16} sec), while many interactions are taking place. Then, a particle may be emitted in a manner independent of the mode of formation of the compound state. In a direct reaction process, an incident particle interacts with one or a few surface nucleons in the target nucleus for a short period

of time (10^{-22} sec) and a particle is emitted.

In 1949, Mayer[1] proposed the basis for the shell model or single particle model. In this model it is assumed that the nucleons form closed shells similar to the atomic case and that the nuclear properties are determined by the nucleons outside the last closed shell. The model also predicts that the effect of the closed shells can be represented by a potential well. This model cast some doubt on the validity of the compound nucleus idea which proposed that the incident energy was shared among the nucleons in the target. In 1954, Feshbach et al[2] introduced the basis for the optical model. This model predicts that a nucleon can enter a nucleus and move within the nucleus without forming a compound state. The target nucleus acts as a potential well for the nucleon. The formation of a compound state occurs with a probability less than unity. Hence, the effect of the nucleus is to act as a potential well with absorption and reflection or scattering of the incident particle in a nuclear reaction. The model can not predict any resonance phenomena and thus can only be used after averaging over many resonances of the compound or intermediate state of the reaction.

The statistical model was founded in the late 1930's and was developed extensively by Weisskopf[3] and his group. The model is based upon three assumptions, namely

1) The Bohr picture of a compound nucleus reaction holds.
2) The spread in energy of the incident particles is sufficiently high, and at the energy of the incident particles the density of levels of the target nucleus is also sufficiently high so that levels of all spins and parities are available. If this is true, then a statistical average is obtained over all possible states.
3) The decay of the compound state is independent of the mode of its formation. This allows the cross section of the reaction to be written as the product of two terms, namely the formation of the compound state of a given spin and parity times the relative probability of decay to a given level.

Inelastic scattering may be treated by two approaches. one is the direct reaction approach and the other is the Hauser-Feshbach[4] approach which is based on the statistical model. Many experiments have been performed to determine which model is the one to use for inelastic scattering. The general trend seems to indicate that at energies up to approximately 6 MeV the statistical model is best and at higher energy the direct reaction model works better. Thus it is probable that neither model is exact but rather both have some validity. The two models have not been tested to any great extent in the energy range 5-10 MeV. For the $(n,n'\gamma)$, (n,p) and (n,α) reactions the statistical model has been used extensively. Marion[5] has published a book

describing the results of these experiments up to 1965. The proceedings of two conferences [6,7] held in 1963 and 1965 concerning neutron physics provide a summary of numerous inelastic neutron scattering experiments.

The compound nucleus reaction can be separated from the direct reaction by means of the lifetime or width of the state. A more practical approach has been to study the angular distribution of the disintegration products. The compound nucleus model predicts symmetry about 90° for the distribution, while the direct reaction model predicts the distribution will be peaked in the forward direction according to the square of the spherical Bessel function. The compound nucleus model also predicts that the cross section for a particular level will decrease with energy as more energy levels are involved since the levels compete for the decay mode. The direct reaction model does not predict this.

In this work the Hauser-Feshbach theory is used to predict the total cross section for the levels in the $(n,n'\gamma)$ reaction. The theory uses the statistical model and the optical model, described in the next section. The optical model is used to calculate the neutron transmission coefficients which in turn are needed to find the probability of forming a compound state and also the relative probability of a given decay mode.

1-2 Optical Model

The first form of the optical model[8] used a complex square well potential

$$V(r) = V + i.W,$$

where V and W were initially treated as constants. The imaginary part of the potential describes inelastic processes permitted by the Pauli principle and the law of conservation of energy. One solves the Schrodinger equation using this potential to obtain the scattering and reaction cross sections. At low energies, later authors made the real part of the potential similar to the potential used in the shell model. The basic square well potential gives too large a cross section for elastic scattering in backward directions and too small a cross section for compound nucleus formation[9].

In 1955, Woods and Saxon[10] replaced the square well potential with the following one

$$V(r) = \frac{-(V + i.W)}{1 + \exp((r-R)/a)} ,$$

where V is the depth of the potential well, W is the nuclear absorption parameter, R is the nuclear radius, "a" is a parameter determining the diffuseness of the well and "r" is the radial distance to the center of the well. This smoothed out potential was used by Beyster[11] in 1956 to generate a set of neutron transmission coefficients. Although this form of the potential predicts the experimental

results reasonable well, other corrections have been added in recent years to allow for spin-orbit coupling, different effects due to different energy regions of the reaction and various other corrections.

The two forms of the optical model potential used in this work were derived by Bjorklund and Fernbach[12] (B&F) and by Perey and Buck[13] (P&B). Both use a potential whose real part is of the Wood-Saxon form namely

$$V_R(r) = \frac{-V}{1 + \exp((r-R)/a)} ,$$

and a spin-orbit term of the Thomas form

$$V_S(r) = -V_S.(\hbar/\mu c)^2.(1/r).\frac{d}{dr}\left(\frac{-1}{1 + \exp((r-R)/a)}\right).(\bar{l}.\bar{\sigma}),$$

where V_S is a constant, μ is the pion mass, $\bar{l}$ is the angular momentum of the neutron with respect to the nucleus and $\bar{\sigma}$ is the spin of the neutron. Both potentials use a surface imaginary term but the forms are different. The radial dependence of the potential uses the Thomas-Fermi[14] approximation which assumes that a Fermi energy can be defined as a function of nucleon density and hence of radial position. The Pauli principle implies that the imaginary part of the potential is not proportional to the nucleon density but decreases more slowly giving a maximum value at the nuclear surface. At higher incident energies the effect of this surface absorption decreases. The B&F work uses a Gaussian surface term, namely

$$V_I^G(r) = -i.W.\exp-((r-R)/b)^2,$$

while the P&B work uses a derivative Wood-Saxon form

$$V_I^D(r) = -i.W.4.b.\ \frac{d}{dr}\left(\frac{-1}{1 + \exp((r-R)/b)}\right),$$

where b is a measure of the diffuseness of this term. In addition to the potential given, the theory of P&B assumes that a nonlocal optical model is required. This means that the Schrodinger equation in their case has the following form

$$-\frac{\hbar^2}{2m}\nabla^2\Psi(r) + V.\Psi(r) = E.\Psi(r).$$

The nonlocal potential V has the following form

$$V.\Psi(r) = \int V(r,r').\Psi(r').dr'$$

with $V(r,r') = V(r',r)$

and $V(r,r') = U(p).H(|r-r'|)$

where $H(|r-r'|) = \dfrac{\exp-((r-r')/\ )^2}{\pi^{3/2}.\beta^3}$

$$U(p) = V_I^D(p) + V_R(p) + V_S(p)$$

$$P = 1/2(|r + r'|).$$

β gives the range of the nonlocality. These potentials were used to generate the neutron transmission coefficients used in the Hauser-Feshbach calculations.

1-3 Hauser-Feshbach Theory

It is reasonable to assume that at the excitation energy of the compound nucleus, the density and widths of levels are such that a range of spins and parities can occur for the intermediate state. The wave functions for the process can be assumed to have random phases so that if phase averages are performed then all interference terms will vanish. It is possible to treat the reaction in two separate steps,

namely the formation of a compound or intermediate state, and secondly the decay of the state. The competition arising from gamma ray emission and charged particle emission will be neglected in this work. Typical cross sections for aluminum reactions[15] with fast neutrons (~2 MeV) are

(n,p) 0.03 barns
(n,α) 0.001
(n,γ) 0.00005
(n,n'γ) 0.8

Aluminum has a large (n,p) cross section; but even it is more than 20 times less probable than the (n,n'γ) reaction.

The cross section for the formation of the compound state is given by

$$\sigma = (2\ell + 1)\pi \lambda\!\!\!^{-2} \cdot T^{J}_{\alpha j \ell}(E),$$

where $T^{J}_{\alpha j \ell}(E)$ represents the fraction of the neutrons with spin j and angular momentum ℓ which strike the nucleus and form a compound state. J gives the value of the resultant spin of the nucleus and α indicates the channel. α indicates which level is involved in the reaction. $\lambda\!\!\!^{-}$ is the neutron wave number. The values of the penetrabilities $T^{J}_{\alpha j \ell}(E)$ are obtained from a table[16] based on optical model calculations. The probability of forming a compound nucleus state of spin J is the above probability times the square of the Clebsch-Gordon coefficient, which gives the probability of forming the spin J given the spins of the target and incident neutron. To obtain the total cross section for inelastic scattering to a given level in the target nucleus, one multiplies the above

term by the relative probability for this particular decay mode. In other words the various levels compete for the available neutrons. Thus the cross section[17] is given by

$$\sigma(\alpha|\alpha') = \pi\lambda^2 \sum_{\substack{J \\ j\ell \\ j'\ell'}} \frac{(2J+1)}{2(2I+1)} \cdot T^J_{j\ell} \cdot \frac{T^J_{\alpha' j'\ell'}}{\sum_{\alpha'' j''\ell''} T^J_{\alpha'' j''\ell''}} ,$$

where I is the spin of the target nucleus, i is the spin of the incident particle, ℓ is the orbital angular momentum of the incident particle, j is the channel spin defined by

$$j = I + i,$$

α is the channel designation and includes energy of initial particle and indicates which level is excited. Primed quantities indicate values after the reaction. The sums in this equation are restricted by the conservation of energy and parity. Conservation of angular momenta and the definition of channel spin requires that

$$|J-\ell| \leq j \leq (J+\ell), \qquad |I-i| \leq j \leq (I+i),$$

$$|J-\ell'| \leq j \leq (J+\ell'), \quad \text{and} \quad |I'-i'| \leq j \leq (I'+i').$$

The double primed sum is a sum over all possible ways for the compound state to decay including the decay of interest. The penetrabilities with a single prime are summed over all possible ways of decaying to the level of interest, and the penetrabilities with no primes are sumed over all possible ways of forming the intermediate state J. J is sumed over all possible values allowed by the conservation laws. The factor (2J+1)/(2I+1) is a statistical weight factor and occurs as a result of averaging and manipulating over

angular momenta.

The equation giving the cross section was first derived by Hauser and Feshbach[18] and also by Wolfstein[19]. Later derivations have been given by Feld *et al*[20], Lane and Thomas[21] and by Feshbach[21].

1-4 Previous Work

One of the earliest measurements of the energy and angular distributions of an (n,n'γ) reaction was done by O'Neil[22] in 1954. His experiment used time of flight techniques to study the neutrons scattered from C, Al, Cu, Sb, and Pb using neutrons produced by a 14.8 MeV neutron generator. His equipment allowed him to study scattered neutrons up to 4 MeV in energy and his results indicated isotropic scattering. The time of flight technique has continued to be developed to study the emitted neutrons, by numerous authors such as Towle and Owens[23] who have studied ^{23}Na and ^{27}Al targets. One of the first experiments which contradicted the compound nucleus model approach was done by Rosen and Stewart[24] in 1955. They used nuclear emulsions to detect scattered neutrons produced by a 14 MeV neutron generator. Their work suggested that the compound nucleus model worked up to approximately 6 MeV and above this energy the angular distribution was peaked in the forward direction. Since 1960, various experimenters such as Mathur *et al*[25] have successfully used the Satchler[26]

formalism which is based on the Hauser Feshbach model to explain angular distributions for the (n,n'γ) reaction.

The theory of Hauser and Feshbach is based on the assumption that there is no interference between different angular momentum channels and that the mode of decay is independent of the mode of formation of the compound state. About 1956, Lane and Lynn[27] and also Dresner [28] assumed that the level widths have a Porter-Thomas[29] distribution with the result that the cross section becomes

$$\sigma = \sigma(HF) \cdot W,$$

where $\sigma(HF)$ is the cross section calculated by the Hauser Feshbach model and W is a correction factor. Moldauer[30] has evaluated W and has found that it varies from 0.50 near threshold to 1.0 for higher energy incident particles.

Numerous experimenters have attempted to test this modified form of the Hauser Feshbach theory. Torop[31] studied the angular distribution of gamma rays following inelastic neutron scattering on iron and cerium. Protons from the Stanford 3 MeV Van de Graaff accelerator were used to produce neutrons by the $^{3}H(p,n)$ reaction. His work showed that effects of the Porter-Thomas fluctuations on angular distributions were of the same order of uncertainty introduced by using different transmission coefficients and as a result he was unable to verify that the fluctuations

exist. A number of experimenters[32,33,34] at the Texas Nuclear Corporation have studied the angular distributions and cross sections for a number of elements. Neutrons in the energy range 3-5 MeV were produced by the $D(d,n)He^3$ reaction using a 3.2 MeV Van de Graaff accelerator. Their work showed that if the incident energy is close to threshold (< 200 keV above it) and if only one or a few levels are excited, then the modified Hauser Feshbach theory must be used.

In 1962, Donahue[35] used reactor produced neutrons to study the neutron inelastic scattering reaction on a number of natural targets. His work was done using an external beam of neutrons and a NaI detection system. Only the first few excited states were observed in each case. Donahue proposed that for neutron energies greater than the threshold energy, the cross section as a function of energy can be written

$$\sigma(E) = \sigma_0(1 - \exp-\beta(E_n - E_{th})),$$

where σ_0 is a constant depending on spin and parity of the level and β is a universal parameter (3 ± 1 MeV^{-1}) independent of spin and parity. With a reactor source of neutrons the gamma ray yield is the product of the cross section times the flux as a function of energy. Donahue's results showed the yield corrected for flux was proportional to the square root of the $B(E_2)$ values for each level. This

contradicts the Hauser Feshbach theory which states that the cross section should be independent of the nature of the state. Donahue's results were in opposition to the results of Guernsey and Wattenburg[36] and in addition Van Patter[37] has pointed out that Donahue's results depend a great deal on two low values obtained for one element. In addition no attempt was made to explain the results using a Hauser Feshbach calculation.

In 1968, Ernst[38] did a study of the $(n,n'\gamma)$ reaction using the McMaster University Reactor. His work was done using an external beam of neutrons and a Ge(Li) detector. The neutron energy spectrum was approximated by $\phi(E) \sim \exp(-\alpha E)$, where $\alpha = 0.77$. Using Donahue's equation for the cross section and integrating over the flux to find the gamma ray yield, Ernst derived the following relation

$$\text{primary population of a level} = \sigma_{\infty} \cdot \phi_0 \cdot \frac{\text{yield observed}}{\exp(-\alpha E_{th})} \cdot \frac{\beta}{\alpha(\alpha+\beta)}.$$

Thus if one divides the observed yield by $\exp(-\alpha E_{th})$, then all levels of the same spin and parity should have the same value. In addition to this approach, Ernst did a limited Hauser Feshbach calculation assuming that branching to other levels in the depopulation of the intermediate state could be approximated by a constant. Due to the fact

that the Ge(Li) detector used was severely radiation damaged and also due to limitations of the beam port facilities used, the experimental results were inconclusive.

Similar experiments to the $(n,n'\gamma)$ studies have been performed on the $(p,p'\gamma)$ reaction using accelerators. The chief limitation of the accelerator experiments is that the protons have to overcome the Coulomb barrier thus limiting the energy and mass regions that may be studied. One advantage of the accelerator type experiment is that the particle energy is monoenergetic and can be varied, allowing one to measure the cross section as a function of energy. In contrast to this reactor produced neutrons having a distribution in energy allow one to measure the cross section of all levels of a target in one experimental run. This implies that branching must be considered in some detail. A second feature of the reactor source is that the mean reaction rate occurs at about 0.5 MeV above the threshold energy independent of level energy, which is the region most dependent on spin and parity of the level.

CHAPTER 2

EXPERIMENTAL FACILITIES

2-1 Reactor Facility

The McMaster University Reactor is a light-water, enriched fuel, 2 MW swimming pool reactor designed and built by AMF. It has six radial horizontal beam ports and one vertical beam tube. It is also provided with a thermal column vault. Figure 2-1 indicates the layout of the reactor and the irradiation facility built for this work. In order to have sufficient sensitivity for studying the $(n,n'\gamma)$ reaction, an internal target, tangential irradiation facility was developed. Radial beam ports are unsuitable for this type of facility since the detector would accept gamma and neutron radiation directly from the core. The vertical beam tube can be set up in the internal target arrangement; but it is limited by the fact that 32 feet of water is required for shielding above the reactor core. In addition there is a limited working area available around the upper end of the beam tube due to reactor control equipment and the upper end is located in an area where the background radiation is relatively high. Since the thermal column area was not in use, it was decided to design a facility using this area.

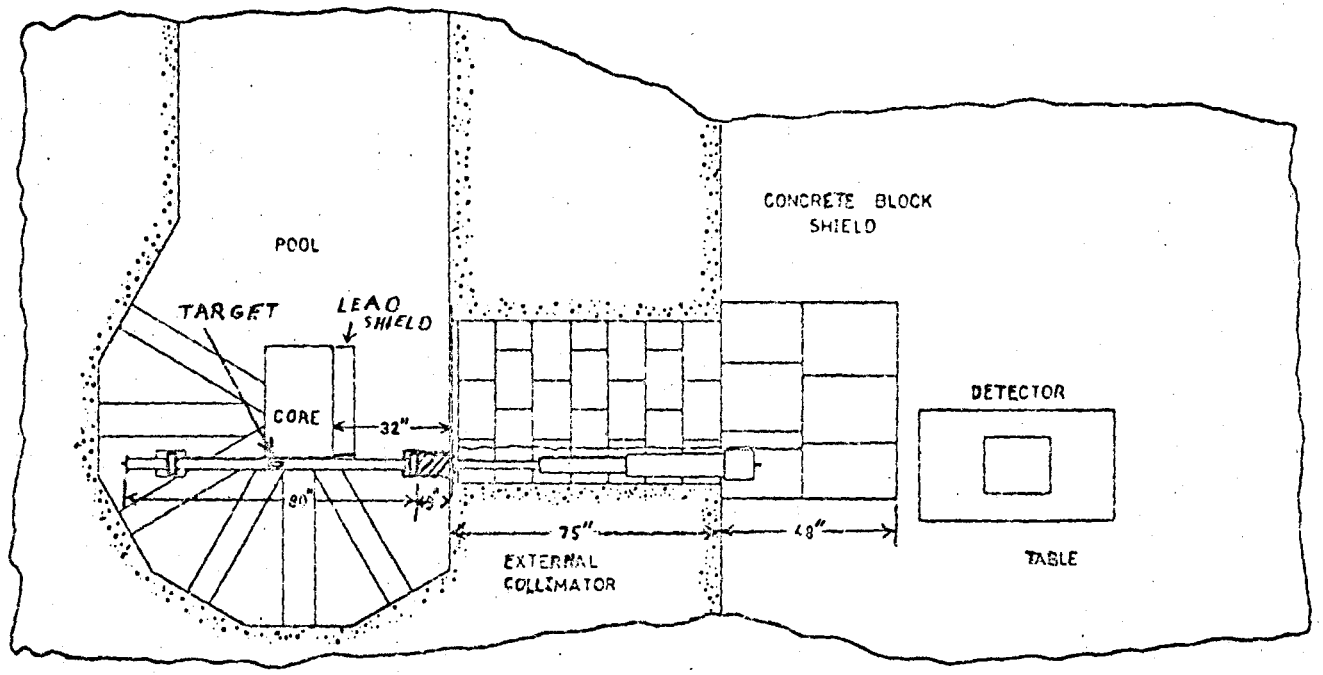

Fig. 2-1 The physical arrangement of the through tube facility. The sample chamber is 12 cm above the centre of the core and rests upon a pair of stands.

The neutron energy spectrum in the reactor core area may be divided into three categories: fast, resonance, and thermal. The fast neutrons extending from 1 to about 16 MeV are produced by the fission reaction. The resonance neutron region extends from keV up to 1 MeV giving a characteristic 1/E spectrum. These neutrons occur as a result of fast neutrons being moderated by the light water in the pool. The thermal neutrons have a Maxwellian distribution of velocities and occur as a result of neutrons coming into equilibrium with their surroundings. The emission rate of fast neutrons depends on the thermal neutron flux and hence inside the reactor core the two distributions are similar. Outside the core there is no production of fast neutrons and the relative amounts of each component of the neutron flux depends on the moderation and absorption properties of the medium. In studying the $(n,n'\gamma)$ reaction it is desirable to filter out the thermal and resonance components of the reactor neutron flux since both of these can produce the (n,γ) reaction which forms an unwanted background. Figure 2-2 indicates the neutron flux distribution for the three categories of neutrons. The relative amount of each component depends on the location around the core where the measurement is made. Section 2-4 of this work gives an experimental measurement of the thermal versus the resonance and fast neutron flux.

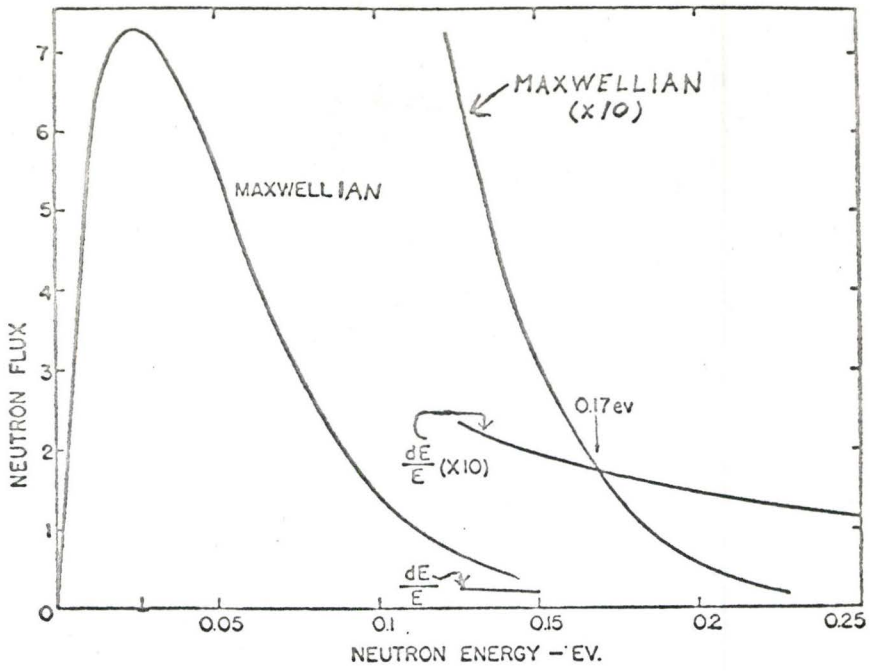

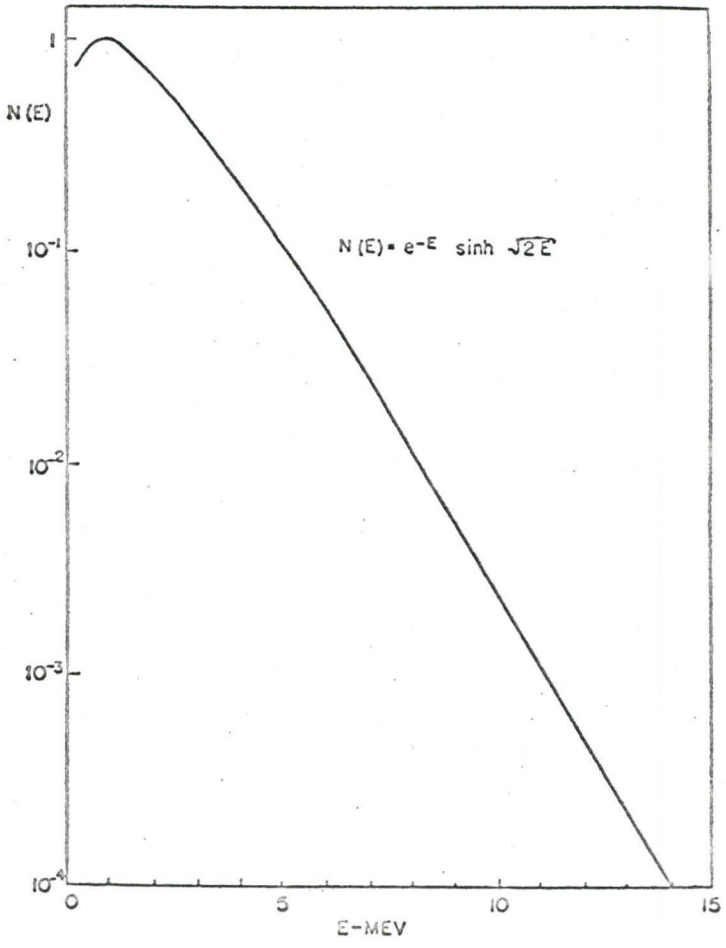

Fig. 2-2 Neutron Flux Distribution. The upper graph indicates the thermal and resonance neutron flux and the lower graph the fast neutron rate distribution.

2-2 Tangential Irradiation Facility Versus A Beam Port Facility

The study of the gamma radiation following inelastic neutron scattering may be accomplished either by use of an external neutron beam striking the sample or by placing the sample in a facility beside the reactor core and extracting the resultant gamma rays in a beam. The external neutron beam method has the advantage when it comes to handling targets, i.e. simple and fast sample changes, no danger of samples decomposing or overheating. The chief advantage of placing the target by the core in the internal position is the greater sensitivity obtained. The rate for the internal system is given by

$$k.\phi.W.\sigma.T_\gamma.\Omega_\gamma^i.\Omega_n^i.\varepsilon ,$$

where k is a constnat, ϕ is the neutron flux at the core, W is the weight of the sample, σ is the cross section for the reaction, T_γ is the probability of the gamma ray penetrating any neutron shielding required, Ω_γ^i is the solid angle for the gamma radiation detector, Ω_n^i is the solid angle for the neutrons hitting the target (approximately π), and ε is the efficiency of the detector. The rate for an external system is given by

$$k.\phi.W.\sigma.T_n.\Omega_\gamma^e.\Omega_n^e.\varepsilon ,$$

where T_n is the probability that the neutrons will penetrate any absorbers in the beam, Ω_n^e is the solid angle for the neutron beam, Ω_γ^e is the solid angle of the gamma radiation detector. The chief difference is that the external rate

depends on the product of two small solid angles and the internal rate depends on the product of one small and one large solid angle. When typical values are used in the two rates, it turns out that the internal rate is several orders of magnitude more sensitive. A second advantage of the internal case is that it is easier to predict the neutron energy spectrum since it is almost the same as a fission spectrum for energies above 100 keV. The shape of the neutron distribution for the external beam of neutrons is greatly affected by the surroundings of the beam port[39]. An additional advantage of the internal system is that the scattered neutrons are absorbed by the pool water around the reactor core, thus greatly reducing the amount of external shielding required. Finally it should be noted that the internal target arrangement leads to a well collimated gamma ray beam which is essential in using a multiple detector spectrometer system. Thus it was decided to construct an irradiation facility in which the target would be located beside the core.

2-3 Description of Tangential Irradiation Facility

Figure 2-1 gives the layout of the facility[40] used. The system consists of an evacuated aluminum target chamber, an in-pool collimator, an external collimator and a detection system. The collimation system is located in the thermal column vault which is isolated from the pool

by a 2.54 cm thick aluminum plate. In order to retain maximum flexibility for the system it was decided to thin a small region of the plate, 5 cm in diameter to 0.60 cm thickness, rather that to design a collimator built into the plate. At 500 keV the percentage of gamma rays passing through the window without interacting is 85% and at 7000 keV it is 94%. The side of the core nearest the detection system is covered by a 5 inch thick lead plate which helps to reduce unwanted gamma radiation coming directly from the core area.

The target chamber consists of 7.6 cm O.D. 65ST aluminum tubing approximately 2 m in length. The tube is located in the pool by means of removable annular lead weights clad in aluminum at each end of the chamber. The weights position the tube on "V" shaped notched supports at each end of the pool. Steel wires are attached to the weights to make handling of the tubes easy. The chamber can be operated either under vacuum or reduced pressure by means of a 30 foot long $\frac{1}{4}$ inch in diameter aluminum tube attached to the flange at the end of the target chamber and extending to the surface of the pool. For some experiments the tube can also be used to admit nitrogen gas for energy calibration purposes. Flux measurements revealed that the neutron flux at the end of the chamber nearest the detector is about 10^{-4} of the value at the core.

Since the ends of the chamber are in direct line with the collimation system, they are thinned to 1.6 mm to reduce the background radiation due to neutron capture. Several chambers were made so that after use each chamber is allowed to remain in storage for at least a week to reduce the radiation hazard before removal of the targets and reloading of the tubes.

The internal collimator consists of a 15 cm diameter, 23 cm long lead annulus with a 3.0 cm aperature. Discs of ^{6}LiF packed in aluminum containers are situated at each end of the collimator to remove thermal neutrons from the beam of gamma rays. The space between the discs was initially water filled to help remove the fast neutron component of the beam. The presence of water however, led to a large amount of Compton scattered radiation, coming from the core area, being scattered into the detector. Hence the water gap was replaced by an air filled aluminum container with thin walls to reduce the amount of material available to scatter off of.

The external collimator placed inside the thermal column vault consists of a stepped square shaped aluminum collimator 190 cm long filled with a mixture of lead and polyethylene shot with a 1 cm opening. The vault itself is filled with interlocking barytes concrete blocks. In addition to this, two layers of three foot thick barytes concrete blocks are located external to the vault to provide

additional shielding for the detection system. The fast neutron component in the gamma ray beam is removed inside this collimator by means of a 15 cm polyethylene rod. During the course of this and other work, it was discovered that the Ge(Li) detectors used suffered from neutron radiation damage and as a result the shielding was increased.

The entire collimation system was aligned with the aluminum window removed using optical methods and then checked by means of placing radioactive sources at the sample position. The size of the source chosen was typical of the samples to be used, namely 1 cm in diameter and 4 cm long. A NaI detector and a single channel analyser and scalar were placed at the end of the external collimator. Figure 2-3 shows the effect on the rate on moving the end of the collimator both vertically and horizontally. The half width of roughly 1 cm gives some idea of the degree of alignment and collimation achieved. After alignment the window was keyed to ensure realignment at a later time if required. The "V" shaped stand in the pool on the side remote from the detector was made adjustable in both height and position, from the surface of the pool, although no adjustment has been found necessary to date. The solid angle at the end of the collimator is about 10^{-6} of the unit sphere.

In order to study the $(n,n'\gamma)$ reaction, it was

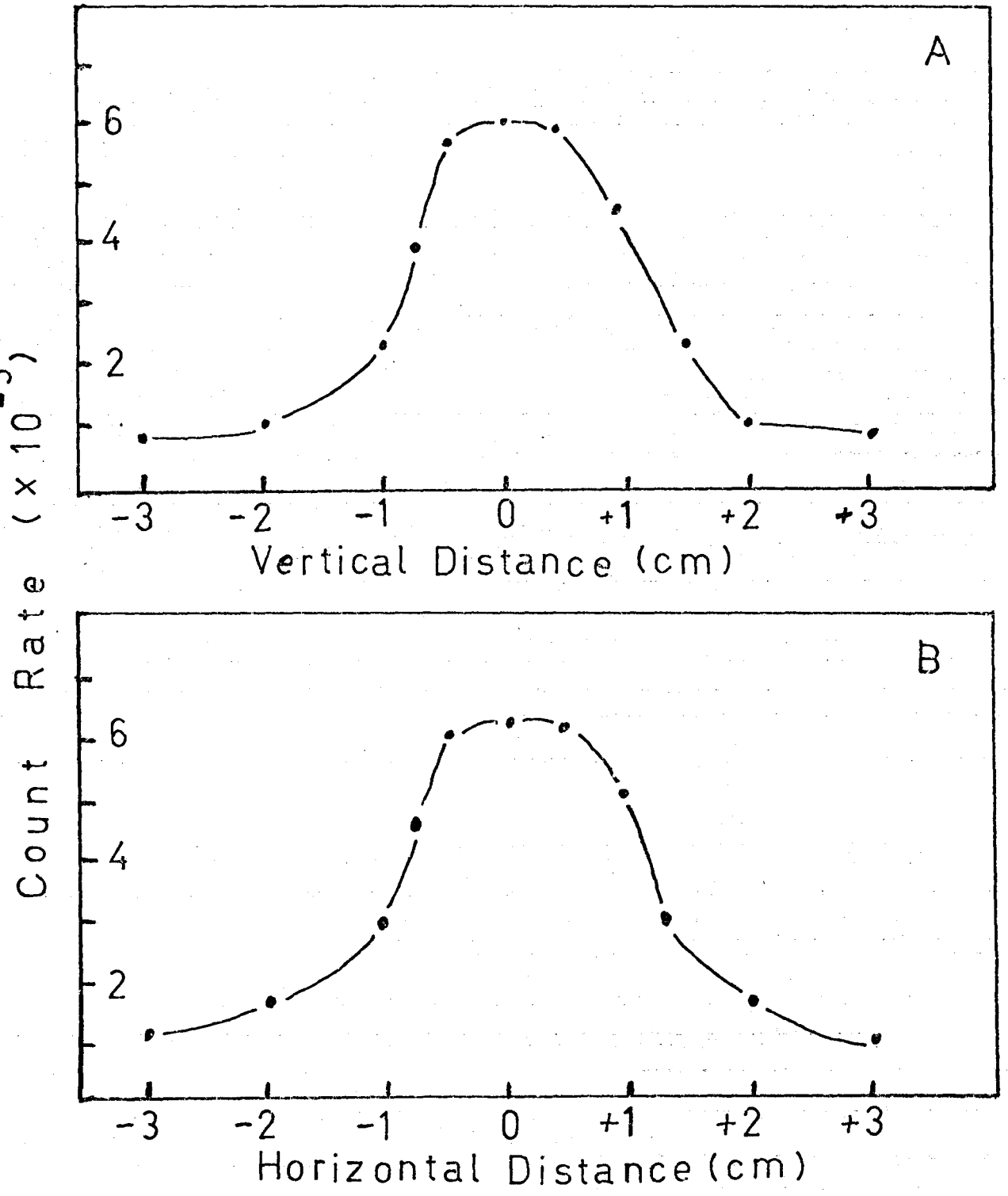

Figure 2-3 Alignment of Collimation System, (A) vertical, (B) horizontal. The two pictures show the effect on count rate in a NaI detector located at the end of the external collimator when the collimator and detector are moved horizontally and vertically.

necessary to reduce the thermal component of the reactor flux hitting the target in order to limit the (n,γ) reaction which produces unwanted background radiation. This was accomplished by means of a cadmium filter 0.048 inches thick. The filter was mounted on a 3 inch I.D. aluminum tube 20 inches in length which slides on the outside of the chamber. The slider was normally positioned to shield the sample from the core and was locked in position by means of a large stainless steel set screw. The thermal neutron flux was reduced by a factor of 10^{-6} using the cadmium filter. In order to further reduce the thermal flux and also to cut down the resonance capture reaction, a boron filter was used as well. The boron filter consisted of B_4C powder sealed inside an aluminum annulus with welded joints. The container was 18 cm long with a 4.3 cm aperture and had a natural boron carbide thickness of 1.1 cm. The container fitted inside the target chamber and was located by means of aluminum straps which formed a framework between the end caps of the chamber. The targets themselves were either solid metals or were powders encapsulated in extremely thin walled aluminum tubes and were mounted inside this filter container. The straps on the filter in addition to locating the filter and target also allowed one to handle the sources from a short distance if they were radioactive. Cooling was

not a problem, since the target chamber and the cadmium filter were in direct contact with the pool water, and the boron filter had reasonable good thermal contact with the target chamber.

The reduction in neutron capture due to resonance neutrons can be calculated if one assumes a 1/v cross section for both boron and the target material. The boron cross section can be written

$$\sigma_\beta(E) = \sigma_\beta \cdot v_T/v \ ,$$

where σ_β is the thermal cross section for boron, $v_T = 2200$ m/sec and v is the incident neutron velocity. The rate of resonance capture obtained with just a cadmium filter is given by

$$R \propto \int_{0.6}^{\infty} \sigma_o \cdot \frac{v}{v} \cdot \frac{dE}{E} = \int_{v_c}^{\infty} \sigma_o \cdot \frac{v_T}{v} \cdot \frac{dv}{v} = \sigma_o \cdot \frac{v_T}{v_c} \ ,$$

where v_c is the velocity of a neutron at 0.6 ev and σ_o is the thermal cross section of the target. The cadmium cutoff has been taken as 0.6 ev. If the boron filter is used in addition, the rate becomes

$$R_F \propto \int_{0.6}^{\infty} \exp-(\sigma_\beta \cdot \frac{v_T}{v} \cdot t) \cdot \sigma_o \cdot \frac{v_T}{v} \cdot \frac{dE}{E}$$

$$= \frac{\sigma_o}{\sigma_\beta \cdot t} \cdot (1 - \exp-(\sigma_\beta \cdot t \cdot \frac{v_T}{v_c})),$$

where t is the thickness of the boron absorber. The ratio of the two cases gives the fractional reduction in the rate

$$\text{Ratio} = \frac{1}{\sigma_\beta \cdot t \cdot \frac{v_T}{v_c}} \cdot (1 - \exp-(\sigma_\beta \cdot t \cdot \frac{v_T}{v_c})).$$

Figure 2-4 is a graphical representation of this ratio. Thus if the cross section for both the thermal capture reaction and the fast neutron inelastic scattering reaction are known, one can calculate the amount of boron required. In order to reduce the cost of the filter it was decided to use natural boron in the form of B_4C powder in a long annulus. The thickness used was equivalent to 440 mg/cm^2 of ^{10}B and gives a reduction of 0.05 times for resonance capture. The effect of the cadmium filter on the thermal neutron spectrum is shown in figure 2-5A for several thicknesses of cadmium. The lowest curve corresponds to the thickness actually used. The effect of the boron filter in addition to the cadmium filter is shown in figure 2-5B. Again the lowest curve is the value used. Above 500 keV, the two filters have little effect on the neutron flux distribution.

2-4 Neutron Flux Measurements and System Sensitivity

In order to determine the optimum location of the target chamber and its size, several horizontal and vertical neutron flux measurements were taken. Bare and cadmium covered Fe-Mn wires (85% Fe, 13% Mn, 2% Mo), were cut into one inch sections and were located at intervols inside a welded aluminum tube. The tube was then placed vertically beside the core and irradiated for a few minutes and then taken apart and the activity on the wires measured.

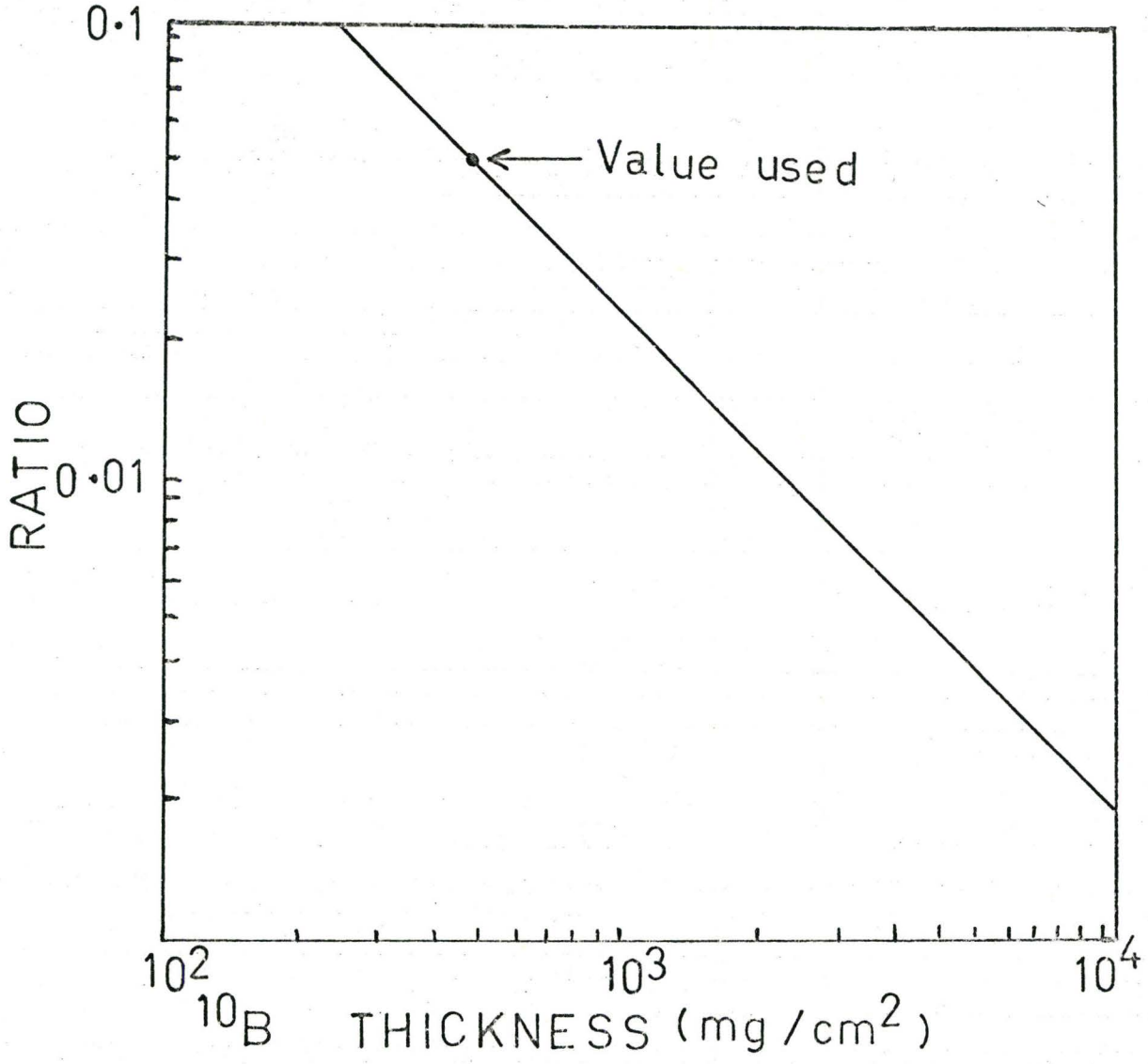

Figure 2-4 Capture Rate Reduction Using Boron Filter.

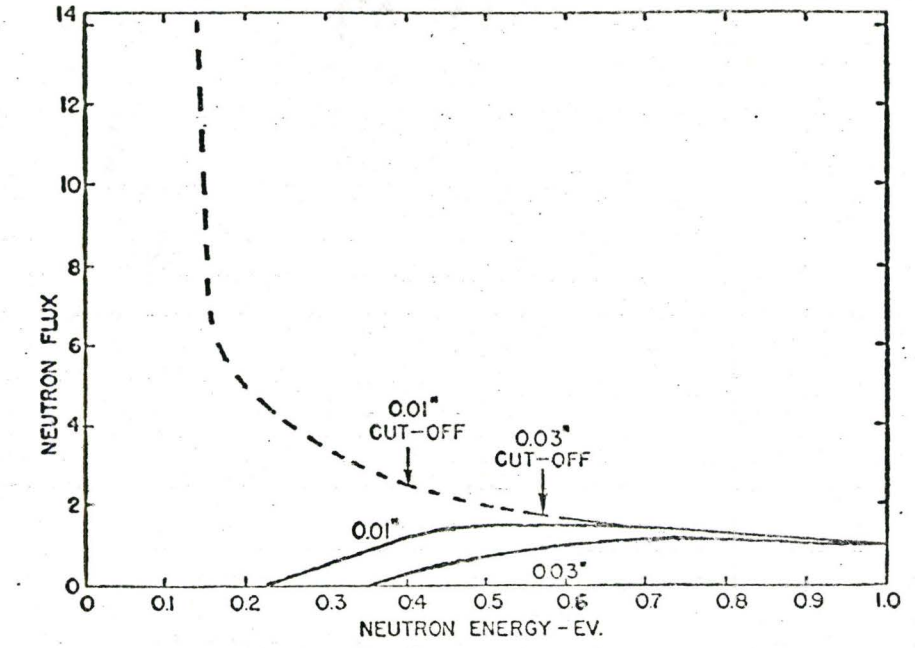

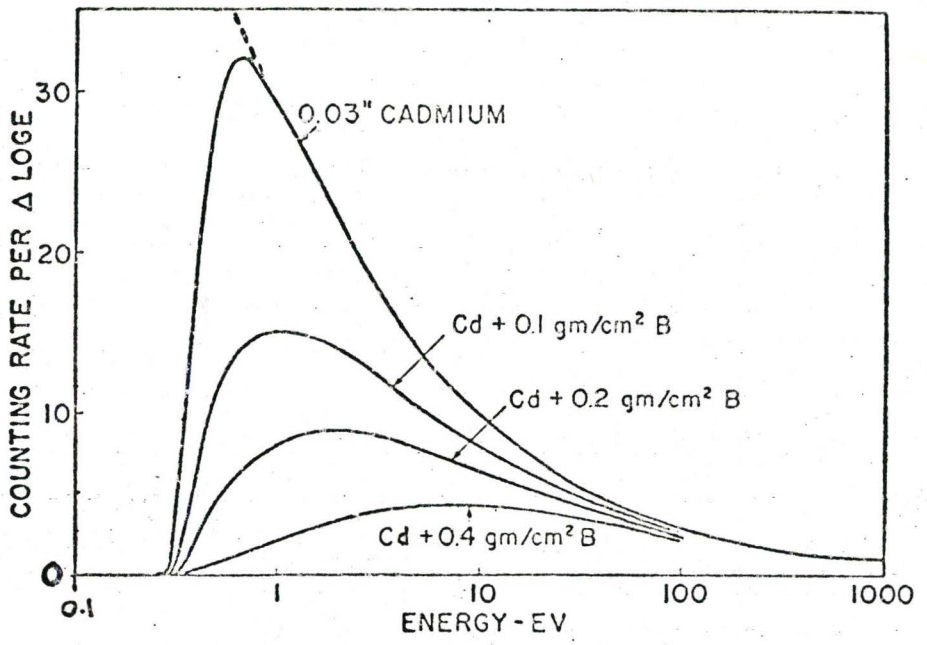

Fig. 2-5 Effect of filters on neutron flux. The upper graph gives the effect of a cadmium filter by itself and the lower graph indicates the effect of a cadmium plus a boron filter.

A similar experiment was performed with the tube in the horizontal plane out from the core. Figure 2-6 shows the results of the measurements. The vertical distribution of the resonance neutron flux had the identical shape as the total neutron flux case. The results indicated that both the thermal and resonance neutron fluxes decrease monotonically out from the edge of the core. Since no maxima were observed in the ratio of the two fluxes it was decided to locate the tube as close to the core as possible. The cross-hatched region on the vertical distribution shows the location of permanent beam ports. It was decided to place the chamber above the main beam ports in order to get a reasonable flux and at the same time to make handling of the target chambers easy. A 3 inch diameter size was chosen for the chamber to ensure a minimum of background coming from the walls of the chamber and entering the collimating system even though this meant that the targets would be back from the core. Since the tubes were operated under vacuum, it was felt that the flux distribution would be reasonably close to the value obtained at the edge of the core. The cadmium ratio was approximately constant from the edge of the core to 20 inches out from the core and equal to 50. To some extent the flux pattern depends on the conditions of the fuel rods and the location of the reactor control rods at any given time.

After the tangential irradiation facility was

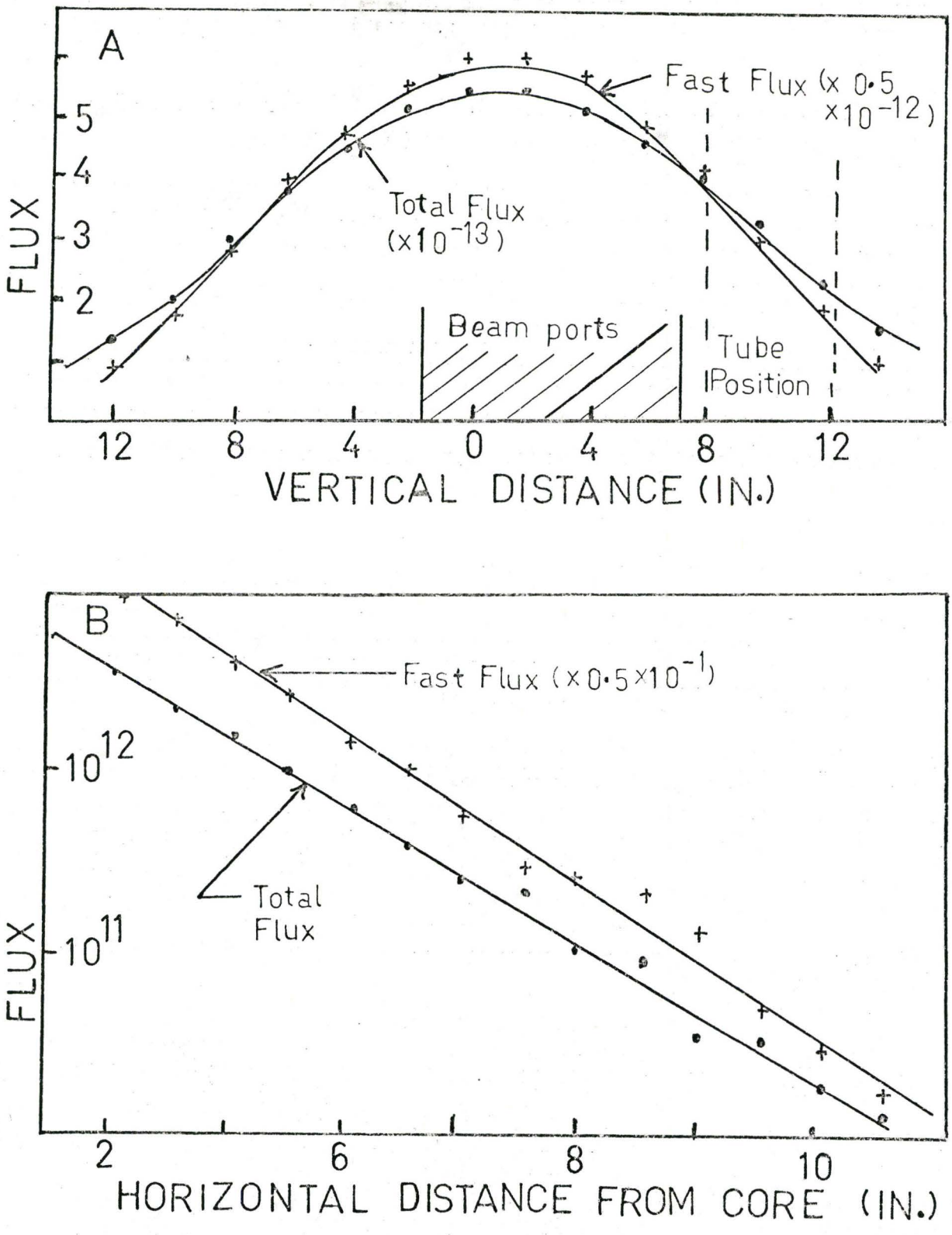

Figure 2-6 Neutron Flux Distribution. A gives the vertical distribution beside the center of the core and B gives the horizontal distribution out from the core.

constructed, experiments were undertaken to measure the absolute thermal and resonance neutron flux inside the target chamber. This was done by irradiating aluminum wires containing 0.1% cobalt for one week periods with the cadmium filter off to one side of the core and with the slider in position. The boron filter was not used in these measurements. After a three week cooling period the wires were counted in a well type ionization chamber and compared to calibrated cobalt sources. The cross section for cobalt was taken as 37 barns for both cases. This led to a total flux at the target position of 7.0×10^{12} neutrons/cm^2/sec and a resonance flux of 3.0×10^{11} neutrons/cm^2/sec, and hence, a cadmium ratio of 24. The values were obtained with the reactor operating at 2 MW. The reason that this value for the cadmium ratio is lower than the earlier one measured may be due to the fact that the cadmium filter does not completely enclose the target and as a result some neutrons may be scattered into the target area without passing through the filter.

In addition to the flux wire studies a carbon sample was studied with and without the cadmium filter. The (n,γ) reaction on carbon produces a simple spectrum containing only three gamma rays. The most prominent member is the 4943 keV ground-state transition which has an intensity of 66 events per 100 capture events[41]. The $(n,n'\gamma)$ reaction

leads to a gamma ray at 4439 keV. The cross section for this reaction has been measured as 0.23 barns[42]. The ratio for the inelastic peak area to the 4943 keV thermal peak area was found to be 0.62. If an exponential fission spectrum for the fast neutrons and Donahue's formula for the cross section are assumed, then only 2.5% of the fast flux can contribute to the inelastic reaction. If 3.5 mb is used for the thermal neutron capture cross section, then the ratio of fast flux to thermal is 0.38. Since the thermal flux was 7.0×10^{12}, then the fast flux was 3.0×10^{12} neutrons/cm^2/sec.

In order to estimate the sensitivity of the system, a 30 mg sample of vanadium wire was placed in the center of the target chamber with no neutron filters in place. The intensity of the 6874 keV transition[43] was used to obtain a pair peak rate for a 100% transition of 280 counts/sec/mole/barn. The resolution of the detector used was 10 keV and the background rate at this energy was 0.004 counts/sec. If the limit of sensitivity is defined as being the case where the peak rate equals the background rate, then

$$(\%\ \text{intensity of transition}) \times \left(\text{number of mole-barns}\right) \geq 0.0016.$$

This figure serves as a rough guide of the thermal sensitivity since it depends greatly on the shape of the background radiation. In the case of the inelastic reaction it also depends greatly on the amount of interference from gamma

rays originating in the target from the (n,γ) reaction.

2-5 The Ge(Li) Detector

The energy measurement of a gamma ray may be achieved by taking advantage of the ionization produced in a gas or solid by the gamma ray, or by making use of scintillation which occurs when a gamma ray strikes an organic or inorganic crystal. The scintillation method (NaI detector) gives less energy resolution but a greater detection efficiency. In a semiconductor diode (Ge(Li) detector), the gamma ray transfers its energy to a charge carrier by means of the photoelectric, Compton or pair interactions. The charge carrier then loses its kinetic energy by colliding with other charge carriers which it liberates. The resultant charge surge which is collected by the electric field across the diode is proportional to the energy deposited in the detector.

The detectors used in this work were fabricated using techniques described by Fiedler et al[44] and Wall[45]. The detectors were made from horizontal, float-zoned, gallium doped germanium* grown in the <111> direction. The germanium ingots were alloyed with lithium as five sided coaxial detectors using an electroplating bath[44]. After the drifting procedures and clean-up drift, the detectors were mounted in cryostats and cooled to liquid nitrogen temperature.

*The germanium was obtained from Hoboken in Belgium through NPC Electronics Co. located in Los Angeles, California, USA.

Typical detectors used were 15-20 cc in active volume with a cross sectional area of 12 sq cm and a height of 1.4 to 2.0 cm. This size of detector was chosen because it was relatively easy to make and by collimating the beam down the long axis of the counter, a reasonable percentage of the gamma rays interacted in the detector. The fraction of the gamma rays at 7000 keV which interact in the detector is of the order of 50%. In addition there was a reasonable probability of the annihilation gamma rays escaping from the detector to be captured in the NaI annulus, thereby enhancing the pair mode of operation. The collimating system was chosen so as to provide a beam of gamma rays approximately 1.5 cm in diameter at the detector. Leakage currents of 1 nanoampere at 1500 volts bias were obtained for the detectors with a resolution initially of about 3 keV full width at half maximum at 1 MeV and about 7 keV at 7 MeV. The resolution of the detectors varied somewhat due to rate effects and greatly deteriorated during usage due to the scattered fast neutron component of the gamma ray beam which produced radiation damage in the detectors.

Figure 2-7 is a block diagram of the electronics system used. Signals from the Ge(Li) detector were amplified by a Tennelec TC 135 charge sensitive preamplifier. The signal was then filtered and amplified by a Tennelec TC 200 main amplifier. Since high rates were used, the signal

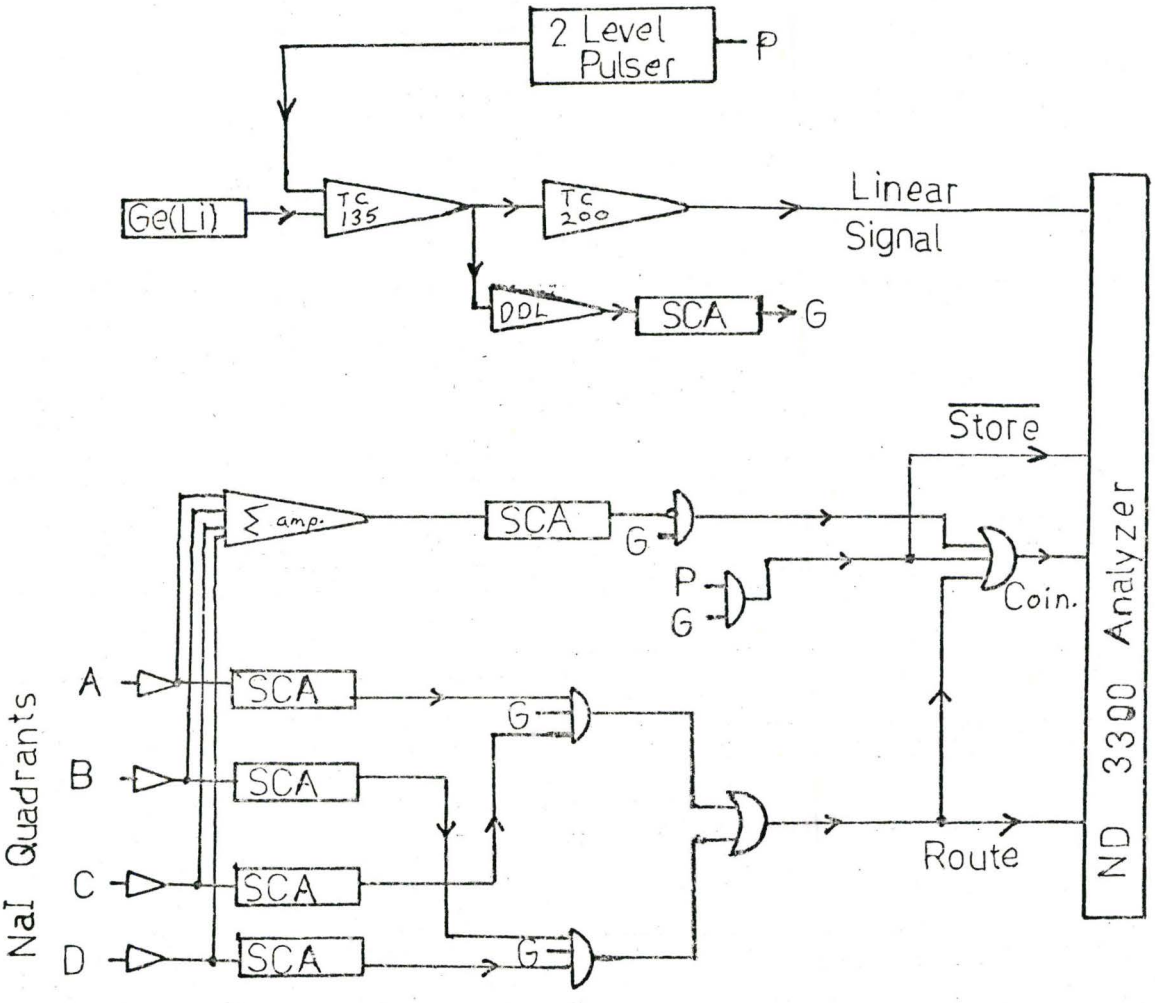

Figure 2-7 A schematic representation of the electronic logic and linear circuits used for the detection system. Provision is made to concurrently record pair and photo-electric events occurring in the Ge(Li) detector. A dual level pulser is used to stabilize both the zero and gain of the system.

was passed through a Tennelec TC 610 baseline restorer. The signal was delayed using an Ortec Model 427 delay amplifier in order to allow time for signals coming from the NaI annulus to be electronically processed. Next, the signal was presented to a 4K ramp ADC of a Nuclear Data 3300 analyzer having 16K of memory. Gain and zero shifts were handled in two ways. One method was to use a Nuclear Data Series 3300 Digital Spectrum Stabilizer unit. Since this method requires strong peaks at the low and high energy ends of the spectrum, which were not always available, a precision pulser[46] was built to provide them. It was found that the pulser was stable over a period of several weeks compared to thermal neutron capture gamma rays. A second method of stabilization was achieved by recording the accumulated spectrum every few hours on magnetic tape and then using a computer program which lines up a high and a low energy peak in each spectrum recorded and then sums the spectra up. The computer shifting method was developed because the electronic stabilizing unit was not available initially. Both methods were found to be satisfactory. The computer shift method did however tie up the tape deck facilities and as a result the stabilizer was used for most of the experiments. One advantage of the computer method was that if the reactor was shut down for a period of several days in the middle of the experiment, the stabilizer sometimes needed to be

adjusted to regain control of the experiment, whereas the computer approach made it easy to deal with this problem.

Figure 2-8C shows a typical detector response for a 3 MeV gamma ray. Figure 2-8A shows the response for photoelectric and Compton events. The full energy peak consists of photoelectric events and also multiple events. For example, if a Compton scattered photon undergoes a photoelectric interaction in the detector, the result is a full energy event. The peak at $mc^2/2$ occurs as a result of back-scattered radiation. Figure 2-8B indicates the response for pair events. The first and second escape peaks occur when one or two annihilation quanta escape completely from the detector. The continuum of events corresponds to events in which the quanta interact and only partially escape. The 511 keV peak and its associated Compton continuum arises when pair production occurs in the source or surroundings and an annihilation quantum proceeds into the detector. Counts just below the full energy peak can occur either as a result of incomplete charge collection of a full energy event or as the result of multiple events, adding together in the detector. For the detectors used the full energy peak height was equal in height to the second escape peak height when the gamma ray energy was about 3000 to 3500 keV.

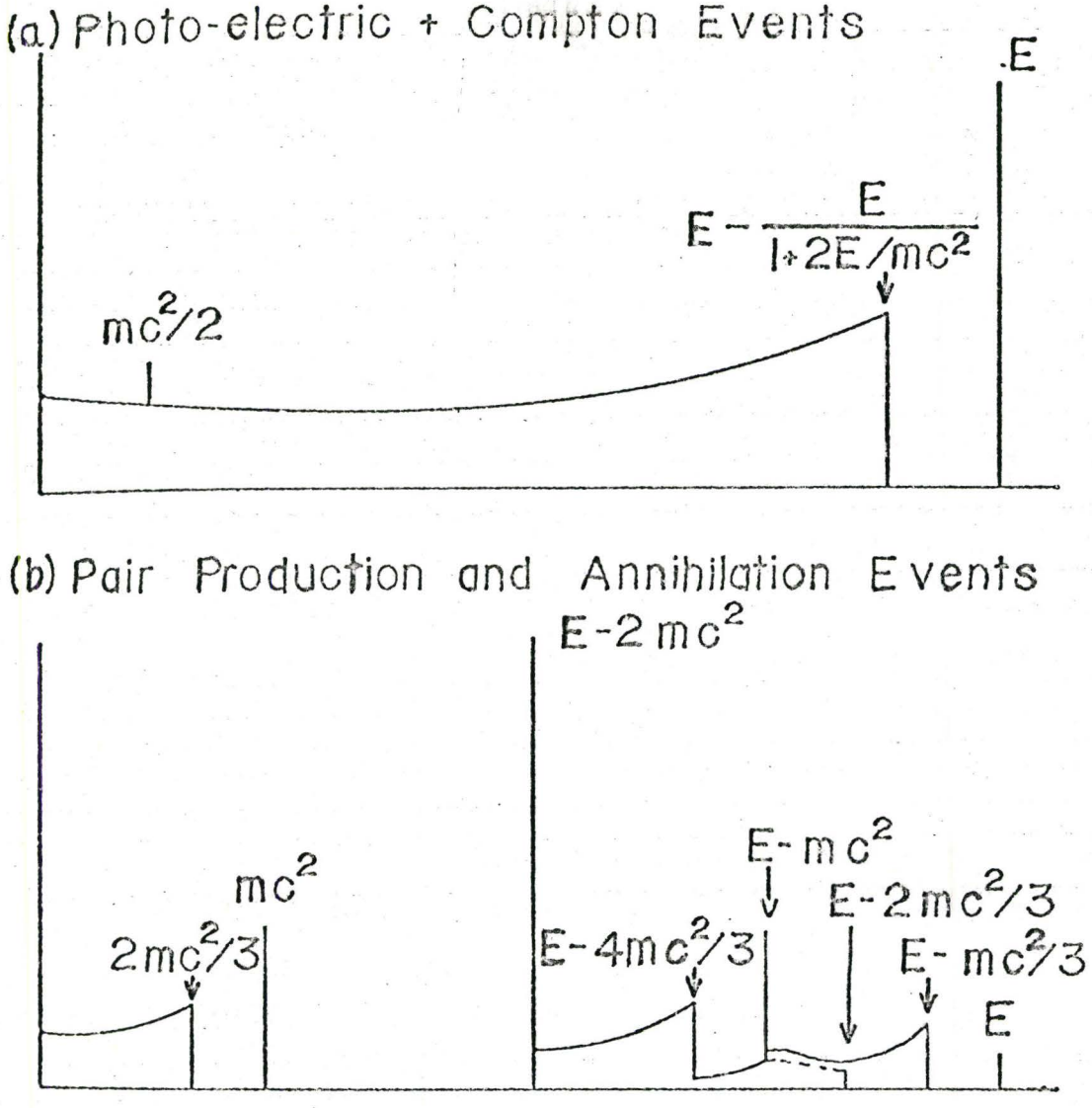

Fig. 2-8 A typical Ge(Li) detector response to a 3 MeV gamma ray.

2-6 NaI Split Annulus Detection System

The chief disadvantage of the Ge(Li) spectrometer is its complicated response function. At energies above 1022 keV the response includes a full energy peak, first and second escape peaks and a Compton continuum. Thus the response function is redundant and also includes a significant Compton background which simply lowers the signal to noise ratio. This means that weak photo-peaks can be easily masked by the Compton continuum of strong higher energy gamma rays. In addition if the spectrum is complex, escape peaks and photo-peaks of different gamma rays may interfere with each other. Increasing the size of the Ge(Li) detector improves the response by enhancing the full energy peak; but this approach is limited by present day fabrication techniques. Collimated beams also improve the response by limiting the gamma rays to the central part of the active region of the detector. However, present detectors have a peak to Compton(background) ratio of generally less than 25 to 1. The spectral complexity and the unwanted Compton background can both be reduced by operating the detector in a pair mode at high energy and in a Compton suppression mode at low energy, using a NaI split annulus system. Reduction of the Compton continuum is particularly important in dealing with gamma rays produced in fast neutron reactions, since the peaks are Doppler broadened, thereby reducing the peak height to

noise ratio.

The NaI split annulus is 15.2 cm long with an outside diameter of 23 cm. It is split into four optically isolated quadrants, each with its own photomultiplier. The central opening is 7.6 cm in diameter. The entire crystal is surrounded by Al_2O_3 reflector and is hermetically sealed in aluminum. The design of the Ge(Li) cryostat permits the detector to be located at the optimum position along the central axis of the annulus. Figure 2-9 shows a cross-sectional schematic drawing of the annulus with the Ge(Li) detector in place. The annulus is surrounded by a lead shield 4 cm thick and 30.4 cm long. The face of the annulus nearest the target is protected by a 7.6 cm thick lead shield with a 2.5 cm aperture. Since the gamma ray beam is approximately 1.5 cm in diameter at the detector, this shield provides crude collimation in addition to protecting the annulus from background radiation. The entire assembly is supported on a steel table which can be adjusted in all directions in order to align the detector system with the beam.

Signals from the four quadrants are amplified by Stirrup preamplifiers and double delay line amplifiers and are then passed through Stirrup single channel analyzers. Figure 2-7 shows the basic electronic logic used to route events in the Nuclear Data 3300 analyzer. Pair events are selected by demanding a triple time coincidence between

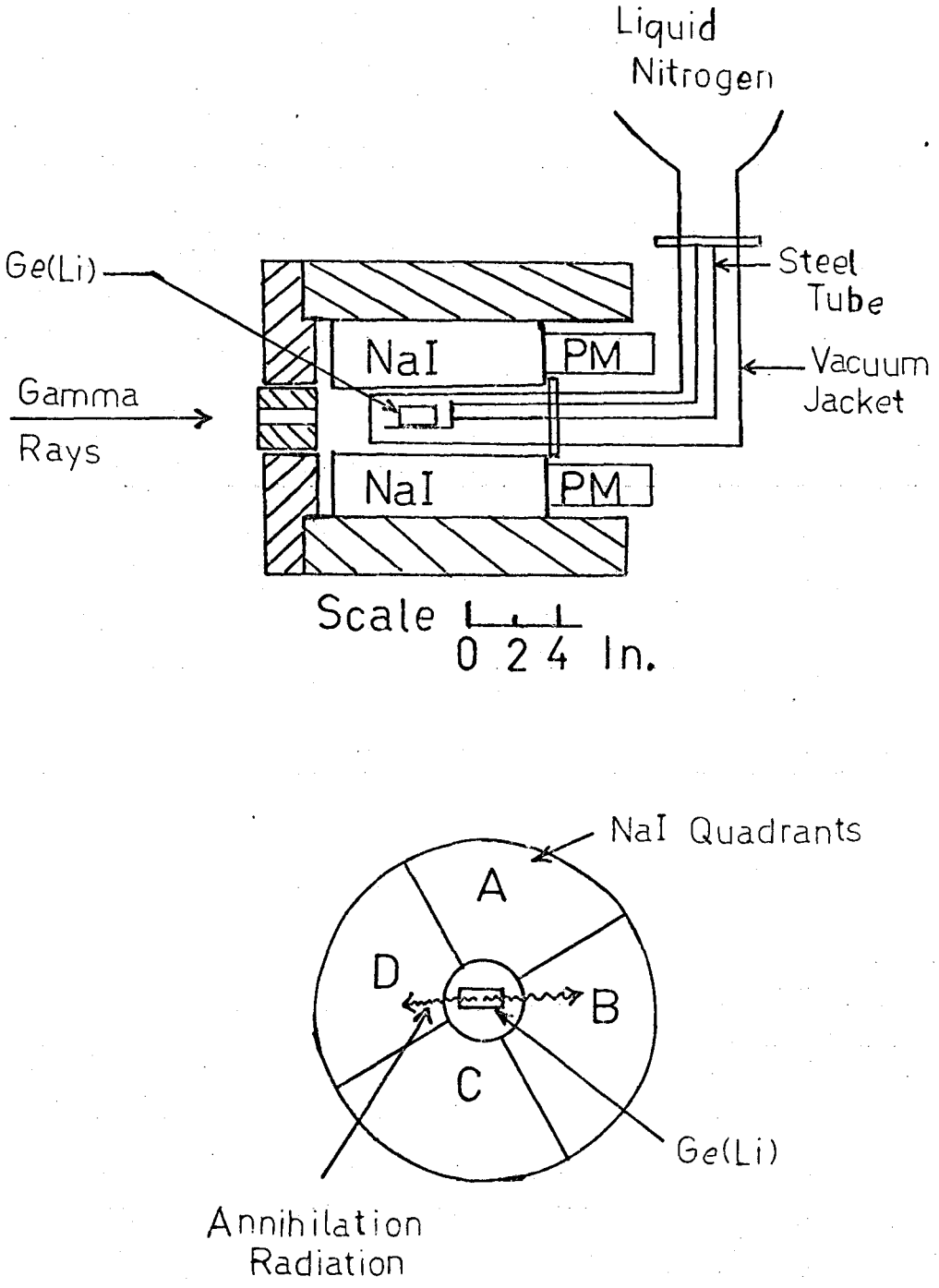

Figure 2-9 Detection System. The NaI annulus consists of four optically isolated quadrants. In the pair mode of operation the annihilation quanta are detected in oppossite quadrants since they are emitted at 180° to one another.

the Ge(Li) detector and two opposite quadrants, in addition to satisfying the 511 keV energy requirements in each quadrant. Rejection of Compton events is achieved by demanding anti-coincidence between the Ge(Li) detector and all quadrants. Compton suppression and pair modes can be operated simultaneously by means of routing the pulses in the analyzer into two different 4K memory groups. The two level pulser is used to stabilize gain and zero for the Ge(Li) detector and its pulses are not normally stored in the analyzer.

The NaI annulus spectrometer was tested using a Na^{22} source. With the gains of the four quadrants matched, resolution of 10% for the four quadrants on the 511 keV gamma ray was obtained. In addition there was no appreciable gain shift when the source was moved from one end of the annulus to the other. The Na^{22} source was mounted inside a $\frac{1}{4}$ inch diameter, thick walled aluminum tube $1\frac{1}{2}$ inches long, which is the approximate length of the Ge(Li) detectors used. The thick wall ensured that the positrons emitted by the source were annihilated to produce 511 keV gamma rays. Figure 2-10 indicates the count rate obtained as the source was moved along the central axis of the annulus. The 1275 keV gamma ray emitted by sodium is in time coincidence with the positrons; thus the time coincidence rates for the two halves of the annulus did not go to zero at the ends of the annulus.

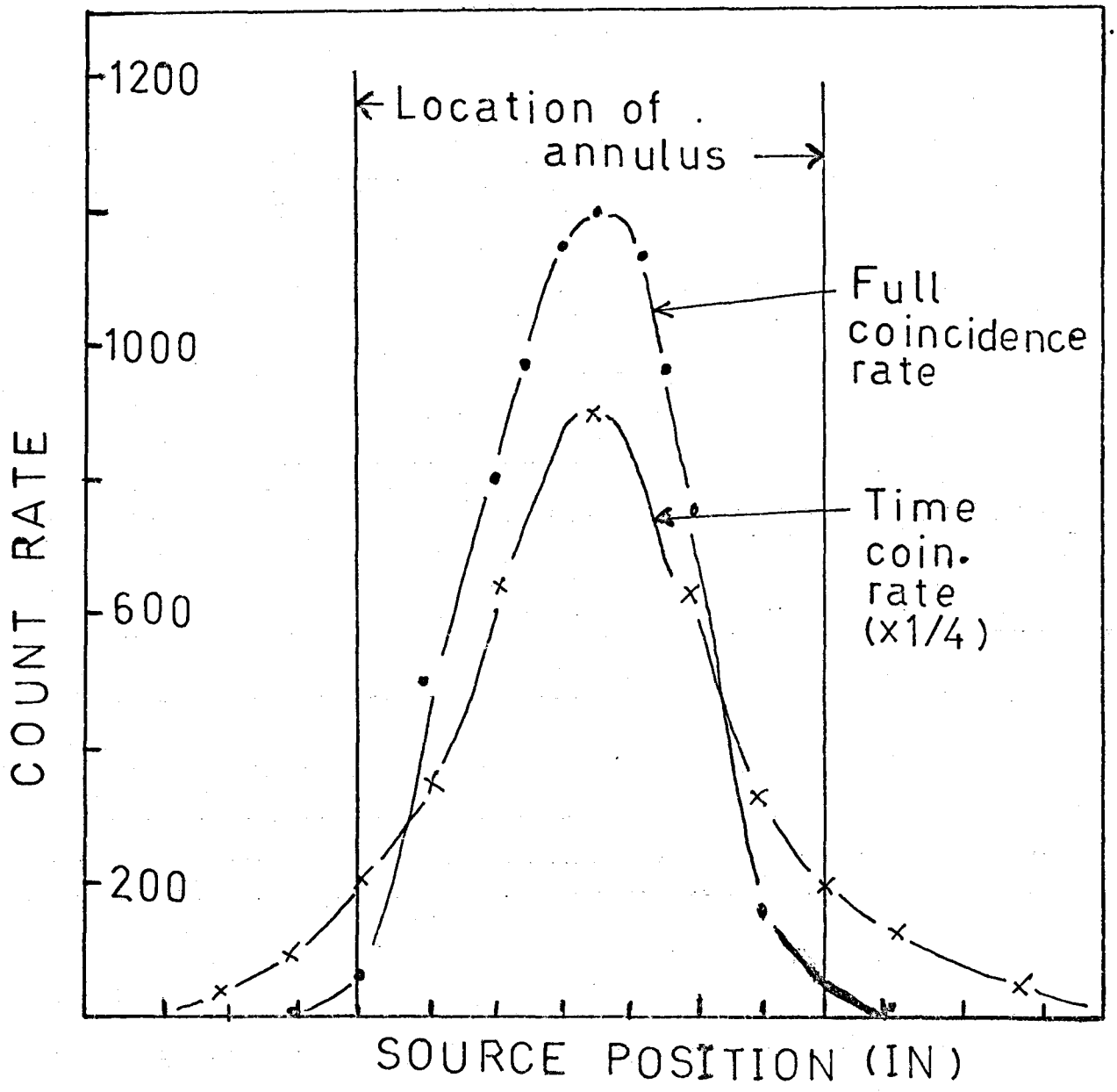

Figure 2-10 NaI annulus count rate as a function of position along the central axis of the annulus for a ^{22}Na source. Results are given for one pair of quadrants only. The coincidence rate obtained using energy requirements alone gave results similar to the full coincidence rate.

Since the 511 keV gamma rays are emitted in opposite directions, the energy coincidence rates did tend to zero at the ends of the annulus. The time coincidence rates for the two halves of the annulus and the individual singles rates for each quadrant varied because of the difficulty in setting the lower level of the discriminators exactly the same on each single channel analyzer.

Figure 2-11 shows the detector response to the Na^{22} source placed in front of the Ge(Li) detector on the central axis within the annulus. Part A is the response of one of the NaI quadrants, part B is the response of the Ge(Li) detector and part C is the response of the Ge(Li) detector operated in the pair mode. The peak at 1786 keV is due to coincidence summing of the 511 keV and 1275 keV gamma rays in the detector. The Ge(Li) detector has a peak to Compton ratio of about 10 to 1 with a resolution of about 3 keV at 1275 keV. The peak to Compton ratio is somewhat limited by the fact the annulus is present to scatter events back into the Ge(Li) detector. In part C, the 511 keV gamma rays produced by positron annihilation trigger the pair logic circuit, and the 1275 keV gamma ray and its Compton continuum, which are in time coincidence with the positron emission, are recorded. Parts B and C were recorded concurrently using the routing electronics. The fact that there is no trace of a 511 keV gamma ray in part C indicates the reliability

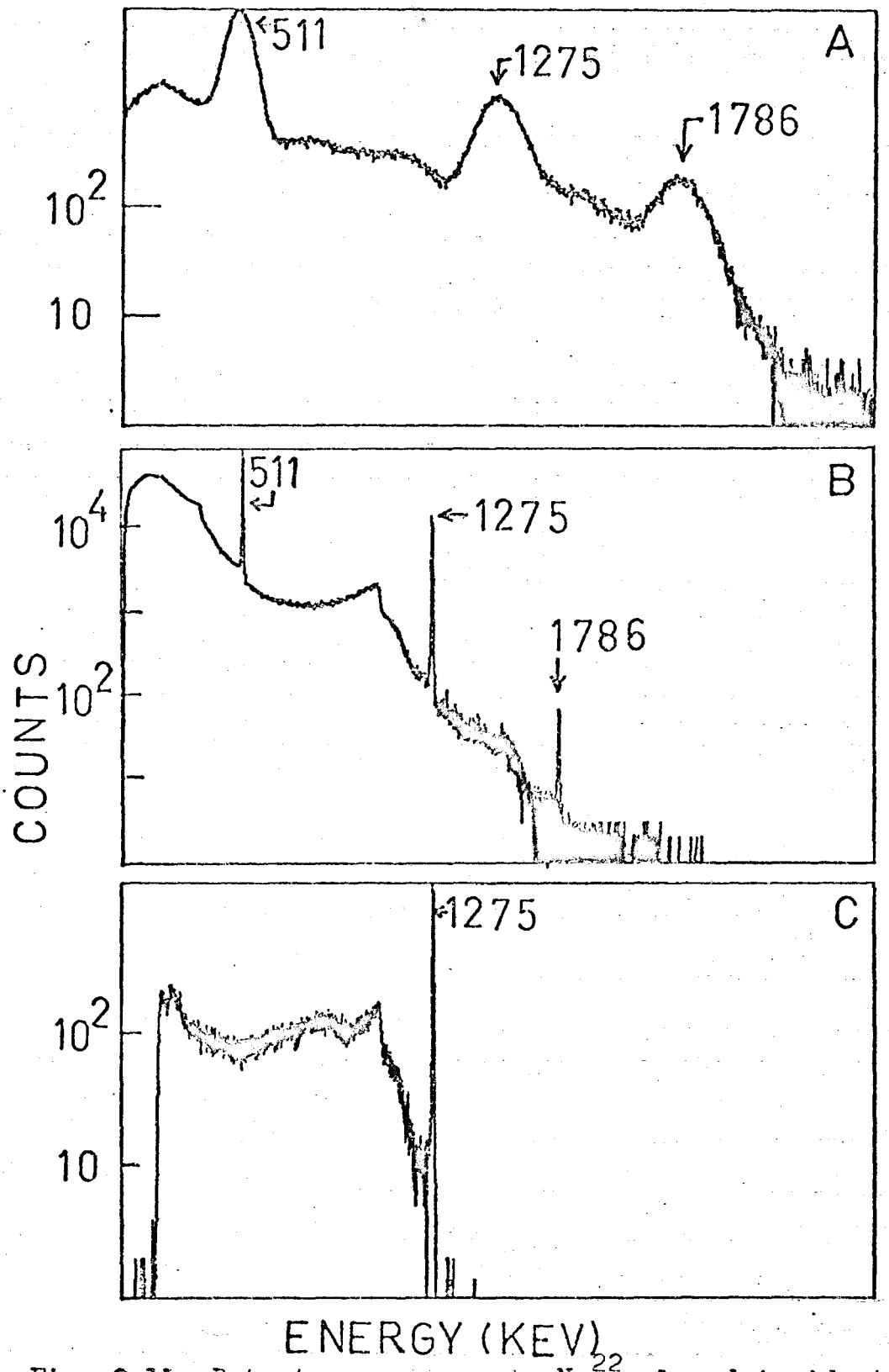

Fig. 2-11 Detector response to Na^{22} placed inside the annulus on the central axis. Part A is the response of a NaI quadrant. Part B is the response of the Ge(Li) detector and Part C is the response of the pair mode of the detection system.

of the logic and routing electronics, for the source strength used which was typical of the (n,n'γ) experiments done later. One of the reasons for this is the exclusive conditions imposed on the pair mode. In practice the logic circuitry can be operated with either the energy demands or the timing requirements alone on the pair mode. Since the second escape peak was not affected by the extra requirements, all experimental results were obtained using the full pair logic.

Figure 2-12 shows the response of the detector system using a natural thorium sample. All three spectra were obtained for the same counting time. The uppermost spectrum was a singles mode spectrum. The middle one was obtained using the Compton suppression mode and the lower spectrum was obtained using the pair mode. The picture of the pair mode response has been shifted down by a factor of 10 to facilitate the display. It is obvious that for energies above approximately 1100 keV that the pair mode greatly reduces the complexity of the response. The peak to background in this mode is approximately 600 to 1, at 2614 keV. Since the normal full energy peak height to continuum ratio is roughly 10 to 1 at this energy, the overall improvement in signal to noise ratio is about 60 times. The response in the pair mode consists of the second escape peak, a low energy tail, and a plateau extending about 30 keV up on the high energy side.

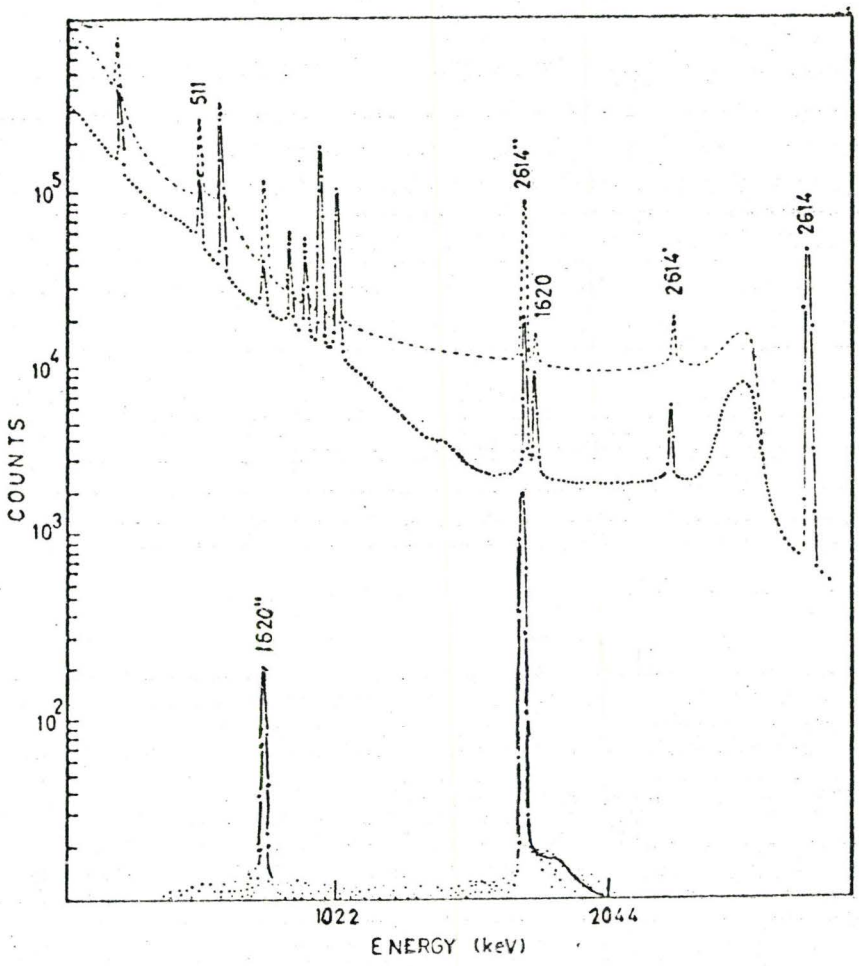

Fig. 2-12 Response of detection system to thorium using the singles, Compton suppression and pair modes of operation.

The plateau is the result of small angle scattering of the annihilation radiation in the Ge(Li) detector leaving behind extra energy which adds on to the true pair energy. The resolution of the NaI detectors (approximately 50 keV at 511 keV) still allows the partially degraded annihilation gamma rays to be accepted as true events. The tail which extends down to the threshold of the electronics is caused by electron range effects. The efficiency of the pair mode is 21% at all energies. The efficiency is limited by the acceptance angle of the annulus (roughly 80% of 4π), by absorption in chamber walls and the cryostat and by the photoefficiency of the NaI detectors(of the order of 50%).

In the Compton suppression mode the annulus is used in an anti-coincidence mode with the Ge(Li) detector. Since the dimensions of the detectors are finite and the solid angle subtended by the annulus is less then 4π, the partial energy transfer events are not completely suppressed. The Compton suppression mode is however still fairly effective giving a photopeak to background enhancement of up to 5 times. The effectiveness of the Compton suppression increases with energy since the ratio of the Compton to photoelectric cross sections increases with gamma ray energy. Compton edges are enhanced since large angle scattering (backscattered radiation) can escape through the entrance aperture of the annulus. The full

energy peaks are unaffected in the Compton suppression mode. Pair and first escape peaks are greatly reduced. The 511 keV gamma ray line consists of annihilation radiation produced by pair interactions in the source itself as well as being produced by pair events in the collimator and chamber walls.

2-7 Performance of Tangential Irradiation Facility

Figure 2-13 shows the response of the entire tangential irradiation and detector system on the pair mode using a solid melamine sample ($C_3H_6N_6$). No neutron filters were used for this experiment. Most of the peaks in the spectrum are due to nitrogen with a few carbon lines and a line at 2223 keV due to neutron capture in hydrogen. The intense ground state transition in aluminum at 7725 keV is produced by scattered neutrons being captured by the aluminum parts at the end of the target chamber and collimator assembly. The line could also be due to elastic scattering of aluminum gamma rays originating in the core area or in the target chamber walls. The iron doublet in the background occurs as a result of using a steel end cap on one end of the target chamber. These peaks were not present when an aluminum end cap was used. The resolution is 4 keV at 2200 keV and 7 keV at 7000 keV. The carbon peak at 4433 keV is Doppler broadened since it is produced by inelastic scattering of fast neutrons on ^{12}C.

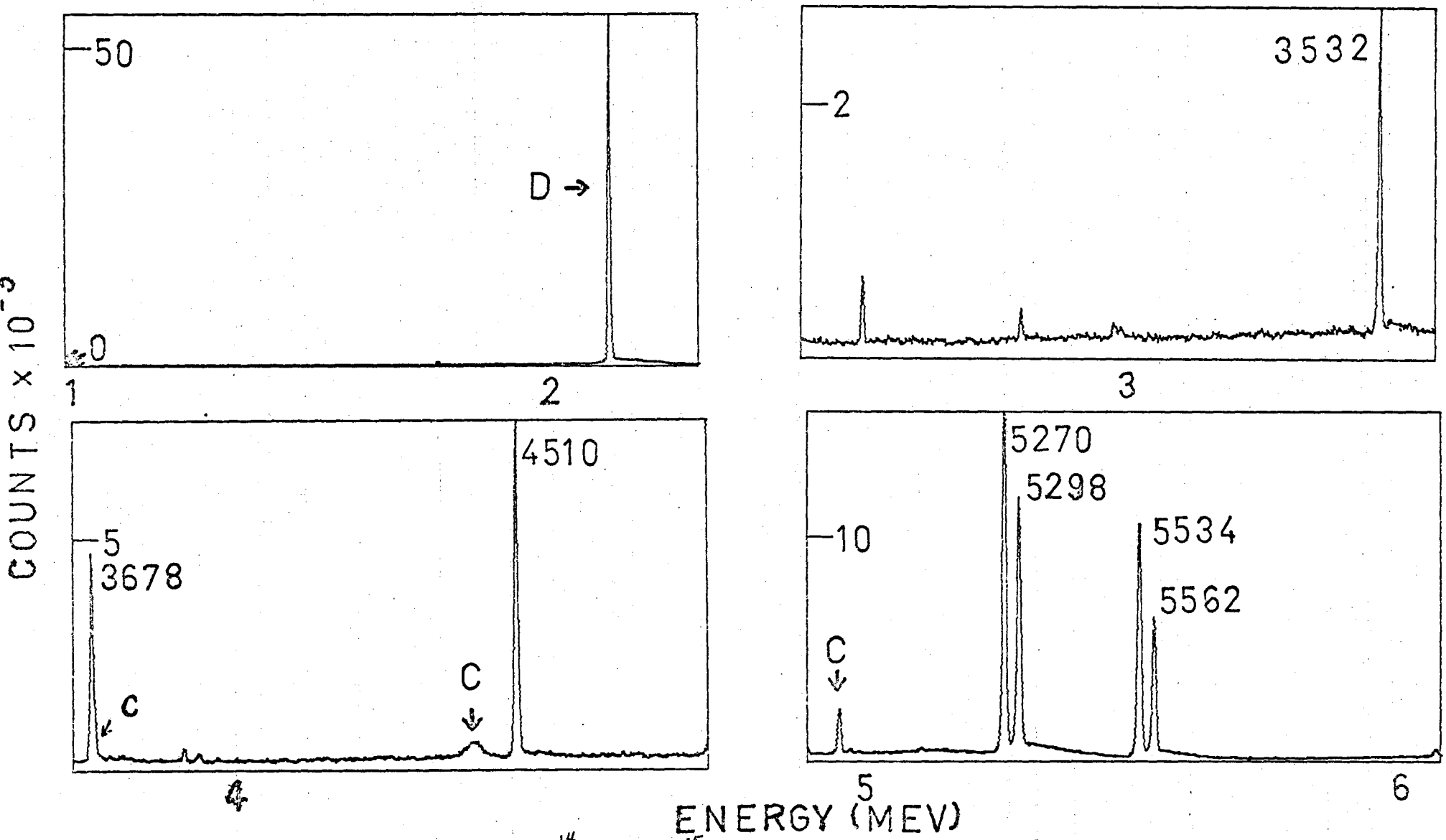

Fig. 2-13 Pair response spectrum of $^{14}N(n,\gamma)^{15}N$. The energy scale refers to the full energy of the gamma ray.

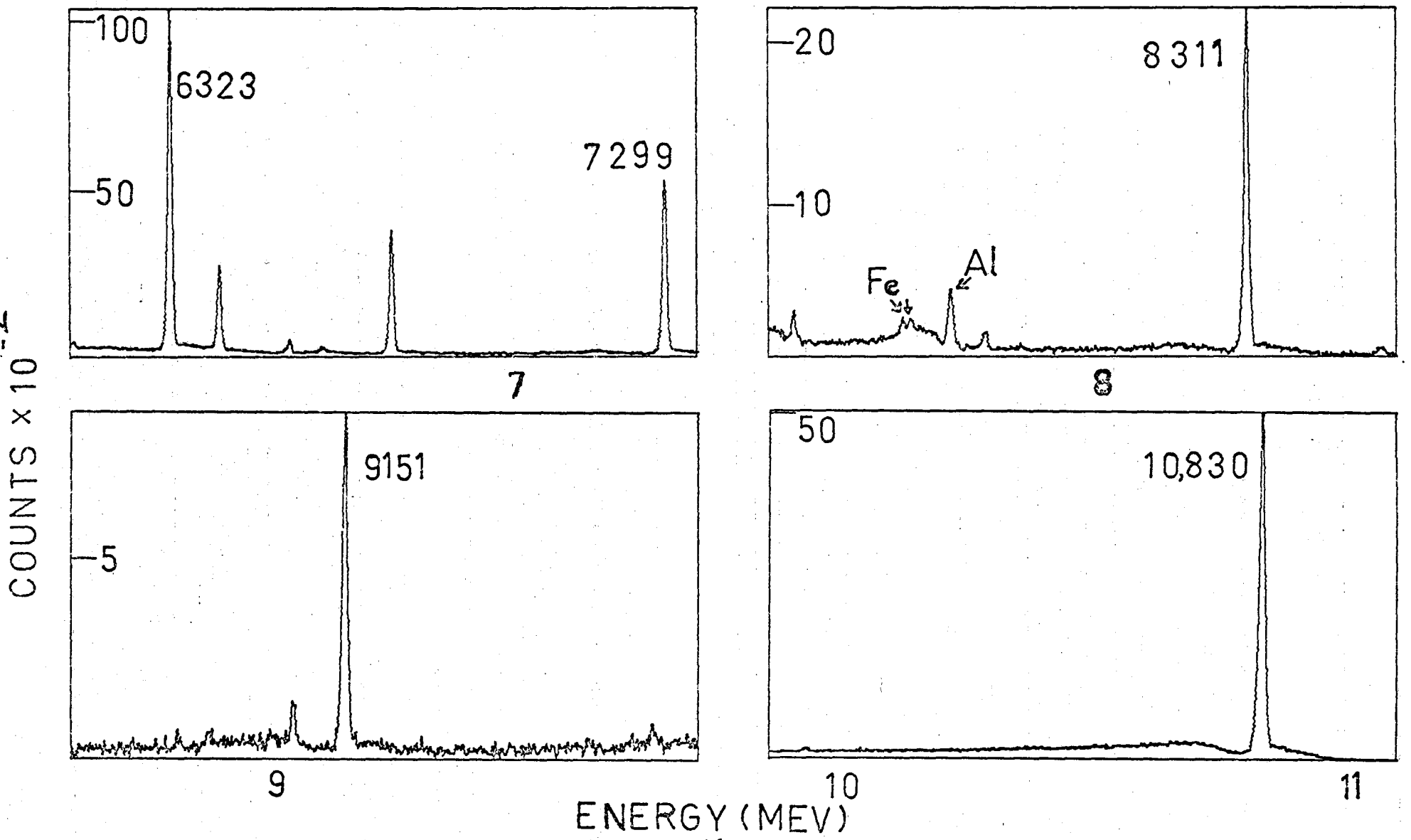

Fig.2-13 Pair response spectrum of $^{14}N(p,\gamma)^{15}O$. The energy scale refers to the full energy of the gamma ray.

The system is sensitive enough to use nitrogen gas at atmospheric pressure in the target chamber along with a target to do a mixed source energy calibration. Since the chamber is connected to the surface of the reactor pool by means of a small metal tubing, samples are run under vacuum and nitrogen gas can be admitted while the reactor is running.

Figure 2-14 indicates the pair and photoefficiency of the system. The pair efficiency curve is given for two of the detectors used. For both detectors the pair efficiency curve follows the theoretical pair cross section in germanium up to about 5 MeV. Above this energy, the curves fall off due to finite size of the detectors. The low end of the pair efficiency curves are very slightly lower than the theoretical pair cross section curve due to absorption of gamma rays by the polyethylene absorber. The fact that a collimated beam of gamma rays is used is probably why the curves follow the theoretical curve to such a high energy. The difference in the two detectors is largely due to the height of the detectors. The one in which the curve tends to level off was higher than the one which drops significantly. It may be that in the former detector the path of the direct gamma beam was below the dead "p" region of the detector; while for the latter one it was hitting this central dead region thereby reducing the efficiency of the detector at higher energy.

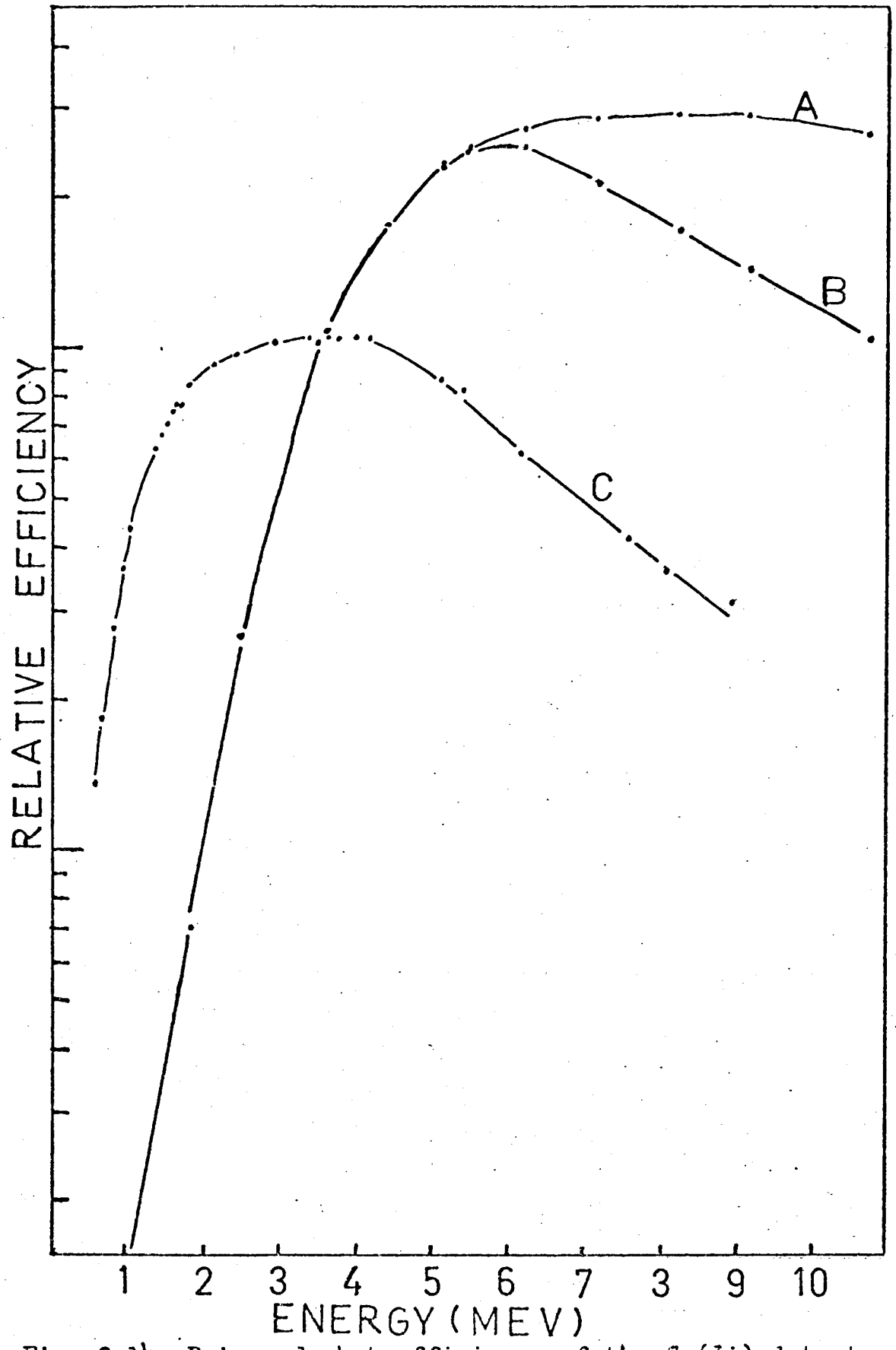

Fig. 2-14 Pair and photoefficiency of the Ge(Li) detectors. A and B give the pair efficiency for two different detectors and C gives the photoefficiency of one of them.

The photoefficiency curve is shown for one of the detectors and it forms a fairly straight line on a semilogrithmic plot except for severe drop off at low energy due to absorption by the neutron shielding. The two curves are normalized relative to each other by the fact that in a single parameter spectrum the pair peak and photopeak at 3500 keV are equal in height. The pair peak energy scale is the full energy of the gamma ray and not the energy deposited in the detector. The efficiency curves were obtained using nitrogen, gamma rays following decay of gallium, vanadium, aluminum and various other standards.

Figure 2-15 shows the background of the system. Part A was obtained using an empty target chamber over a 24 hour period of time. The prominent peaks are at 7725 keV and 1778 keV due to aluminum, and a peak at 2223 keV due to neutron capture in hydrogen. In addition to these there are numerous small peaks which are quite broad, probably due to Compton scattering. Table 2-1 lists the lines observed. Part B was obtained by using a carbon sample at the target position for a 4 hour run. The carbon spectrum consists of two (n,γ) lines at 4945 keV and 3648 keV, and a Doppler broadened line due to inelastic neutron scattering at 4433 keV. The 7725 keV line appears to be enhanced compared to the 1778 keV line suggesting the possibility of elastic scattering as one mechanism contributing to the formation of these background lines.

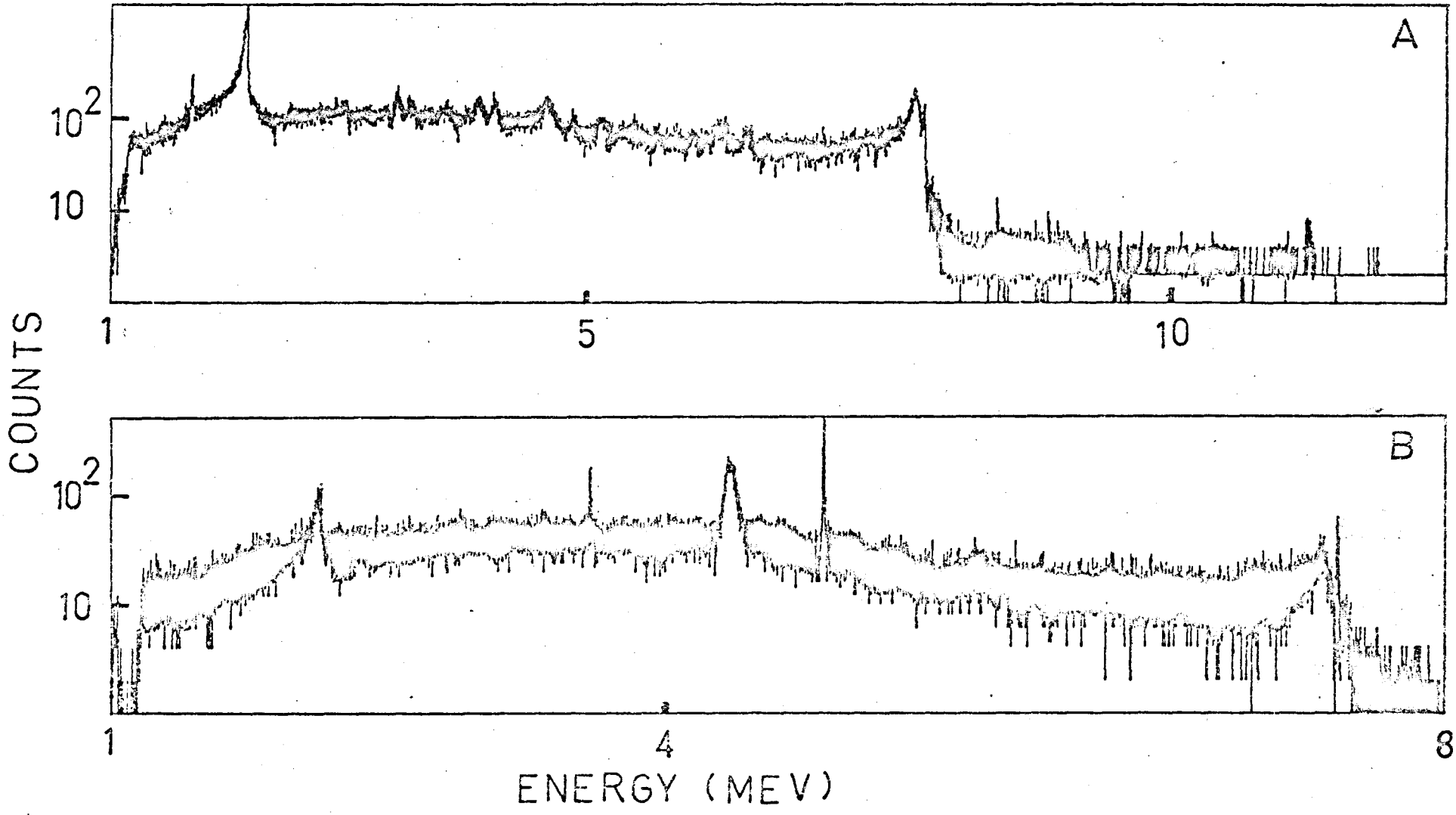

Figure 2-15 System Background. Part A was obtained using an empty target chamber over a 24 hour period of time. Part B was obtained using a carbon sample at the target position for a 4 hour run.

Both the 7725 and 2223 keV lines have a broad Compton scattered component just below these energies. The geometry of the reactor and lead plate beside the core provide an acceptance angle of 2 to 5° for gamma rays originating in the core area and hitting the aperature area of the in-pool collimator and scattering into the detector. These angles explain the width of the Compton scattered component of the 7725 and 2223 keV gamma ray lines. Initially the in-pool collimator was water filled between the ^{6}LiF neutron absorbers. After the initial trial run on the facility, the water was replaced by an air filled thin walled aluminum container in order to reduce the material which can be used for scattering off of. This cut down the background peaks by approximately 5 to 10 times. Figure 2-15 was obtained after this modification.

Table 2-1

System Background

Energy(keV)	Rate(counts/min)	Width of Line(keV)
1778	0.99	4-6
2223	7.4	7 + 90 keV continuum extending downwards
2948	0.68	30-40
3110	0.69	30-40
3447	0.34	30-40
3579	0.13	30-40
4110	0.58	30-40

Energy	Rate	Width of Line
4237	0.56	30-40
4685	0.77	30-40
4886	0.33	30-40
7656	1.93	30-40
7725	0.36	10-12 + continuum extending downward

2-8 Doppler Broadening Effects

When fast neutrons (1 to 10 MeV) interact with atoms in a target, they transfer typically 10 to 200 keV of kinetic energy to the atom according to the laws of conservation of energy and momentum. The resultant motion of the nucleus produces a Doppler shift in the energy of the gamma rays, which are emitted while the nucleus is in motion. For each set of given initial conditions there is a distribution of velocities of the target nucleus and hence a distribution of possible energy shifts of the resultant gamma rays. This leads to a broadening of the gamma ray peaks produced in the $(n,n'\gamma)$ reaction. Figure 2-16 shows a small portion of a spectrum obtained for the reactions $^{27}Al(n,\gamma)^{28}Al$ and $^{27}Al(n,n'\gamma)^{27}Al$. The radiation arising from the inelastic reaction is Doppler broadened and is indicated by arrows in the figure. The peaks due to the capture reaction display the peak width which is characteristic of the system resolution.

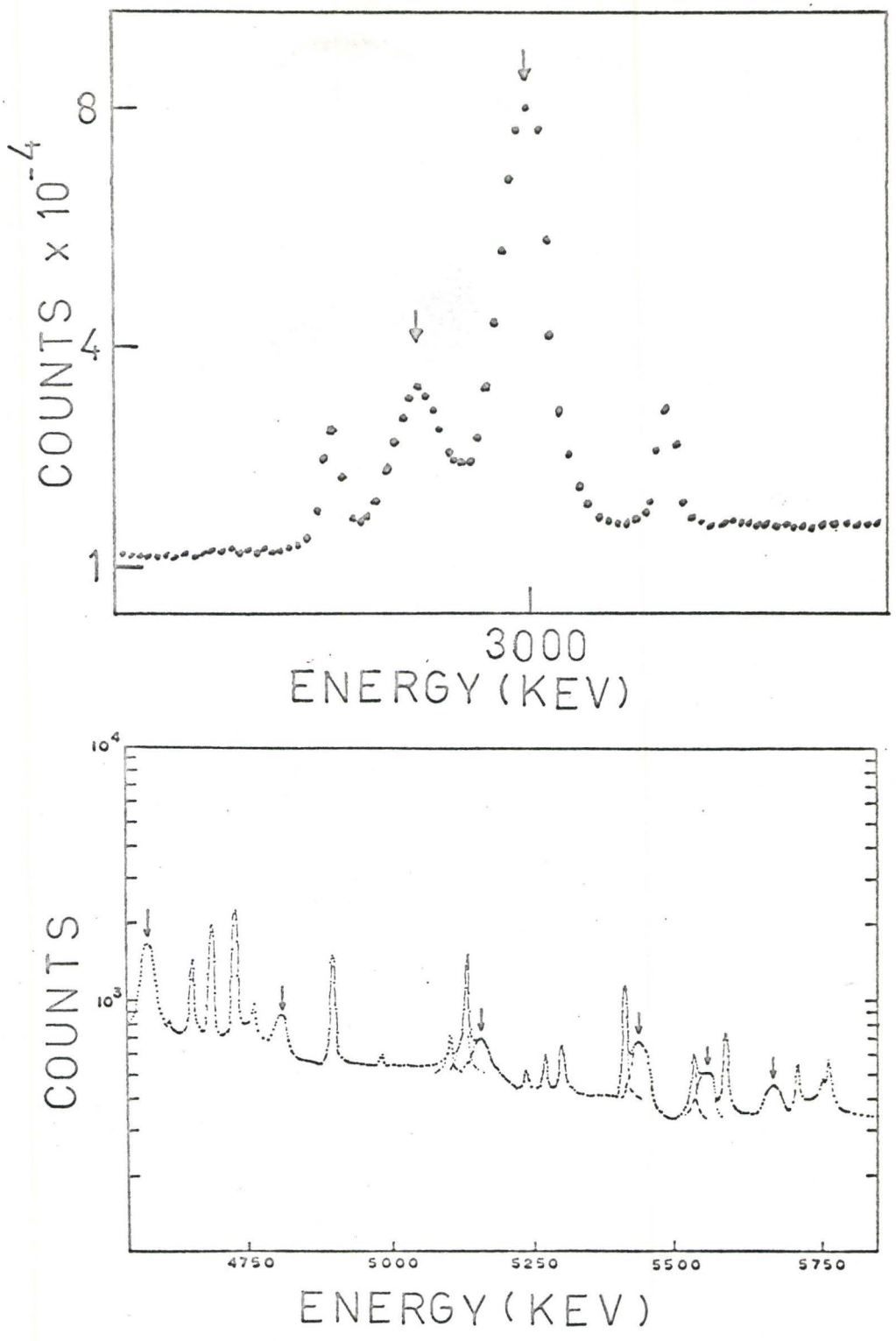

Figure 2-16 A portion of the aluminum spectrum. The radiation arising from inelastic scattering is Doppler broadened and is indicated with arrows. The capture components show the usual peak width characteristic of the system resolution.

In order to understand the experimental results and their limitations, a model for the system has been derived. The model assumes that the complex geometric convolution factors can be approximated by assuming that the incident neutron flux is isotropic, and that the target nuclei recoil isotropically in the center of mass co-ordinate system. The gamma rays are assumed to be emitted isotropically in the center of mass system as well. In addition to the geometric factors, a quantitative estimate of the reaction parameters is necessary. The neutron spectrum is assumed to be an unmodulated fission spectrum of the form $\phi(E_n) \sim \exp(-\alpha E_n)$ with $\alpha = 0.77$ MeV^{-1}. The inelastic neutron scattering cross section is approximated by Donahue's expression [35]

$$\sigma(E_n) \sim (1 - \exp-\beta(E_n - E_x)),$$

where E_n is the center of mass neutron energy, E_x is the level energy, $\beta = 3$ MeV^{-1} and $E_n > E_x$. The reaction rate as a function of energy is thus given by

$$R(E_n) \sim (1 - \exp-\beta(E_n - E_x)).\exp(-\alpha.E_n).$$

The mean value of the neutrons entering into this reaction in the laboratory system of energy is given by

$$\bar{E}_n = (E_x + \frac{\alpha + 2\beta}{\beta(\alpha + \beta)}).\frac{(A + 1)^2}{A^2}$$

$$= (E_x + 1.56).\frac{(A + 1)^2}{A^2} \quad \text{MeV}.$$

The most probable neutron energy is given by

$$\hat{E}_n = (E_x + \frac{1}{\alpha}.\ln(\frac{\alpha + \beta}{\beta})).(\frac{A + 1}{A^2})^2$$

$$\hat{E}_n = (E_x + 0.53).\left(\frac{A+1}{A^2}\right)^2 \text{ MeV.}$$

Both of these may be represented by the expression

$$E_n = (E_x + \Delta).\left(\frac{A+1}{A^2}\right)^2 \text{ MeV.},$$

with $\Delta = 1.56$ or 0.53.

The incident energy in the laboratory system is given by $E_n = \frac{1}{2}.m.V_n^2$, where V_n is the velocity of the neutron in the laboratory system. Before the collision the energy in the center of mass co-ordinate system is

$$\frac{1}{2}.m.(V_n - V_c)^2 + \frac{1}{2}.M.V_c^2 = \frac{A}{A+1}.E_n ,$$

where A is the mass of the target nucleus, V_c is the velocity of the center of mass and M is the total mass of the system. After the collision the energy is given by

$$E_x + \frac{1}{2}.m.V_{n'}^2 + \frac{1}{2}.M.V_A^2 = E_x + \frac{1}{2}.m.A.V_A^2.(A+1),$$

where $V_{n'}$ is the velocity of the recoil neutron and V_A is the velocity of the recoil nucleus. The conservation of energy states these two energies are equal. Thus

$$E_x = \frac{1}{2}.m.(A+1).A.(V_c^2 - V_A^2).$$

Since $V_c = V_n/(A+1) = \frac{1}{A+1}.\sqrt{\frac{2.E_n}{m}}$, the previous equation can be rearranged to obtain

$$V_A = \sqrt{\frac{2.E_n}{m(A+1)^2} - \frac{2.E_x}{m.A.(A+1)}} .$$

The transformation from the center of mass system of co-ordinates to the laboratory system is given by

$$V_\ell^2 = V_c^2 + V_A^2 + 2.V_A.V_c.\cos\phi_c \quad \text{and}$$

$$\tan\phi_\ell = \frac{V_A.\sin\phi_c}{V_A.\cos\phi_c + V_c},$$

where ϕ_c is the angle of scattering in the center of mass system, ϕ_ℓ is the angle of scattering in the laboratory system and V_ℓ is the recoil velocity of the target nucleus in the laboratory system.

To calculate the Doppler broadening it is necessary to determine the probability distribution function $P(V_\ell)$. If the target nuclei recoil isotropically, then

$$P(\phi_c) = \frac{1}{2}.\sin\phi_c . \qquad \text{Thus}$$

$$P(V_\ell) = P(\phi_c).\frac{d\phi_c}{dV_\ell} = \frac{V_\ell}{2.V_A.V_c}$$

and $\quad (V_c - V_A) \leq V_\ell \leq (V_A + V_c).$

If the gamma radiation is emitted at an angle from the recoil direction, then the energy shift is given by $\Delta E_\gamma = E_X.\frac{V_\ell}{c}.\cos\Psi$. If the gamma rays are emitted isotropically, then $P(\Psi) = \frac{1}{2}.\sin\Psi$. The probability distribution of ΔE_γ for a given V_ℓ is

$$P(\Delta E_\gamma | V_\ell) = P(\Psi).\frac{d\Psi}{d(\Delta E_\gamma)} = \frac{c}{2.E_\gamma.V_\ell} .$$

Since $P(V_\ell)$ has been calculated, the distribution becomes

$$P(\Delta E_\gamma) = \int_{\frac{c\Delta E_\gamma}{E_\gamma}}^{V_c+V_A} \frac{c}{2.E_\gamma.V_\ell} \cdot \frac{V_\ell}{2.V_A.V_c} \cdot dV_\ell$$

$$= \frac{c}{4.E_\gamma.V_A.V_c} \cdot \left(V_A + V_c - \frac{c.\Delta E_\gamma}{E_\gamma}\right).$$

The full width at half maximum of the $P(\Delta E_\gamma)$ distribution is given by

$$\Delta E)_{fwhm} = \frac{E_\gamma}{c} \cdot (V_A + V_c).$$

V_A and V_c have been given in terms of E_n and E_X previously. If mean or most probable neutron energies are used and if only ground state transitions are used ($E_\gamma = E_X$), then the full width at half maximum of the gamma ray peaks becomes $\Delta E)_{fwhm} = \sqrt{\frac{2}{931}} \cdot \frac{E_\gamma}{A} \cdot \left(\sqrt{\frac{E_\gamma + \Delta(A+1)}{(A+1)}} + \sqrt{E_\gamma + \Delta} \right)$.

In the $(n,n'\gamma)$ reactions studied the mass number A varied by a factor of 4 and the energy by a factor of 8. Figure 2-17 gives the results of a study of the variation in peak width with A and E_γ. The experimental values of ΔE have been divided by the calculated value given above. The two dotted lines give the theoretical values for the two choices of parameters $\bar{E}_n$ and $\hat{E}_n$. Excellant agreement is obtained if $\bar{E}_n$ is used. The average value of the experimental points is 0.93.

2-9 Sample Position and Energy Shift

The reactor is a source of gamma rays as well as a neutron source. The wide angle subtended by the core leads to a broad energy spread when radiation is scattered from the target. Since the energy of the scattered radiation is given by

$$E'_\gamma = \frac{E_\gamma}{1 + (1-\cos\theta) \cdot \frac{E_\gamma}{mc^2}},$$

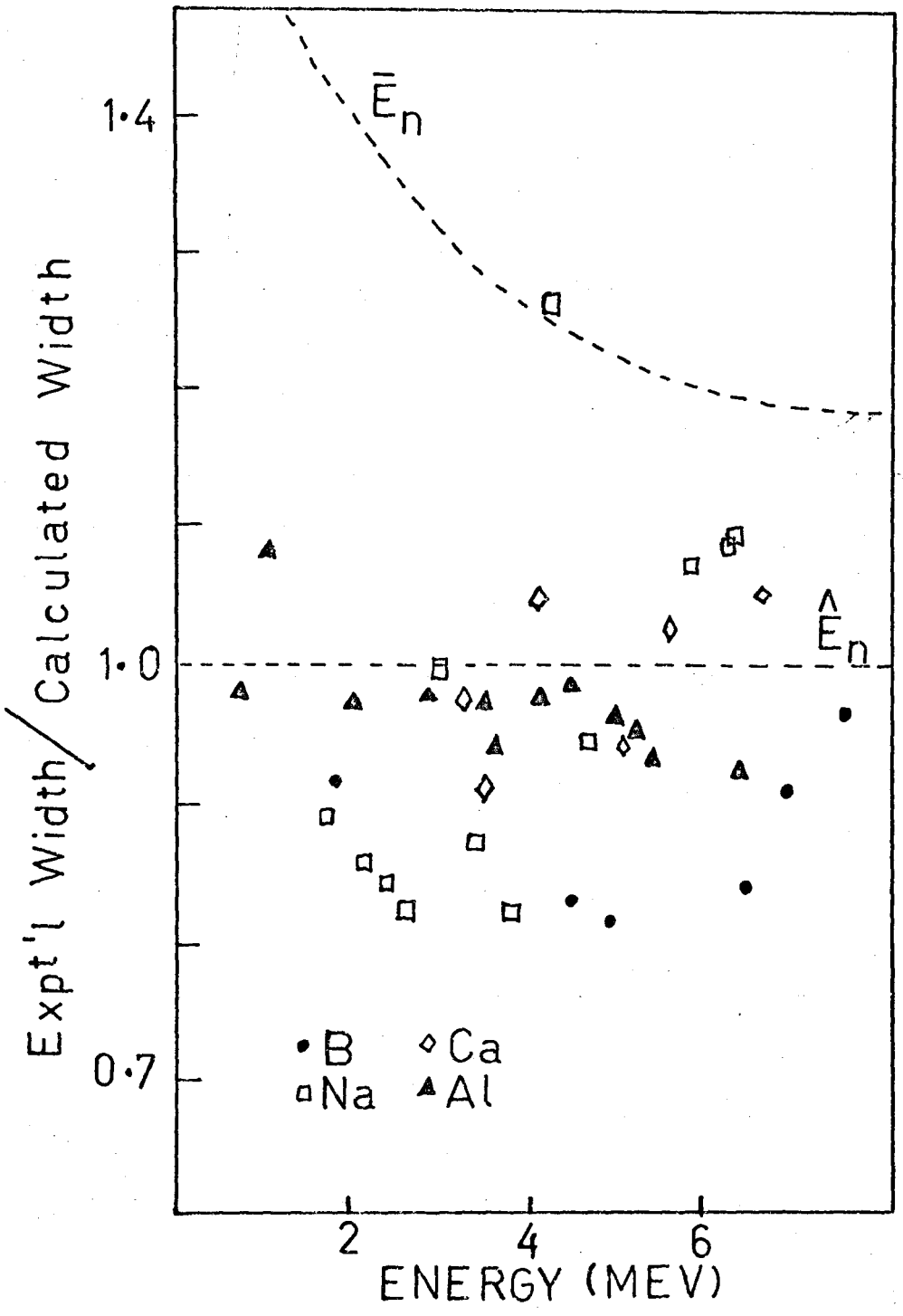

Figure 2-17 Doppler Broadening Results.

it can be seen that the target position has a pronounced effect upon the spectrum of radiation scattered down the beam. If the target is placed in the target position indicated in figure 2-1, at the edge of the core remote from the detection system, then the gamma rays are scattered through large angles with the result that the scattered gamma ray spectrum is compressed into the energy range 0 to 511 keV. The gain in overall sensitivity by using this target position more than compensates for the small (~20%) loss in neutron flux compared to a target position opposite the center of the core. Thus targets used for this work were typically of the order of 3 to 6 inches in length and 1 inch in diameter and were placed beside the last 6 inches of the core. Figures 2-18 and 2-19 show the result of placing a 4 inch long aluminum sample at the target position at the back edge of the core and also at the edge of the core nearest the detector system. Figure 2-18 is the result of operating the detection system in the singles mode. The lower electronic threshold for the case with the sample at the back edge of the core had to be set high to limit the dead time on the analyzer due to the high rate at low gamma ray energy. Figure 2-19 shows the same samples done using the pair mode of operation. The gain in overall sensitivity accomplished by placing the target at the back edge of the reactor thereby reducing the general Compton scattered background

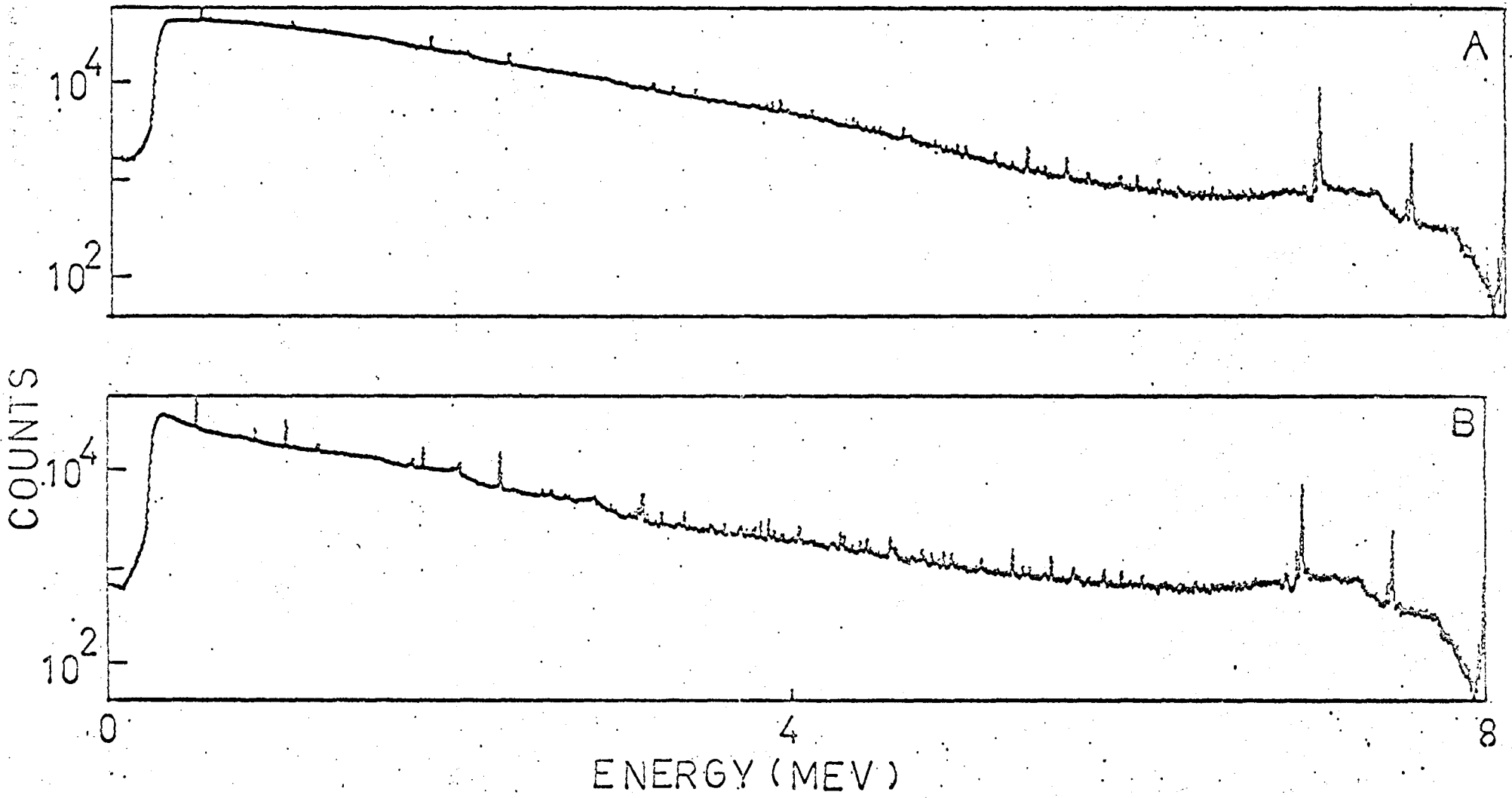

Figure 2-18 Singles mode spectrum for an aluminum sample located at the front edge (A) and at the back edge (B) of the reactor core.

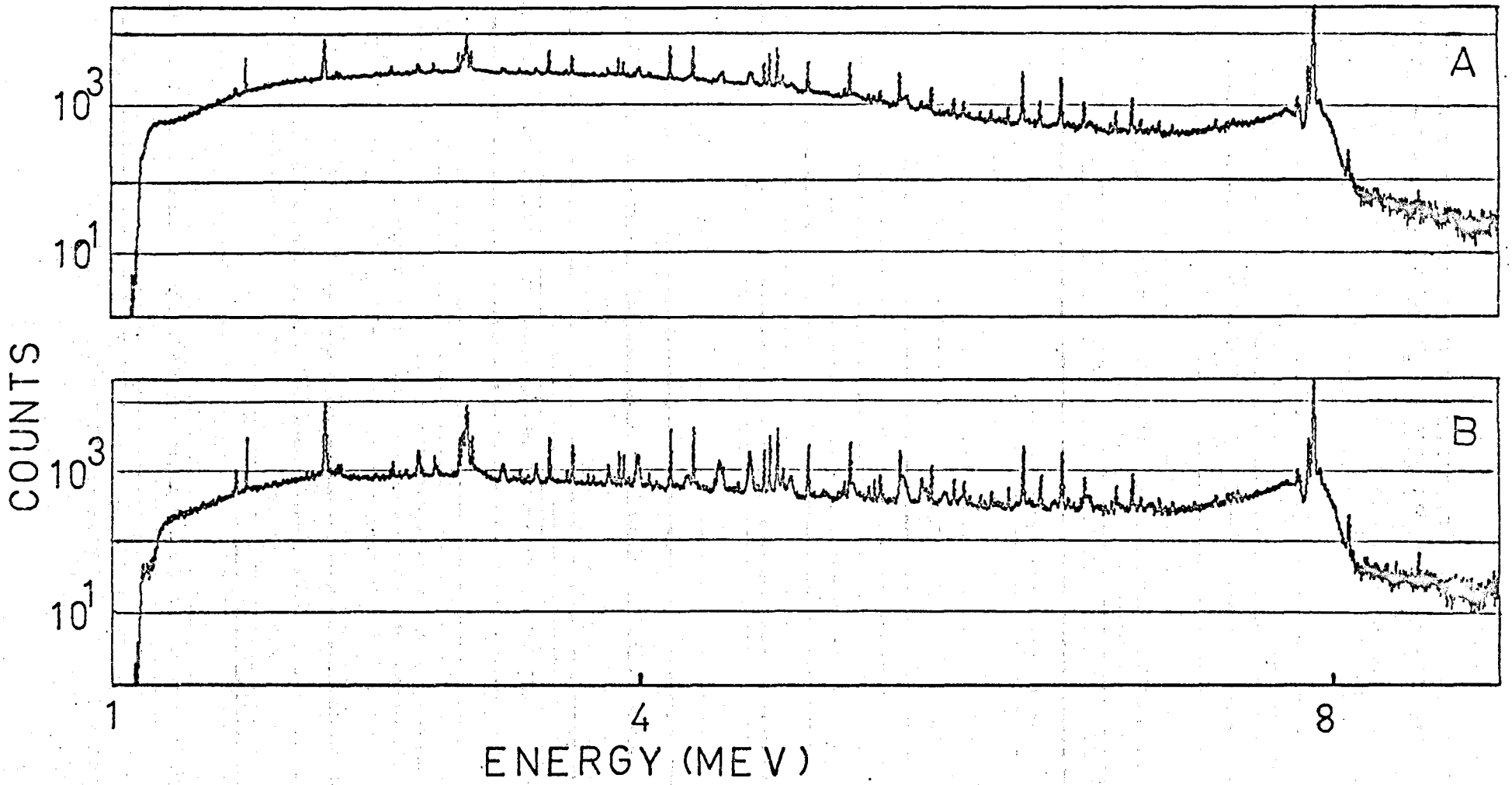

Fig. 2-19 Pair mode spectrum for an aluminum sample located at the front edge (A) and at the back edge (B) of the reactor core.

at energies above 500 keV can be easily seen. The gain in sensitivity using the pair mode of operation compared to the singles mode is also obvious. The results for the aluminum sample were obtained using only a cadmium filter. As a result of this, there is a significant gamma ray contribution to the overall spectrum due to the (n,γ) reaction. This component is readily identified since the resolution of these peaks is limited by the response of the detector. Gamma ray peaks due to the inelastic neutron reaction are Doppler broadened.

A serious drawback to the position chosen to locate the targets is that there is a net energy shift of the gamma rays. This is caused by the fact that the neutrons are not entirely isotropic but are peaked about some incidence angle slightly off from 90°. Figure 2-20 shows the algebraic difference between the two sets of results given in figure 2-19. The gains for the two experiments were identical and the number of counts in the 7725 keV gamma ray peak was equal and as a result the gamma rays originating in the (n,γ) reaction cancelled. The peaks due to the inelastic reaction appear to be bipolar because of the net energy shift between the two locations. Several of the larger inelastic gamma ray lines were deleted to make the illustration clearer. The general pattern is caused by the difference in the Compton scattered background radiation.

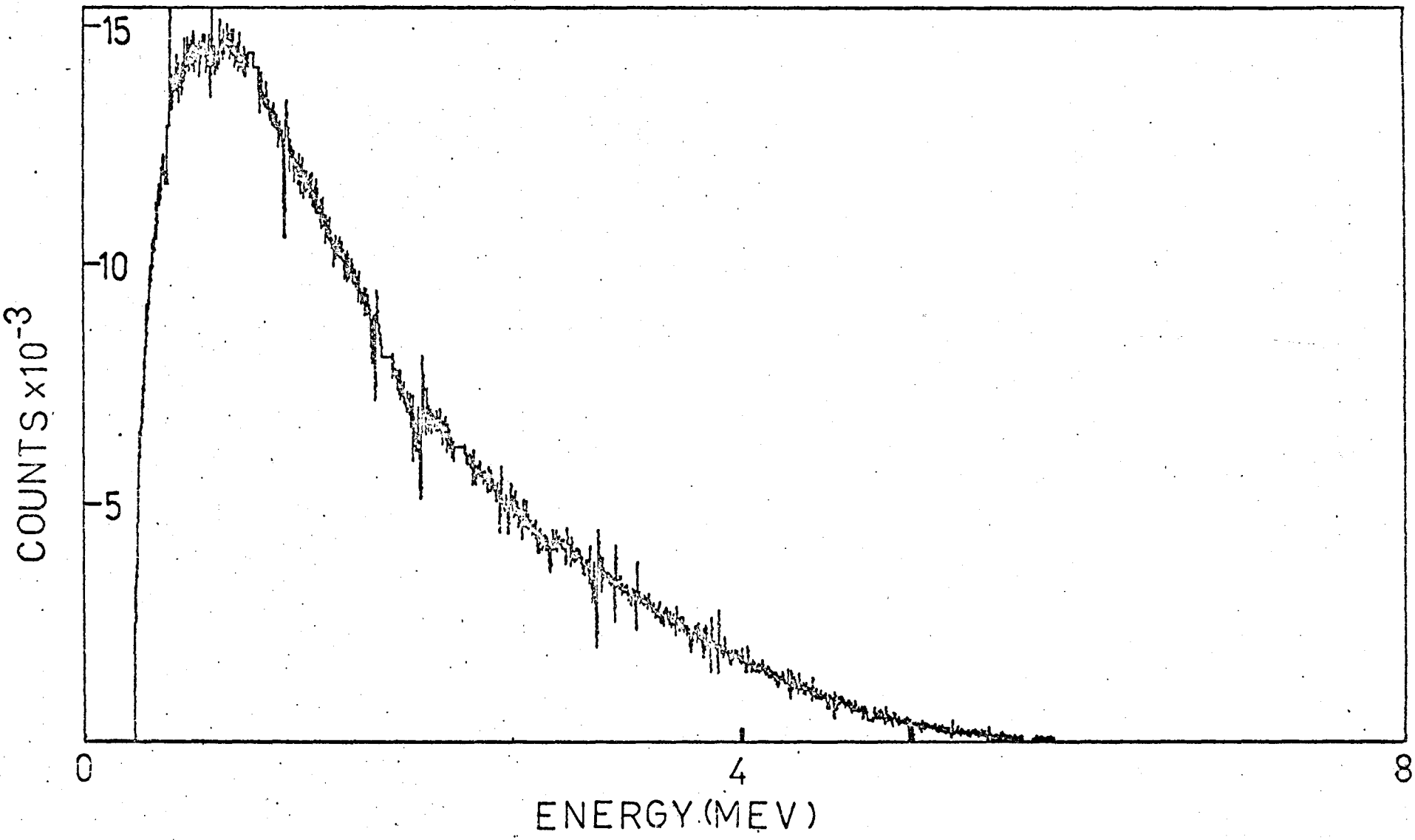

Fig. 2-20 The result of taking the algebraic difference of A and B spectra of Fig. 2-18. The bipolar peaks indicate an energy shift for lines due to the inelastic reaction and the general shape is due to scattered radiation.

The net energy shift produced by placing samples at each end of the core is given by

$$\Delta E_\gamma = 2.E_X.\frac{\bar{v}_\ell}{c}.\cos\Psi \ ,$$

where $\bar{v}_\ell$ is the average recoil velocity and Ψ is the effective incident neutron angle relative to the collimator axis. An examination of the conservation laws reveals $\bar{v}_\ell \approx V_c$. The value for V_c is given by

$$V_c = \frac{1}{A+1} \cdot \sqrt{\frac{2.E_n}{m}} = \frac{1}{A} \cdot \sqrt{\frac{2(E_x+\Delta)}{m}},$$

if the average or most probable neutron energy is used. Thus the shift is given by

$$\Delta E_\gamma = \frac{2.E_x}{A} \cdot \sqrt{\frac{2(E+\Delta)}{931}} \cdot \cos\Psi.$$

This expression can be integrated over the length of the sample to predict the net energy shift. Figure 2-21 shows the experimental values of the energy shift for ground state transitions in aluminum. The solid line gives the calculated values using the value of Ψ which gives the best fit. The angle Ψ is very dependent upon the sample position as indicated in the insert of figure 2-21. The general agreement between the model and the experimental data is good considering that the E_X and A dependence are fixed by the equations and the range of $\cos\Psi$ is limited by the geometry of the reactor. The equation for the energy shift has been used to correct all the gamma ray energies given in subsequent chapters of this work. Since the true unshifted energy would be obtained opposite the center of

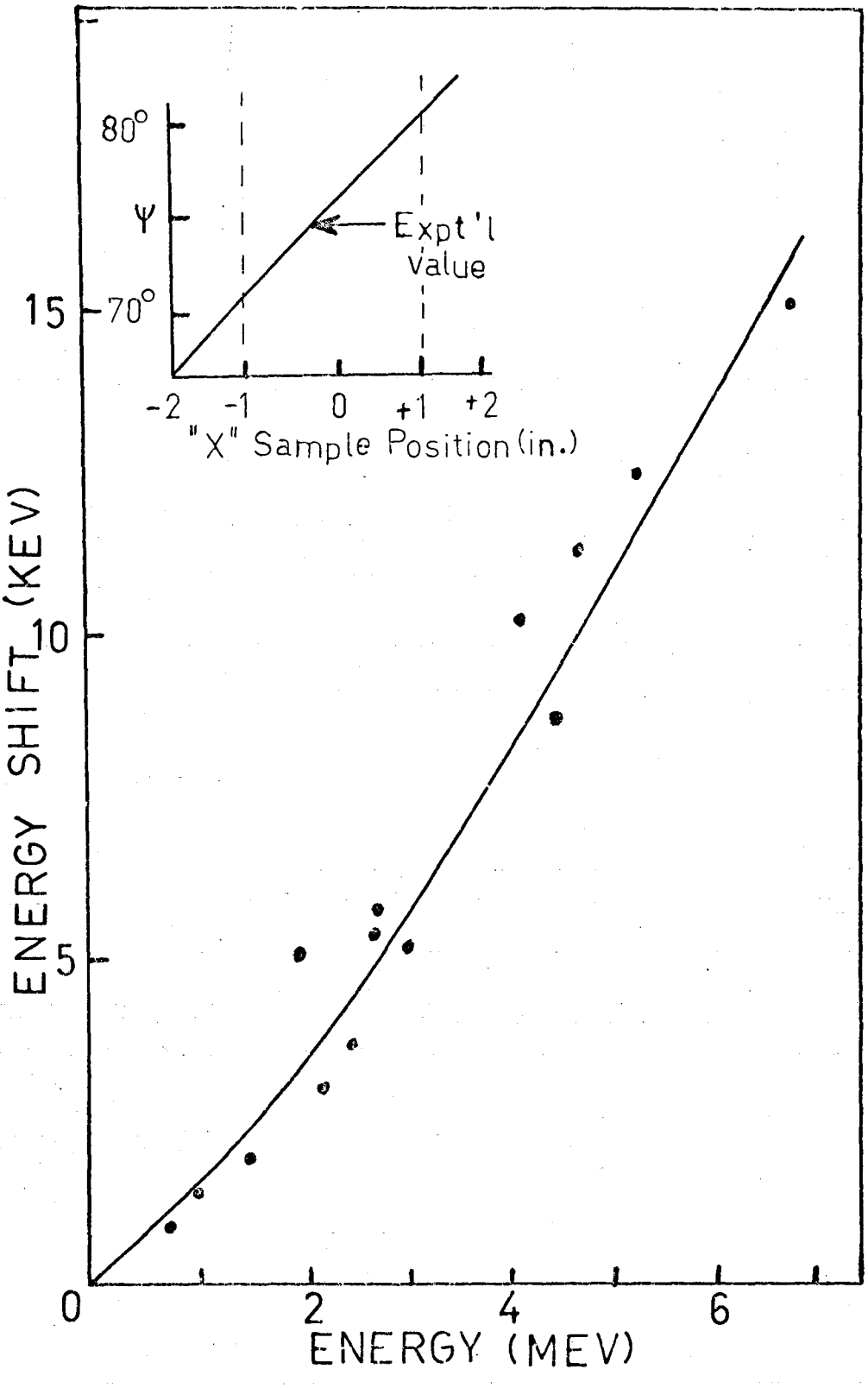

Figure 2-21 Energy Shift due to Doppler Effects. The graph displays the energy difference for an aluminum sample placed at the front and back edges of the reactor core.

the core the shift is divided by a factor of two.

2-10 Sample Form

In choosing the form of sample to use there are a number of important experimental limitations. Since most samples would be heated up to a few hundred degrees Centigrade depending on the material used, the melting point or decomposition point of any sample used must be quite high. Reactor safety dictates that the samples must not be reactive with air or water at the elevated temperature in case of any vacuum failure while the target chamber is in position. Materials which were water soluble were encapsulated in thin walled aluminum containers. This led to background gamma radiation which was frequently used for calibration. Disposal of the irradiated samples implies that the half life and decay mode of the activated samples must be considered. In order to satisfy these requirements, it was necessary to choose stable compounds containing the desired elements. Since several elements were thus studied concurrently it was necessary to study several compounds containing each element to separate the various components. Fluorides were chosen since they are very stable and are easy to obtain. In addition fluorides were chosen in order to study the effect of stopping power on the Doppler broadening. The samples studied were Si, Al, BP, B, melamine, LiF, NaF, CaF_2 and PbF_2.

CHAPTER 3

TYPICAL HAUSER FESHBACH CALCULATIONS

3-1 Introduction

The cross section for a given level as a function of energy using the Hauser Feshbach formalism is given by

$$\sigma(E) = \pi \lambda^2 \sum_{\substack{J j l \\ j' l'}} \frac{(2J+1)}{2(2I+1)} \cdot T^{J}_{\alpha j l} \cdot \frac{T^{J}_{\alpha' j' l'}}{\sum_{\alpha'' j'' l''} T^{J}_{\alpha'' j'' l''}} \quad .$$

One of the chief problems in applying this formula to the $(n,n'\gamma)$ reaction using reactor neutrons, is the fact that the cross section for one level depends on the branching from the intermediate state to all other levels which have their threshold energy below the available energy. A second problem is that the decay scheme and branching ratios must be well known in order to correct for the population of a level due to the decay of other levels of higher energy. In order to minimize these problems, it was decided to study some of the lighter elements in this work. The experimental facility is somewhat limited for low energy gamma rays below 600 keV due to the large amount of Compton scattered radiation coming from the targets. In addition, the neutron absorbers reduce the sensitivity of the system at low energy. The detection system is also limited at low energies since the Compton suppression mode is less effective. However light elements do not have complicated decay schemes and have relatively few low energy

gamma rays in their decays schemes and thus are easier to work with.

The determination of the total cross section for given levels of a nucleus was accomplished by placing a target beside the reactor core, thereby averaging over a large range of angles. The intensity and energies of the gamma rays emitted were then recorded. The energy information, along with other experimental results obtained by previous experimenters was used to determine the decay scheme. The intensities were used to obtain values for the yield or population of the various levels in the target nucleus. The intensities also provided branching ratios which are useful aids in predicting spins and parities of levels.

For energies above 1 MeV, the reactor spectrum of neutrons can be approximated by $\phi(E) = \phi_o \exp(-\alpha E)$. The constant α depends on the amount of water and other material located between the sample and the reactor core. A pure fission spectrum can be approximated by $\alpha = 0.77$ MeV^{-1}. The data given in Research Reactors[47] suggests a value of α in the range 0.65 to 0.75 MeV^{-1}. In handling the silicon data, several values of α were tried to get the best overall agreement with known spins and parities. It was found that the best value was $\alpha = 0.70$ MeV^{-1}. The fission spectrum can also be fitted by the function[48]

$$\phi(E) = \sinh(2.E)^{\frac{1}{2}}.\exp(-E).$$

This form does not appear to give a good an agreement as the simple exponential although it does predict the drop in population observed for the very low energy levels.

The primary population of a level after correcting for decays from other levels is given by

$$P = \int \sigma(E).\phi(E).dE \quad \text{or} \quad \sum_i \sigma_i(E).\phi_i(E).$$

Since the values of the transmission coefficients used to calculate $\sigma(E)$ were obtained from a table, the finite sum formula was applied. The energy range was divided up into finite steps and level energies were rounded off to the nearest step. Several grid sizes or energy divisions were tried until changing the grid size by 50% had less than a 5% effect on the predicted population values in general. The step size chosen was 200 keV. Since the population versus energy for a given level always tends to peak at 0.5 MeV above threshold it was possible to get a good value for the population of the levels by taking the energy range to extend up to 3 MeV above the highest state observed.

3-2 Predicted Population Values for ^{28}Si

In order to use the Hauser Feshbach formalism, one must first draw up a table of possible spin combinations for each level of interest using the restrictions given in chapter 1. Table 3-1 shows the permitted spin combinations for a transition from the 0^+ ground state of ^{28}Si to a 2^+ excited state.

Table 3-1

Neutron Angular Momenta
for a 0^+ to 2^+ Excitation

ℓ	$\ell+s$	$J\pi$	ℓ'	$\ell'+s$	ℓ	$\ell+s$	$J\pi$	ℓ'	$\ell'+s$
0	1/2	1/2+	2	3/2	3	5/2	5/2-	1	1/2
			2	5/2				1	3/2
								3	5/2
								3	7/2
1	1/2	1/2-	1	3/2					
			3	5/2	3	7/2	7/2-	1	3/2
								3	5/2
1	3/2	3/2-	1	1/2				3	7/2
			1	3/2					
			3	5/2	4	7/2	7/2+	2	3/2
			3	7/2				2	5/2
								4	7/2
2	3/2	3/2+	0	1/2				4	9/2
			2	3/2					
			2	5/2	4	9/2	9/2+	2	5/2
			4	7/2				4	7/2
								4	9/2
2	5/2	5/2+	0	1/2					
			2	3/2					
			2	5/2					
			4	7/2					
			4	9/2					

The primed quantities refer to angular momenta after the reaction. J is the spin of the intermediate state. The ℓ values considered range from 0 to 4 for both the entrance and exit channels. For this example it is assumed that there is only one possible level other than the ground state, so that the double primed sum in the cross section equation consists of only two terms, for each given intermediate state. Since the parity is not changed in the overall reaction, the parity of ℓ' in each case must be the same as the parity of the corresponding ℓ in order to conserve parity. The following equation gives the cross section for

a 0+ to 2+ excitation as a function of energy. The intermediate spin and parity are given in brackets at the right for each term.

$$\frac{2}{\pi\lambda^2}\cdot\sigma(E;0+\text{ to }2+) = \frac{2\cdot T_0^{1/2}(E)\cdot[T_2^{3/2}(E') + T_2^{5/2}(E') + T_4^{5/2}(E')]}{T_0^{1/2}(E) + T_2^{3/2}(E') + T_2^{5/2}(E') + T_4^{5/2}(E')} \quad (1/2+)$$

$$+ \frac{2\cdot T_1^{1/2}(E)\cdot[T_1^{3/2}(E') + T_3^{5/2}(E')]}{T_1^{1/2}(E) + T_1^{3/2}(E') + T_3^{5/2}(E')} \quad (1/2-)$$

$$+ \frac{4\cdot T_1^{3/2}(E)\cdot[T_1^{1/2}(E') + T_1^{3/2}(E') + T_3^{5/2}(E') + T_3^{7/2}(E')]}{T_1^{3/2}(E) + T_1^{1/2}(E') + T_1^{3/2}(E') + T_3^{5/2}(E') + T_3^{7/2}(E')} \quad (3/2-)$$

$$+ \frac{4\cdot T_2^{3/2}(E)\cdot[T_0^{1/2}(E') + T_2^{3/2}(E') + T_2^{5/2}(E') + T_4^{7/2}(E')]}{T_2^{3/2}(E) + T_0^{1/2}(E') + T_2^{3/2}(E') + T_2^{5/2}(E') + T_4^{7/2}(E')} \quad (3/2+)$$

$$+ \frac{6\cdot T_2^{5/2}(E)\cdot[T_0^{1/2}(E') + T_2^{3/2}(E') + T_2^{5/2}(E') + T_4^{7/2}(E') + T_4^{9/2}(E')]}{T_2^{5/2}(E) + T_0^{1/2}(E') + T_2^{3/2}(E') + T_2^{5/2}(E') + T_4^{7/2}(E') + T_4^{9/2}(E')} \quad (5/2+)$$

$$+ \frac{6\cdot T_3^{5/2}(E)\cdot[T_1^{1/2}(E') + T_1^{3/2}(E') + T_3^{5/2}(E') + T_3^{7/2}(E')]}{T_3^{5/2}(E) + T_1^{1/2}(E') + T_1^{3/2}(E') + T_3^{5/2}(E') + T_3^{7/2}(E')} \quad (5/2-)$$

$$+ \frac{8\cdot T_3^{7/2}(E)\cdot[T_1^{3/2}(E') + T_3^{5/2}(E') + T_5^{7/2}(E')]}{T_3^{7/2}(E) + T_1^{3/2}(E') + T_3^{5/2}(E') + T_5^{7/2}(E')} \quad (7/2-)$$

$$+ \frac{8\cdot T_4^{7/2}(E)\cdot[T_2^{3/2}(E') + T_2^{5/2}(E') + T_4^{7/2}(E') + T_4^{9/2}(E')]}{T_4^{7/2}(E) + T_2^{3/2}(E') + T_2^{5/2}(E') + T_4^{7/2}(E') + T_4^{9/2}(E')} \quad (7/2+)$$

$$+ \frac{10\cdot T_4^{9/2}(E)\cdot[T_2^{5/2}(E') + T_4^{7/2}(E') + T_4^{9/2}(E')]}{T_4^{9/2}(E) + T_2^{5/2}(E') + T_4^{7/2}(E') + T_4^{9/2}(E')}. \quad (9/2+)$$

E' is the energy difference between the intermediate state and the final state. E is the incident neutron energy.

Figure 3-1A illustrates the predicted cross section of the 2+ 1778 keV level in ^{28}Si versus neutron energy using the above equation. The upper curve gives the result if no other levels other than itself and the ground state are considered. The lower curve includes the effects of all known levels on the calculations. The effect of extra levels is that extra transmission coefficients are added into the denominator of each term of the cross section equation.

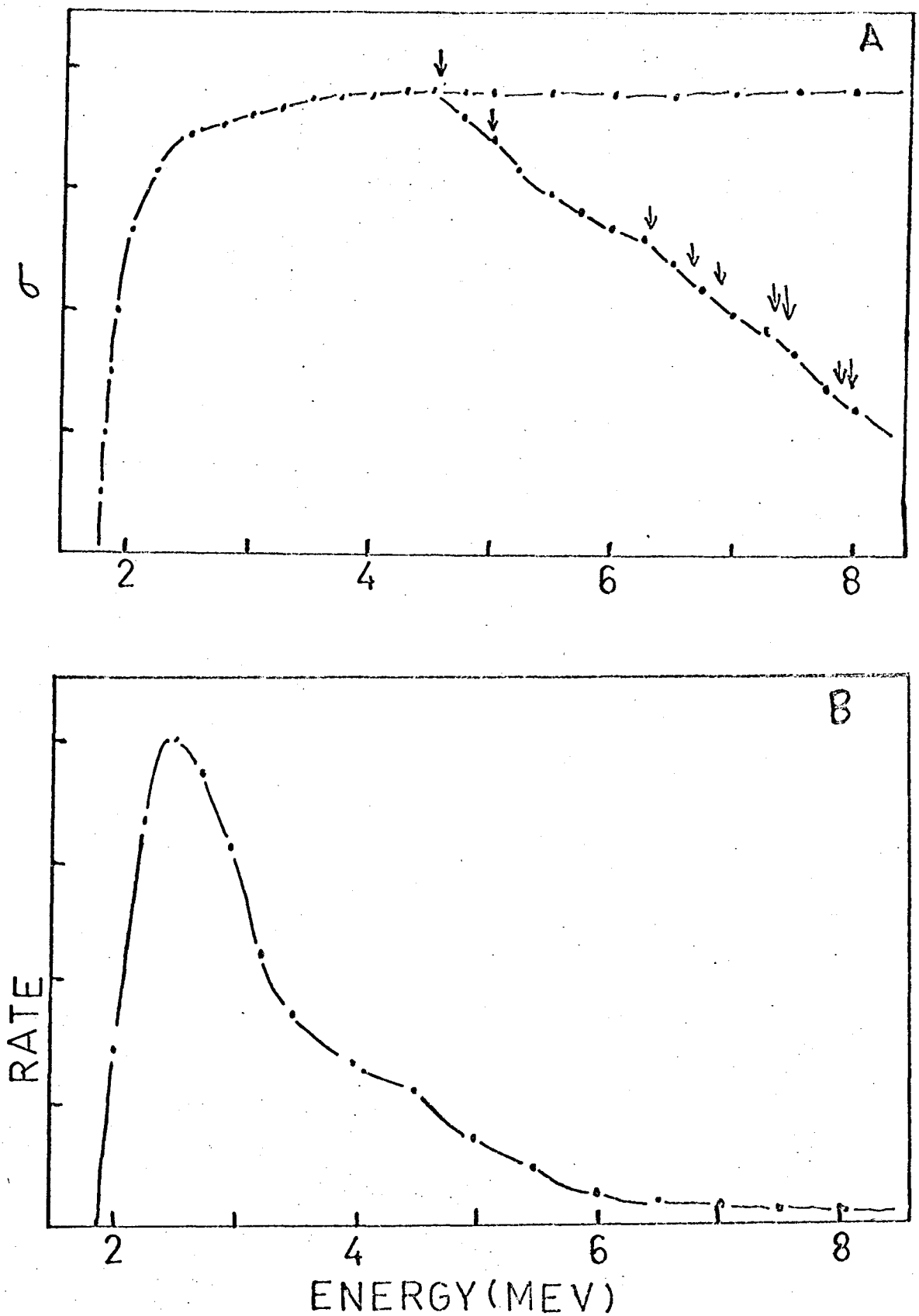

Figure 3-1 The Calculated Cross Section (A) and Rate (B) Versus Energy for the 2 +, 1778 keV Level in ^{28}Si. In (A) the upper curve gives the result if other levels are ignored in the calculation. In (A) the arrows indicate the presence of the other levels.

The arrows in the illustration indicate the known energy levels and their spins and parities. Figure 3-1B shows the population of the state as a function of energy. Due to the fact that the higher energy states in ^{28}Si are more than 2 MeV higher in energy, they have very little effect on the population of the 1778 keV level. Figures 3-2A and 3-2B give the calculated cross section as a function of energy for the 1778 keV level up to 5 MeV for various choices of spins and parities. The effects of the 4614 keV level have not been included in this calculation. The results of this calculation indicates that the results are not very sensitive to parity. This result is true in general, except for level energies below 1.5 MeV. However the calculations are very sensitive to spin values. Figure 3-2C shows the calculated population values as a function of energy. The different spins tend to produce pairs of curves lying close together. For example, the values of the 1+ and 2+ cases produce similar values as do the 0+ and 3+ cases. The total populations up to 5 MeV of the 2+,3+ and 4+ cases are 2.84, 1.99 and 0.86 units respectively.

Figures 3-3A and 3-3B display the cross section and population values as functions of energy for several typical higher energy levels in ^{28}Si. Results are given for the calculations assuming there is branching to all known levels, and also assuming there is only one level present.

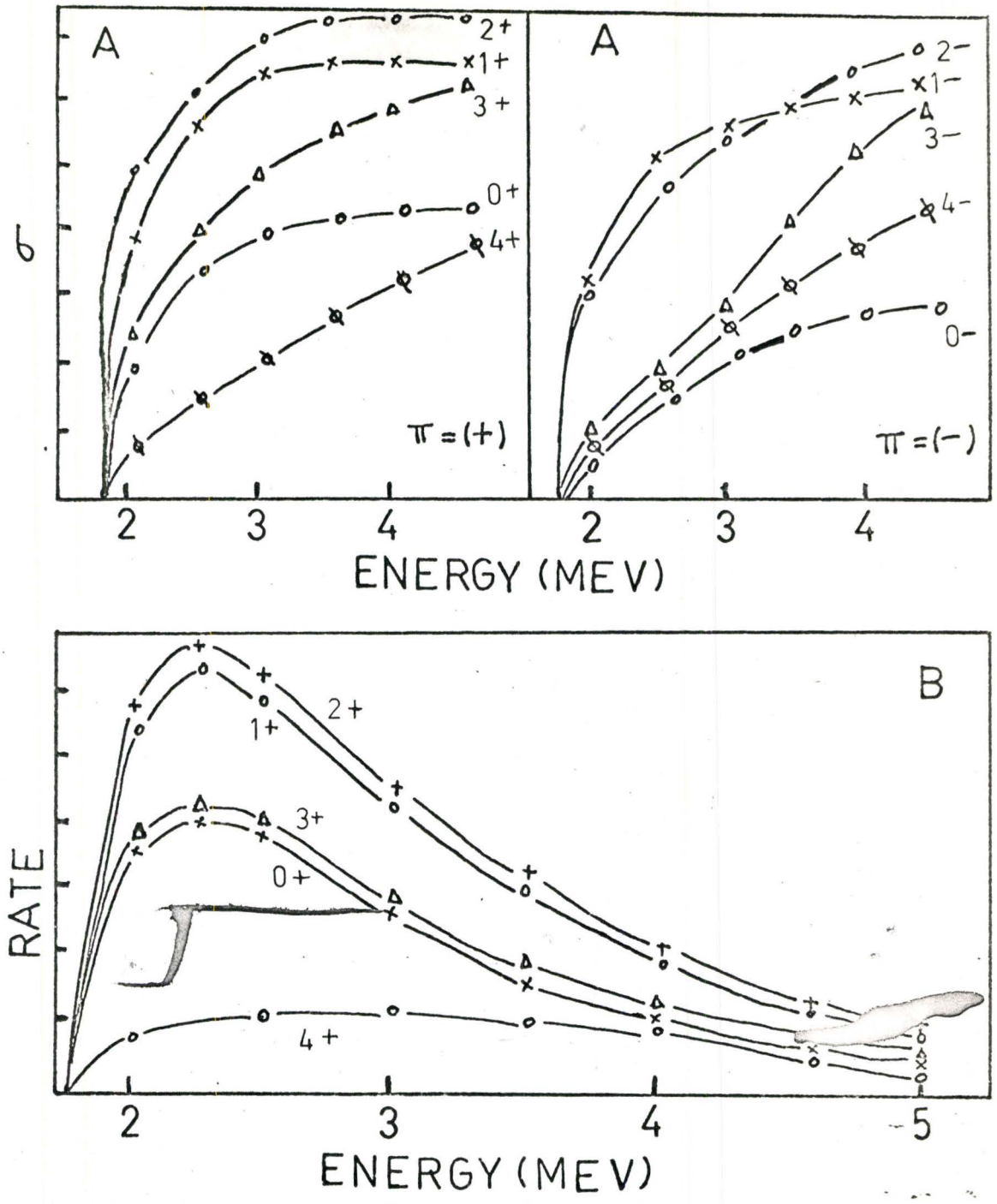

Figure 3-2 The calculated cross section(A) and Rate(B), for various choices of spin, versus energy for the 1778 keV level in ^{28}Si.

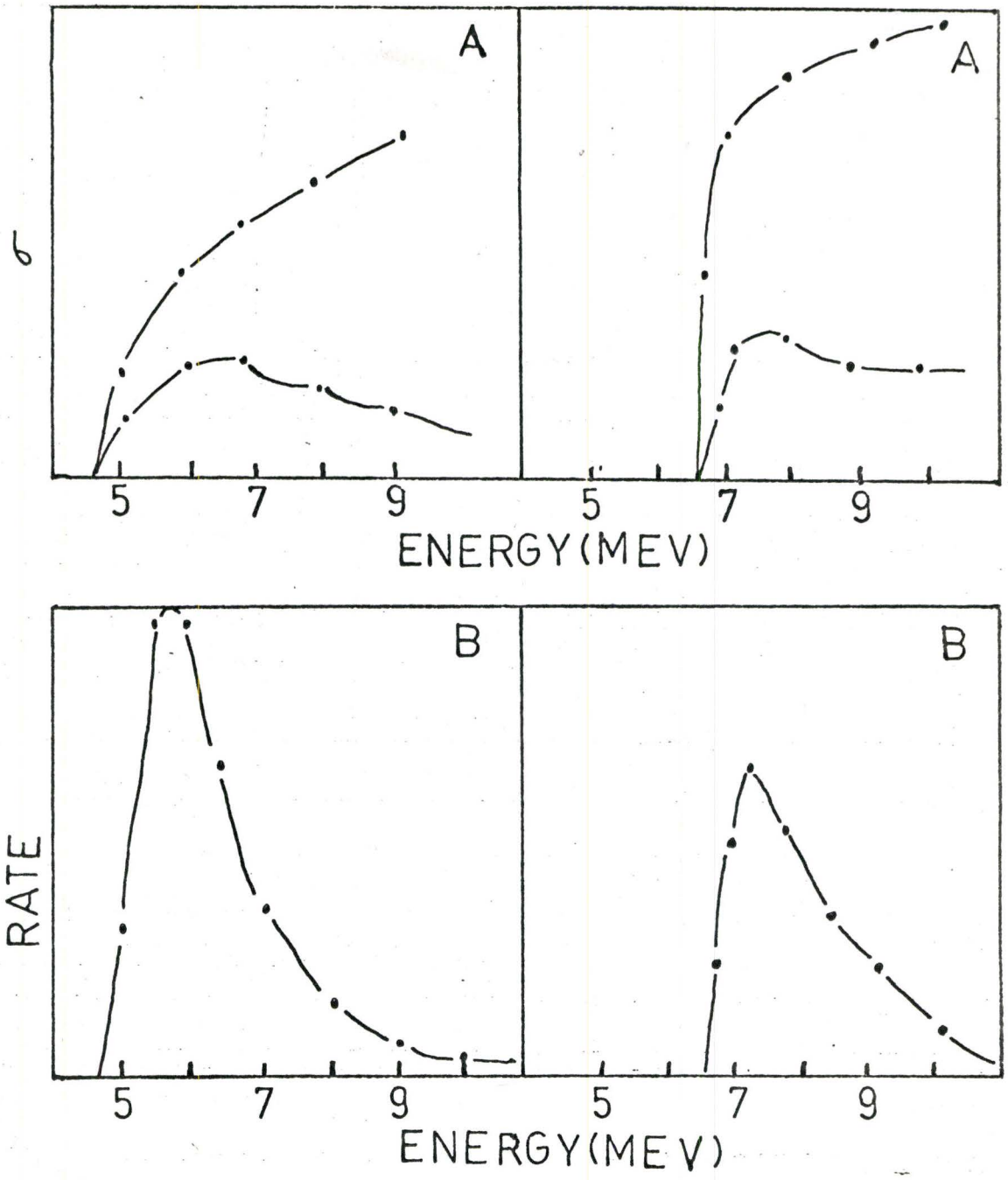

Figure 3-3 The calculated cross section (A) and rate (B) for typical higher energy levels in ^{28}Si. **In (A) the upper curve gives the result if the branching to other levels is ignored. The lower curve includes the effects of known levels.**

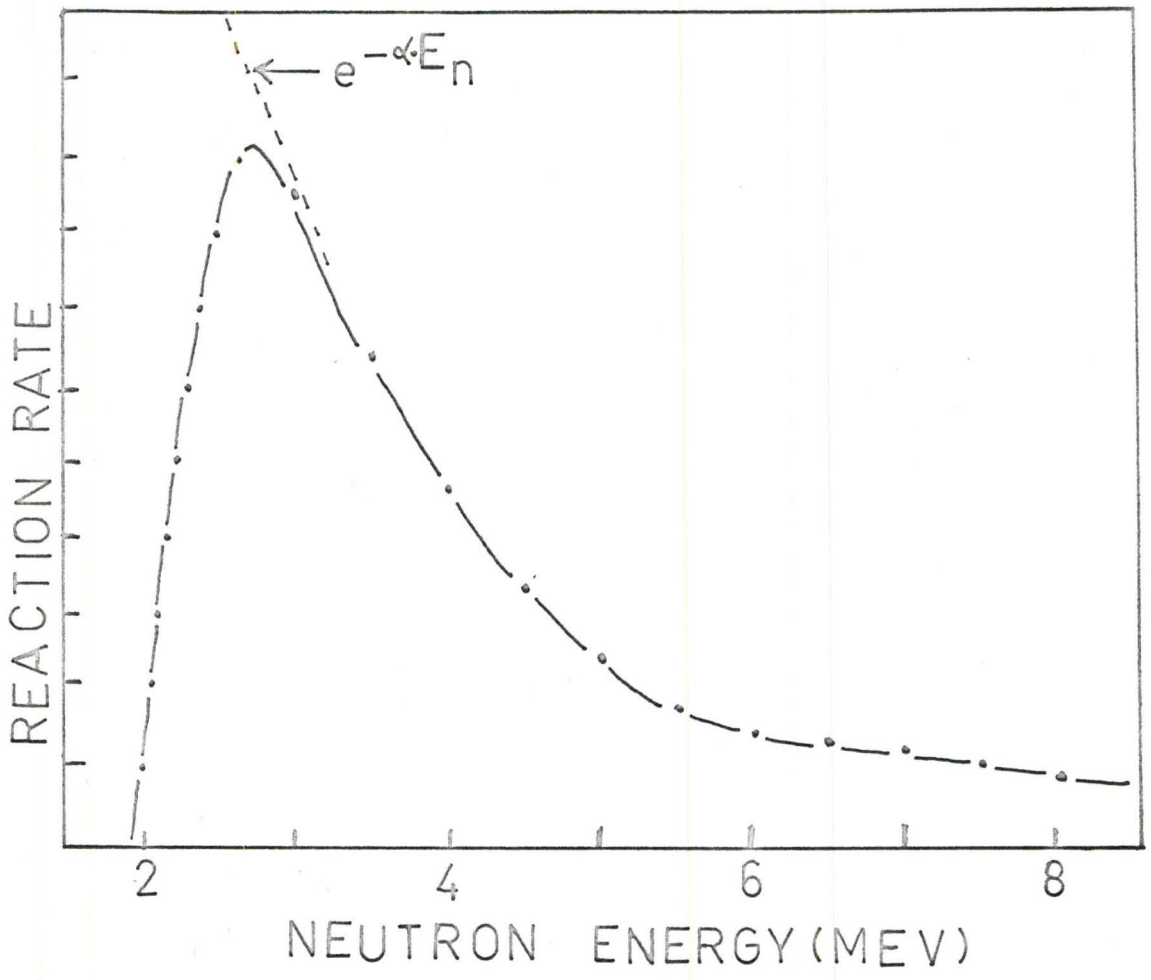

Figure 3-3C Reaction rates versus energy using Donahue's formula for σ and an exponential neutron flux.

If Donahue's formula for the cross section is used and if an exponential neutron flux distribution is used, then the population of a state is given by

$$\text{population} \sim (1 - \exp-\beta(E_n - E_{th})).\exp-\alpha E_n \quad ,$$

where E_n is the energy of the neutron and E_{th} is the level energy. Figure 3-3C is a plot of this equation for a state at 2 MeV. As can be seen in the figures 3-3A,B,C the population curves all have the same general shape and reach a peak value about 0.5 MeV above the threshold energy.

In order to test how sensitive the calculations were to an incorrect choice of spin and parity, various combinations of spins were tried for the levels. It was found that an incorrect choice of a spin for a high energy level had little effect on the calculated values for other levels. Any incorrect choices for levels below 3 MeV tended to have drastic effects on the results for other levels. In the nuclides studied in this work, the spins and parities for low lying levels were all well known. Thus it was possible to select reasonable spin choices for higher energy levels of unknown spin and use the predicted intensities obtained to iterate to find the correct spin of the levels. This proceedure was repeated until the best fit was obtained for all levels simultaneously.

3-3 Experimental Data Handling

The experimental data for each target studied

consisted of a set of single parameter measurements using the singles mode, pair mode and sometimes the Compton suppression mode of operation. The information obtained consisted of a set of energies and intensities of the gamma rays emitted by the target nuclei. In order to obtain the energy of a gamma ray, the channel position of the centroid of the response peak for the gamma ray had to be determined. The easiest technique to do this was by visual observation. It was generally possible under the experimental conditions to determine the centroid to the nearest two tenths of a channel which corresponds to 0.5 keV in energy. For some of the spectra a Gaussian peak with a linear background was fitted to the gamma ray peaks using a computer program. Since it gave the same results within the error quoted, it was felt that the simple visual approach was good enough. In addition the gamma ray lines may not have a Gaussian response, due to kinematic considerations arising from Doppler broadening. The energies of the gamma rays were obtained from the expression

$$E = a + b.x + c.x^2 ,$$

where x is the channel. The constants a, b, c were determined using a least squares fit to known gamma ray lines. For most spectra, known lines could be obtained from gamma rays originating from the (n,γ) reaction which always occured as background along with the $(n,n'\gamma)$ reaction. If low energy gamma rays were required then an external ^{56}Co source

was used as well. The accuracy of the energy measurements was limited by uncertainties in predicting the energy shift which occured as a result of dealing with fast neutrons. The general overall energy uncertainty was of the order of 3 keV.

The intensities of the lines were obtained by visually fitting a linear background to the peaks and then finding the area of the peaks. These results were also compared to a Gaussian peak fitting program and were found to give reasonable agreement. Since practically all the measured peaks had more than 1000 counts in them and since the background on the pair mode was low, the statistical uncertainty was generally under 5% for all peaks. The intensities were corrected for the response of the detection system using the efficiency curves given in section 2-7. The pair efficiency curve appeared to have uncertainties of under 5% judging from the consistency of the results. Marion et al[49] reported the error in the intensity of the nitrogen lines used for calibration to be under 15%. The photo-efficiency curve was not as accurate due to the poorer signal to noise ratio in the singles mode of operation. The overall error associated with the intensity measurements was generally less than 15%.

3-4 ^{28}Si Results

The silicon target consisted of a cylindrical piece of high purity natural silicon 4 inches in length and

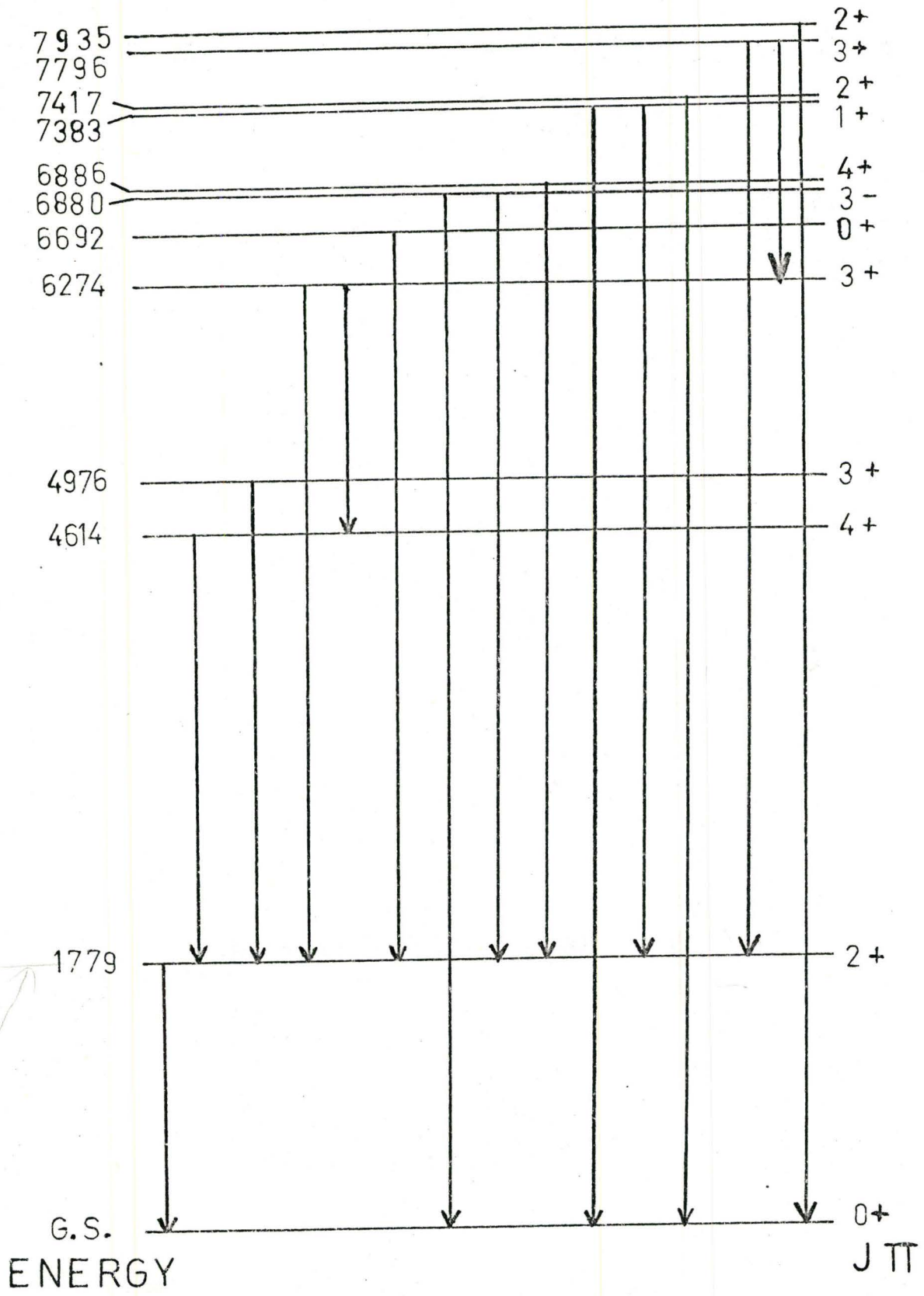

Fig. 3-4 ^{28}Si Decay Scheme

1 inch in diameter. Despite the fact that the boron carbide filter as well as the cadmium filter was used, there was a sufficient (n,γ) contribution in the silicon spectrum to use it to calibrate the energy scale. Since natural silicon consists of 92.2% ^{28}Si, 4.7% ^{29}Si and 3.1% ^{30}Si, gamma rays due to inelastic scattering reactions on all three isotopes occured. In the case of ^{29}Si the lines due to inelastic neutron scattering were masked by gamma rays produced by neutron capture on ^{28}Si. Table 3-2 lists the gamma ray energies and intensities for lines originating from the inelastic reaction on ^{28}Si. Table 3-3 gives the branching ratios. Table 3-4 compares the relative experimental population values for each level with the calculated values using the Hauser Feshbach formalism using previously measured spin and parity results. The fifth column indicates the percentage difference between the present measurement and the calculated results based on previous work. The two sets of population values were normalized to be equal for the 1778 keV level since this level had the least experimental uncertainty and its spin and parity are well known. For other elements studied in this work, normaliztion was usually done for a state in the 2-3 MeV region. Lower energy states were not chosen since the neutron flux would not fit the simple exponential distribution used for the calculations. High energy states were not used since they were generally weakly populated.

Column six of table 3-4 indicates each spin and parity which gives a calculated value within 30% of the experimental values. Spin states up to 6 were considered in the calculations. The neutron transmission coefficients used in the calculations were those of Bjorklund and Fernbach[16]. It was found that the coefficients given by Perey and Buck in the same reference gave similar results within experimental errors.

Table 3-2

Gamma Rays Produced by the $^{28}Si(n,n'\gamma)^{28}Si$ Reaction

Energy (keV)	Relative Intensity	Energy (keV)	Relative Intensity
1523.0	0.00075	5107.1	0.0122
1661.0	0.0118	5605.3	0.00246
1778.9	3.152	6019.1	0.00215
2835.3	0.0740	6880.0	0.00315
3197.4	0.0349	7383.6	0.00164
4494.3	0.00780	7416.5	0.00587
4913.2	0.00490	7934.8	0.00391
5101.1	0.00135		

Table 3-3

Branching Ratios for ^{28}Si Levels

Initial State (keV)	Final State (keV)	Present Work %	Previous Work Endt and Van der Leun[50]	Gibson et al[51]	Ernst[52]
1778.9	g.s.	100	100	100	100
4614.2	1779	100	100	100	100
4976.3	1779	100	100	100	100

Initial State	Final State	Present Work %	Endt and Van der Leun	Gibson et al	Ernst
6274.2	1779	60	90	85	55
	4614	40	10	15	45
6692.1	1779	100	100	100	100
6880	g.s.	*	67	69	60
	1779	*	33	28	40
	4614	-	(2)	3	-
6886	g.s.	*	1	-	80
	1779	*	100	100	20
7383.4	g.s.	40	45	45	57
	1779	60	55	55	43
7416.5	g.s.	100	90	92	100
		-	10	8	-
7795.8	1779	74	75	79	70
	6274	26	25	21	30
7934.8	g.s.	100	80	100	100
	1779	-	20	25	-

* In performing the Hauser Feshbach calculations the results of Gibson were used for the branching ratios which have been omitted due to experimental limitations in resolving doublets in the gamma ray spectrum.

Table 3-4

Experimental Population Values and Hauser Feshbach Results for ^{28}Si

Level Energy (keV)	Previous $J\pi$	Predicted Population	Experimental Population	% Difference	Possibl $J\pi$ value
1778.9	2+	3.067	3.067	-	1+,2+
4614.2	4+	0.0677	0.0616	+10	4+,4-
4976.3	3+	0.0349	0.0377	-7	0+,4+,4-

Level Energy	Previous $J\pi$	Predicted Population	Exp'l Population	% Difference	Possible $J\pi$ values
6274.2	3+	0.0213	0.0196	+9	(1+,1-),3+,3-
6692.1	0+	0.00513	0.00390	+31	0+,0-,4-
6880	3-	0.0112	0.0122	-8	1-,2+,2-,(3-)
6886	4+	0.0053	0.0045	+18	4+,4-
7383.4	1+	0.0045	0.0041	+7	1+,1-
7416.5	2+	0.0060	0.0059	+22	1-,2+,2-,(3+)
7795.8	3+	0.0034	0.0029	+16	1+,1-,3+,3-
7934.8	2+	0.0031	0.0039	-20	1-,2+,2-,(3+,3-)

The predicted possible J values which are in brackets are considered unlikely since the values of the spin and parity are more than two units of angular momentum different from the spin of a level to which the state decays to strongly. There appears to be no disagreement between previous results and the present results. No calculations were attempted for the two less abundant isotopes of silicon since only a few levels were observed and there would be severe interference from the (n,γ) reaction which produces the same energy gamma rays.

3-5 Non-zero Ground State Spin Cases

The silicon calculation contain fewer terms then most other targets since silicon has a 0+ ground state. This means that combining an incident neutron spin with the ground state spin can only lead to one intermediate spin state, and hence a limited number of terms in the calculations. Table 3-5 indicates the terms obtained for

^{27}Al which has a 5/2+ ground state. Only the formation of the intermediate state is indicated in the table. Figure 3-5 indicates the results of the calculations of the cross section as a function of energy of the 845 keV level in aluminum. The upper curve indicates the result with no branching from the intermediate level to other levels and the lower curve includes the effects of all known levels. The 1017 keV level causes the peak in the cross section of the 845 keV level to drop off more rapidly than in the upper case.

Table 3-5

Formation of Intermediate State Spins in Aluminum

ℓ	$\ell + s$	$J\pi$	ℓ	$\ell + s$	$J\pi$	ℓ	$\ell + s$	$J\pi$
0	1/2	2+	2	5/2	2+	4	7/2	1+
		3+			3+			2+
1	1/2	2-			4+			3+
		3-			5+			4+
			3	5/2	0-			5+
1	3/2	1-			1-			6+
		2-			2-	4	9/2	2+
		3-			3-			3+
		4-			4-			4+
					5-			5+
2	3/2	1+						6+
		2+	3	7/2	1-			7+
		3+			2-			
		4+			3-			
					4-			
2	5/2	0+			5-			
		1+			6-			

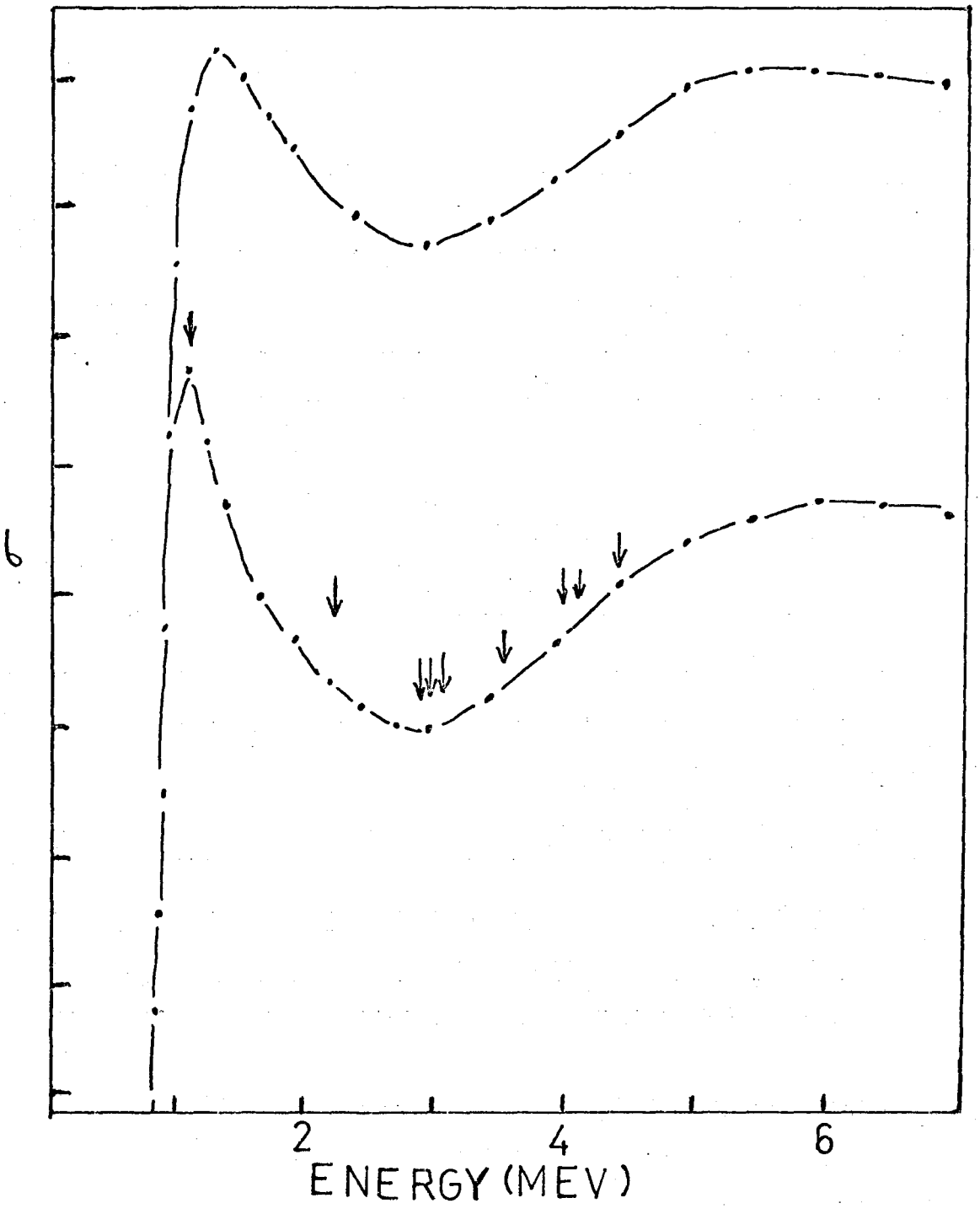

Figure 3-5 Calculated Cross Section Versus Energy for the 845 keV Level in Aluminum. The upper curve gives the result if the effects of other levels is ignored. The lower curve includes the effects of levels whose spin and parity is known. The arrows indicate the location in energy of these levels. The level at 1014 keV in particular has a great influence on the results.

CHAPTER 4

RESULTS OF CROSS SECTION MEASUREMENTS

The method developed by Ernst described in section 1-4 using Donahue's general cross section formula and an exponential neutron flux was considered as a possible way of explaining the experimental population values. It was found that the large range in population values could not be explained using this technique.

Calculations using the Hauser Feshbach formalism were performed for each isotope using the Bjorklund and Fernbach[16] neutron transmission coefficients. For some cases the calculations were also performed using Perey and Buck's[16] and Beyster's[11] neutron transmission coefficients. Since the results were the same within experimental error, only the results for the B&F coefficients are given. In this chapter, calculated population values based on previously known spins and parities have been compared with the experimental values and predictions have been made for the spin and parity of the various levels whose spin and parity are unknown. The methods used for the calculations have been described in detail in chapter 3 and will not be discussed further in this chapter. Unless stated otherwise it may be assumed that both the cadmium and boron neutron filters were used for each element given in this chapter. All energies have been corrected for the shift due to Doppler effects.

4-1 Calcium Results

Calcium was chosen as a target because its branching ratios, spins and parities are fairly well known. Thus calcium along with silicon provided a test for the mathematical model used in this work. A summary of the relevant information concerning calcium up to 1965 was given in a review article by Endt and Van der Leun[53]. MacDonald[54] et al in 1967 studied the $^{40}Ca(p,p'\gamma)^{40}Ca$ reaction. They measured the branching ratios and lifetimes of several levels and obtained some information regarding spins and parities.

Calcium was studied in this work using a calcium fluoride target encapsulated in aluminum. Natural calcium consists of 96.97% ^{40}Ca making it virtually a monoisotopic element. The fluorine component of the gamma ray spectrum was easily separated since fluorine was studied using a number of different compounds. The energy calibration of the spectrum was achieved using gamma rays produced by the $^{40}Ca(n,\gamma)^{41}Ca$ reaction and by background lines due to the presence of aluminum. No gamma rays originating from the $^{19}F(n,\gamma)^{20}F$ reaction were observed. The lower energy region was also calibrated using an external ^{56}Co source[55].

Both ^{28}Si and ^{40}Ca are magic nuclei and as a result both have their first excited states at high energy. The ground state of calcium is a 0+ state and the first excited

state occurs at 3350 keV. Since it also is a 0+ state, gamma ray transitions to the ground state are forbidden and decay is by internal conversion. Normalization of the calculated values to the experimental results was achieved using the 3730 keV level. This level is strongly populated and decays 100% to the ground state.

Table 4-1A is a list of the gamma ray transitions associated with the inelastic scattering on calcium. Table 4-1B gives the branching ratios obtained for the various levels. Table 4-1C gives the experimental population values for the levels of ^{40}Ca and compares them with the calculated results which are based upon previously measured spins and parities. Figure 4-1 shows the proposed decay scheme for ^{40}Ca.

Table 4-1A

Gamma Rays Produced by the $^{40}Ca(n,n'\gamma)^{40}Ca$ Reaction

Energy (keV)	Relative Intensity	Energy	Relative Intensity
755.1	0.0660	2124.0	0.0273
780.0	0.0034	2276.5	0.0020
1123.4	0.00972	2290.0	0.0248
1307.6	0.0441	2294.0	0.0034
1344.5	0.0169	2379.3	0.00801
1372.3	0.0338	3735.4	0.538
1794.0	0.0234	3904.8	0.549
1880.5	0.0235	5249.4	0.0681
2120.0	0.0062	5627.5	0.0162
		5901.4	0.0453

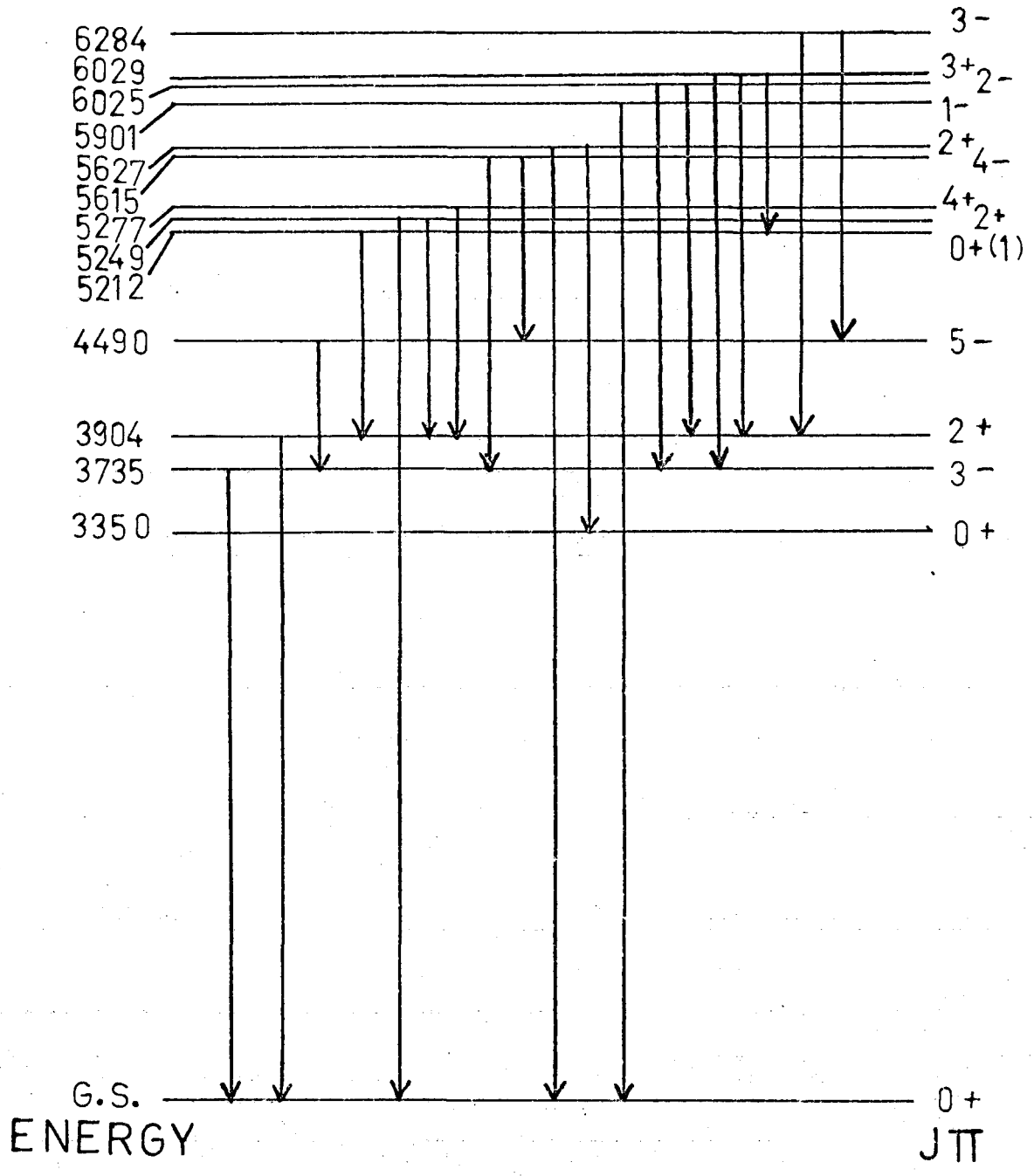

Fig. 4-1 ^{40}Ca Decay Scheme

Table 4-1B

Branching Ratios for ^{40}Ca Levels

Energy of Initial Level		Final Level (keV)	Branching Ratio (%)		
Present Work	Poletti et al (56)		Present Work	Poletti	MacDonald
3735.4	3736.8	g.s.	100	-	100
3904.8	3904.2	g.s.	100	-	100
		3350	-	-	2
4490.5	4491.7	3735	100	-	100
5212.4	5212.2	3905	100	-	100
5249.3	5248.8	g.s.	80	83	80
		3350	-	-	2.5
		3735	-	-	2.0
		3905	20	17	20
5277.1	5277.6	g.s.	-	-	8
		3905	100	-	96
		4491	-	-	4
5614.9	5614.5	3735	70	72	65
		4491	30	28	35
5627.4	5626.3	g.s.	91	-	90
		3350	9	-	10
5901.4	5900.1	g.s.	100	-	100
6025	6025.2	3735	80	80	-
		3905	20	20	-
6029	6029.0	3735	10	20	-
		3905	80	84	-
		5249	10	13	-
6284.1	6285.0	3905	25	24	25
		4491	75	76	75

Table 4-1C

Experimental Population Values and Calculated Values for ^{40}Ca

Level Energy (keV)	Previous Jπ	Predicted Population	Experimental Population	% difference	Possible Jπ Values
3350	0+	decays by internal conversion			--
3735.4	3-	0.461	0.461	-	1+1-2+2-3+3-
3904.8	2+	0.418	0.461	-9	1+,1-,2+,2-
4490.5	5-	0.264	0.320	-17	5+,5-
5212.4	0+(1)	0.0489(0+)	0.0442	+11	0+,0-
5249.3	2+	0.104	0.0808	+28	1+1-2+2-3+3-
5277.1	4+	0.0335	0.0345	-3	4+,4-
5614.9	4-	0.0222	0.0279	-20	0+,0-,4+,4-
5627.4	2+	0.0452	0.0391	+16	1+,1-,2+,2-
5901.4	1-	0.0421	0.0453	-7	1+,1-,2+,2-
6025	2-	0.0301	0.0310	-3	1+,1-,2+,2-
6029	3+	0.0350	0.0341	+3	2+,2-,3+,3-
6284.1	3-	0.0311	0.0350	-11	2+,2-,3+,3-

The calculated population values are in good agreement with the experimental values. All results agree within 30% error and 10 out of 11 are within 20%. As was the case for silicon the results are not sensitive to parity. The 5212 keV level appears to be a 0+ level and not a 1+ or 1- level. MacDonald *et al*[54] observed that the level previously reported at 6025 keV was a doublet. The present experimental limitations did not permit the resolution of

this doublet. The branching ratio given by MacDonald was used to divide up the total intensity of the decay of the two levels. If a doublet level was not assumed then the calculated values for any choice of spin and parity was too high by a factor of two. In addition a gamma ray of energy 780 keV was observed which was assumed to decay from the 6029 keV level to the 5249 keV level. The decay from the 6029 keV level to the 5277 keV level may not have been observed due to the low signal to background ratio of the facility at this energy.

4-2 Phosphorus Results

Phosphorus was studied because the spins and parities of levels up to 4431 keV are known and there are a number of levels above this with unknown spins. The ground state spin of phosphorus is 1/2+. Endt and Van der Leun[57] have summarized the results of previous ^{31}P work up to 1965. In 1968, Ernst[58] studied the $^{31}P(n,n'\gamma)^{31}P$ reaction. Also in 1968, Antropov[59] et al studied the $^{31}P(p,p'\gamma)^{31}P$ reaction using 6 MeV protons. Antropov et al performed Hauser Feshbach calculations for levels in the 3 to 4 MeV region and found spins in agreement with the results given by Endt and Van der Leun.

The phosphorus target consisted of a boron phosphide sample packed in an aluminum container. The boron component of the spectrum was separated from the spectrum by doing

a separate experiment using boron metal powder by itself. Natural phosphorus consists of 100% ^{31}P. The energy calibration was accomplished using gamma rays from the $^{31}P(n,\gamma)^{32}P$ reaction[60] as well as using known background lines.

Table 4-2A lists the gamma rays obtained from the inelastic neutron reaction. Table 4-2B gives the branching ratios measured. Table 4-2C gives the experimental population values and compares then with the calculated values based on prior measurements. Table 4-2C also gives predicted values for spins and parities for levels with no previous measurements. Figure 4-2 gives the proposed decay scheme for phosphorus. The Hauser Feshbach calculations are normalized for the 2234 keV level. It was felt that the experimental population of this level was the most reliable to use. The 1266 keV level has a large correction due to population of this level from the decay of higher energy levels. In addition the neutron flux does not follow the simple exponential model at this low energy. The predicted values for the spins in table 4-2C which are in brackets are considered unlikely since the values of spin and parity are more than two units of angular momentum different from the spin of a level to which the state decays to strongly.

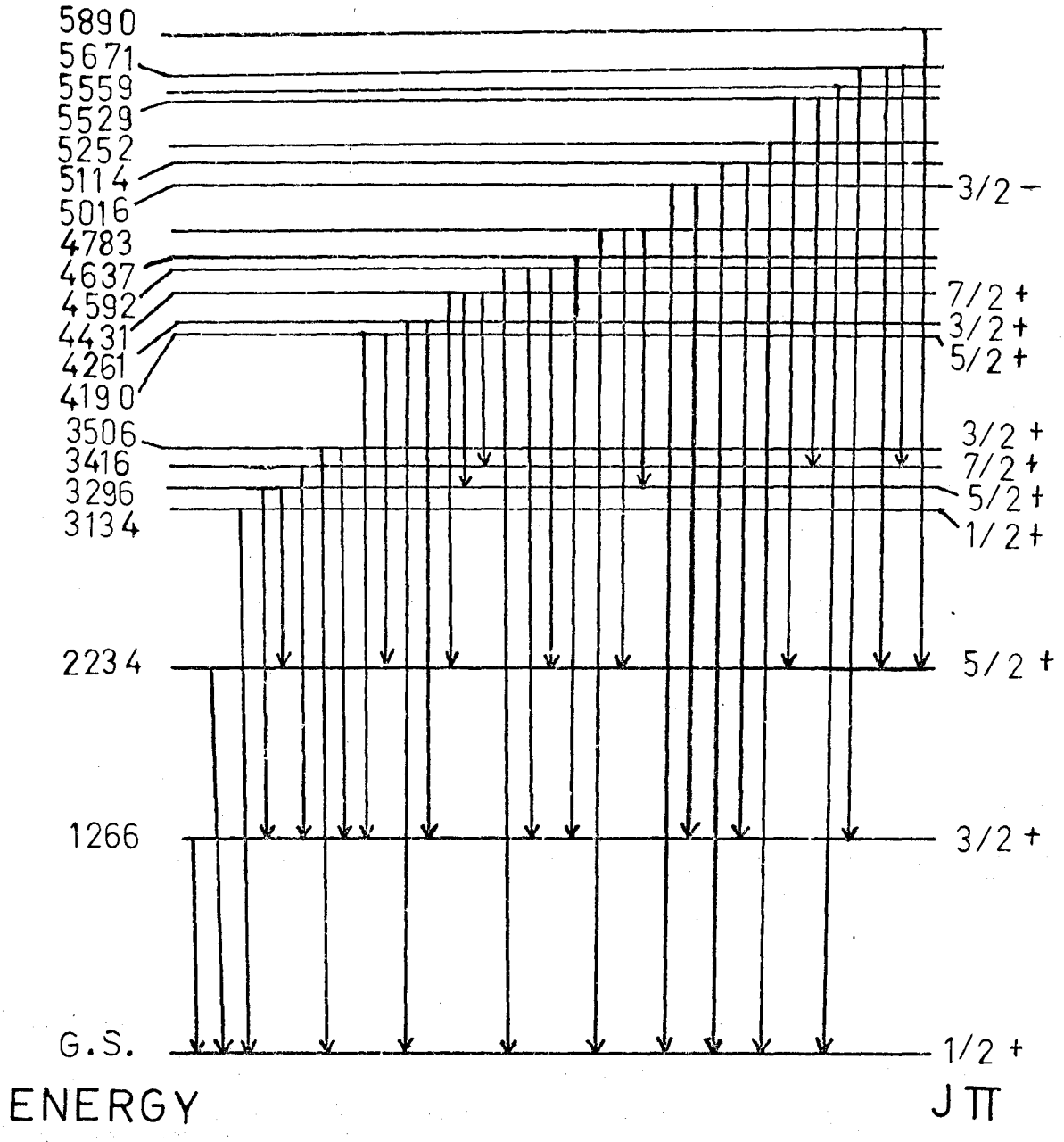

Fig. 4-2 ^{31}P Decay Scheme

Table 4-2A

Gamma Rays Produced by the $^{31}P(n,n'\gamma)^{31}P$ Reaction

Energy (keV)	Relative Intensity	Energy (keV)	Relative Intensity
1016.0	0.00650	2994.4	0.0900
1061.7	0.101	3134.7	0.534
1133.8	0.052	3295.0	0.0220
1266.4	9.73	3325.8	0.102
1486.4	0.0632	3370.4	0.229
1954.8	0.0500	3437.8	0.007
2029.7	0.829	3505.6	0.312
2111.4	0.0228	3655.6	0.0400
2150.0	0.541	3749.1	0.0631
2196.8	0.0690	3847.4	0.0911
2233.8	2.612	4261.4	0.272
2239.6	0.200	4405.0	0.0750
2253.8	0.007	4593.0	0.0464
2358.1	0.0368	4782.9	0.0813
2548.4	0.0360	5016.7	0.120
2880.5	0.0390	5251.8	0.0750
2924.2	0.182	5558.7	0.0900

Table 4-2B

Branching Ratios for ^{31}P Levels

Energy Initial Level (keV)		Final Level	Branching Ratio (%)		
Present Work	Endt and Van der Leun		Present Work	Endt and Van der Leun	Ernst
1266.4	1266.6	g.s.	100	100	100
2234.8	2233.8	g.s.	100	100	93
		1266	-	1	7
3134.1	3134.7	g.s.	100	100	100
3296.2	3294.9	1266	90	80	100
		2235	10	20	-
3416.4	3414.2	1266	100	100	100
3505.8	3505.5	g.s.	60	60	60
		1266	40	35+	35
		2235	-	5-	5
4190.4	4190.3	1266	80	75	100
		2235	20	25	-
4261.4	4260.4	g.s.	75	75	27
		1266	25	20	53
		2235	-	5	20
4430.8	4431.0	2235	53	55	50
		3296	42	40	45
		3415	5	5	5
4592.2	4592.4	g.s.	25	25	23
		1266	55	55	59
		2235	20	20	20
4636.8	4635.4	1266	100	100	100
4782.9	4782.3	g.s.	45	40	-
		1266	-	5	-
		2235	20	20	-
		3296	35	35	-
5016.3	5015.4	g.s.	65	70	61
		1266	35	30	39

Energy Initial Level			Branching Ratios (%)		
Present Work	Endt and Van der Leun	Final Level	Present Work	Endt and Van der Leun	Ernst
5114.3	5116	1266	70	65	-
		2235	30	35	-
5251.8	5254	g.s.	100	100	-
5528.8	5530	2235	50	40	-
		3416	50	40	-
5558.7	5557	g.s.	100	100	-
5671.4	5673	1266	80	55	-
		2235	10	10	-
		3416	10	10	-
5890.4	5892	2235	100	100	-

Table 4-2C

Experimental Population Values and Calculated Values for ^{31}P

Level Energy (keV)	Previous $J\pi$	Calculated Population	Experimental Population	% Difference	Possible $J\pi$ Values
1266.4	3/2+	7.858	7.561	+4	$\frac{1}{2}+\frac{3}{2}+\frac{3}{2}-\frac{5}{2}+\frac{5}{2}-$
2234.8	5/2+	2.328	2.328	-	$\frac{3}{2}+,\frac{3}{2}-,\frac{5}{2}+,\frac{5}{2}-$
3134.1	1/2+	0.586	0.532	+10	$\frac{1}{2}+,\frac{1}{2}-,\frac{7}{2}+,\frac{7}{2}-$
3296.2	5/2+	0.785	0.814	-5	$\frac{1}{2}+\frac{3}{2}+\frac{3}{2}-\frac{5}{2}+\frac{5}{2}-$
3416.4	7/2+	0.439	0.528	-17	$\frac{1}{2}+\frac{1}{2}-\frac{5}{2}+\frac{5}{2}-\frac{7}{2}+\frac{7}{2}-$
3505.8	3/2+	0.559	0.511	+9	$\frac{1}{2}+\frac{3}{2}+\frac{3}{2}-\frac{5}{2}+\frac{5}{2}-$
4190.4	5/2+	0.312	0.236	+32	$\frac{1}{2}+\frac{1}{2}-\frac{5}{2}+\frac{7}{2}+\frac{7}{2}-$

Level Energy	Previous $J\pi$	Calculated Population	Experimental Population	% Difference	Possible $J\pi$ Values
4261.4	3/2+	0.321	0.360	-11	$\frac{3}{2}^+,\frac{3}{2}^-,\frac{5}{2}^+,\frac{5}{2}^-$
4430.8	7/2+	0.169	0.136	+24	$\frac{1}{2}^-,\frac{7}{2}^+,\frac{7}{2}^-$
4592.2			0.185		$\frac{1}{2}^+\frac{3}{2}^+\frac{3}{2}^-\frac{5}{2}^+\frac{5}{2}^-(\frac{7}{2}^+)$
4636.8			0.234		$\frac{3}{2}^+,\frac{3}{2}^-,\frac{5}{2}^+,\frac{5}{2}^-$
4782.9			0.181		$\frac{3}{2}^+,\frac{3}{2}^-,\frac{5}{2}^+,\frac{5}{2}^-$
5016.3	3/2-	0.149	0.189	-21	$\frac{3}{2}^+,\frac{3}{2}^-,\frac{5}{2}^+,\frac{5}{2}^-$
5114.3			0.133		$\frac{3}{2}^+,\frac{3}{2}^-,\frac{5}{2}^+,\frac{5}{2}^-$
5251.8			0.0752		$\frac{1}{2}^+,\frac{1}{2}^-,(\frac{7}{2}^+,\frac{7}{2}^-)$
5528.8			0.0451		$(\frac{1}{2}^+),\frac{7}{2}^+,\frac{7}{2}^-$
5558.7			0.0900		$\frac{3}{2}^+,\frac{3}{2}^-,\frac{5}{2}^+,\frac{5}{2}^-$
5671.4			0.0905		$\frac{3}{2}^+,\frac{3}{2}^-,\frac{5}{2}^+,\frac{5}{2}^-$
5890.4			0.0401		$\frac{1}{2}^+,\frac{1}{2}^-,\frac{7}{2}^+,\frac{7}{2}^-$

There were a number of doublets in the phosphorus spectrum which somewhat limited the interpretation of the results. Previous workers have observed a gamma ray at 2025 keV which forms a 5% component to the decay of the 4260 keV level. A gamma ray of energy 2029 keV which forms 90%

of the decay of the 3295 keV level was observed. The 3295 keV level was populated more than twice as much as the 4260 keV level. There was no evidence for a gamma ray at 2025 keV in this work although its detection would have been difficult due to the facts indicated above. If a gamma ray at 2025 keV existed it would have introduced a small error in the population of the 3295 and 4260 keV levels.

The results for the levels at 2234 and 3506 keV were coupled through the 2234-2240 keV gamma ray doublet. In this case there was some evidence of a doublet due to the unusually wide peak. The estimated branching ratio appeared to be in agreement with prior results. The 2234 keV gamma ray has an intensity more than ten times the intensity of the 2240 keV gamma ray so that the error in the 2234 keV gamma ray would be negligable. In spite of uncertainties introduced by the doublets in the spectrum, there does not appear to be any discrepancies between the present work and previous work.

4-3 Aluminum Results

The aluminum sample consisted of a pure metal bar of aluminum 4 inches long with a 1 cm square cross section. Aluminum was the first element studied in this work and as a result only the cadmium neutron filter was used. This meant that the gamma rays coming from the $^{27}Al(n,\gamma)^{28}Al$ reaction formed a prominent part of the resultant spectrum. These gamma rays provided a simple energy and efficiency calibration[61]

for the system. The efficiency calibration agreed well with a later one done using a melamine target. Endt and Van der Leun[62] have summarized the results for aluminum up to 1965. Ernst[63] studied the neutron inelastic scattering reaction on aluminum and Antropov[59] studied the inelastic proton scattering reaction on aluminum in 1968. Since aluminum is monoisotopic in nature, all of the broadened lines are due to the $^{27}Al(n,n'\gamma)^{27}Al$ reaction.

There were several problems in obtaining the intensities of some of the gamma rays. The gamma ray at 171 keV was assumed to be present. It was not measured due to the fact that it would be a relatively weak intensity line in an area of the energy spectrum with a high background. In addition the neutron absorbers in the beam greatly reduced the detection efficiency of the system at this low energy. The intensity and energy of this line were assumed to be the values given in Endt and Van der Leun. The line due to inelastic neutron scattering at 1014 keV overlapped a strong thermal capture line at 1017 keV. The intensity of the 1017 keV line was known relative to other capture gamma ray lines and was subtracted to find the correct intensity of the 1014 keV line. Similarly a line at 1777 keV was found to overlap a line at 1778 keV which occurs as the de-excitation of the first state in silicon following decay from the ground state of ^{28}Al. The two lines at 2199 and 2212 keV

occurred in the area of the 2223 keV peak and its Compton continuum which occur as a background component in all the experiments. The 2212 keV line was very intense so that there was very little possible error involved in measuring its intensity. The 2199 keV line however was very weak and the error in measuring its intensity could be very large. The two lines at 3038 and 3045 keV were unresolved and as a result there was a large uncertainty in their relative intensity to one another. The structure of the doublet suggested that the lower peak was 50% larger than the upper peak. This was in agreement with the work of Ernst in which the two lines were better resolved.

Table 4-3A gives a list of the gamma rays produced by the $^{27}Al(n,n'\gamma)^{27}Al$ reaction. Table 4-3B lists the branching ratios. Table 4-3C gives the experimental population values for the levels and compares them with the calculated ones based on previous work. The table also gives values of spins and parities for several levels where no prior measurements have been made. The two sets of population values are normalized to give the best fit for the 2208 and 2732 keV levels together. The 1014 and 845 keV levels were not used for normalization due to their low energy. Figure 4-3A gives the proposed decay scheme for ^{27}Al.

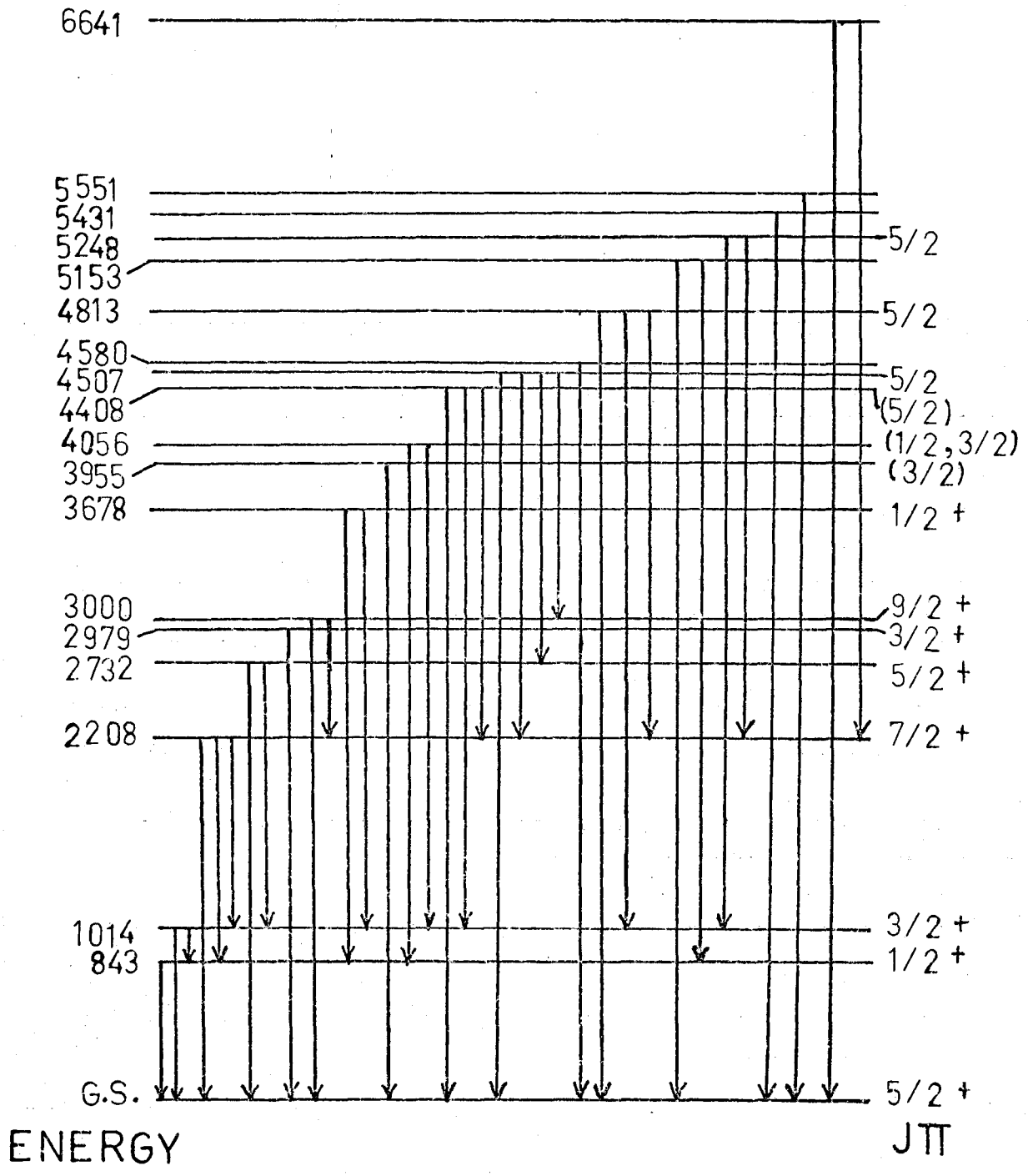

Fig. 4-3A ^{27}Al Decay Scheme

Table 4-3A

Gamma Rays Produced by the $^{27}Al(n,n'\gamma)^{27}Al$ Reaction

Energy (keV)	Relative Intensity	Energy (keV)	Relative Intensity
171	not measured	3038.2	0.170
791.5	0.590	3044.8	0.260
843.2	9.390	3213.7	0.512
1014.1	16.940	3393.8	0.188
1194.2	0.060	3798.2	0.128
1363.8	0.180	3955.1	0.589
1507.3	0.230	4233.9	0.184
1718.4	2.880	4311.4	0.131
1775.8	0.0921	4408.4	0.392
2199.1	0.120	4430.4	0.0721
2207.8	7.311	4506.0	0.052
2299.1	0.540	4580.5	0.298
2604.5	0.142	4813.1	0.194
2664.1	0.291	5152.6	0.0882
2731.7	0.964	5431.0	0.410
2834.7	0.249	5551.2	0.220
2979.1	1.712	6641.8	0.109
2999.9	2.683		

Table 4-3B

Branching Ratios for ^{27}Al Levels

Energy Initial Level (keV)		Final Level (keV)	Branching Ratio (%)		
Present Work	Endt and Van der Leun		Present Work	Endt and Van der Leun	Ernst
843.2	842.9	g.s.	100	100	100
1014.1	1013.0	g.s.	97(assumed)	97	97
		843	3	3	3
2207.8	2208.9	g.s.	96	100	94
		843	3	2	4
		1014	1	2	1.6
2732.3	2732.0	g.s.	25	24	21
		1014	75	76	79
2979.1	2979.7	g.s.	100	100	100
2999.8	3000.6	g.s.	82	87	74
		2208	18	13	26
3678.2	3677.8	843	46	65	49
		1014	54	35	51
3955.1	3955.9	g.s.	100	100	100
4055.9	4054.8	843	75	80	53
		1014	25	20	47
4408.2	4409	g.s.	55	55	53
		1014	25	25	27
		2208	20	20	20
4507.1	4508	g.s.	5	10	4
		2208	60	60	52
		2732	25	20	34
		3000	10	10	10
4580.4	4580	g.s.	100	100	100
4812.6	4811	g.s.	41	40	29
		1014	30	35	23
		2208	29	25	-
		4055	-	-	48

Energy Initial Level			Branching Ratios (%)		
Present Work	Endt and Van der Leun	Final Level	Present Work	Endt and Van der Leun	Ernst
5153.6	5155	g.s.	60	-	50
		843	40	-	50
5248.0	5246	1014	44	70	26
		2208	56	20	74
5431.0	5434	g.s.	100	100	-
5551.2	5550	g.s.	100	100	-
6640.7	6640	g.s.	60	-	-
		2208	40	-	-

Table 4-3C

Experimental Population Values and Calculated Values for ^{27}Al

Level Energy (keV)	Previous $J\pi$	Calculated Population	Experimental Population	% Difference	Possible $J\pi$ Values
843.2	1/2+	9.431	8.502	+11	$\frac{1}{2}^+, \frac{1}{2}^-$
1014.1	3/2+	14.712	13.504	+9	$\frac{3}{2}^+, \frac{9}{2}^-$
2207.8	7/2+	6.40	5.80	+10	$\frac{5}{2}^+, \frac{5}{2}^-, \frac{7}{2}^+, \frac{7}{2}^-$
2732.3	5/2+	3.40	3.76	-10	$\frac{5}{2}^+, \frac{7}{2}^+, \frac{7}{2}^-$
2979.1	3/2+	1.78	1.71	+4	$\frac{1}{2}^+, \frac{3}{2}^+, \frac{3}{2}^-, (\frac{9}{2}^-)$
2999.8	9/2+	2.42	3.02	-20	$\frac{5}{2}^+, \frac{7}{2}^+, \frac{7}{2}^-, \frac{9}{2}^+$
3678.2	1/2+	0.510	0.541	-6	$\frac{1}{2}^+, \frac{1}{2}^-, (\frac{11}{2}^-)$
3955.1	(3/2)	0.735	0.590	+25	$\frac{3}{2}^-, \frac{9}{2}^-, (\frac{11}{2}^+, \frac{11}{2}^-)$

Level Energy	Previous $J\pi$	Calculated Population	Experimental Population	% Difference	Possible $J\pi$
4055.9	$(\frac{1}{2},\frac{3}{2})$	0.730 (3/2) 0.482 (1/2)	0.680	+7	$\frac{3}{2}^+,\frac{3}{2}^-,(\frac{9}{2}^-)$
4408.2	(5/2)	0.806	0.690	+17	$\frac{3}{2}^+\frac{3}{2}^-\frac{5}{2}^+(\frac{9}{2}^-\frac{11}{2}^+)$
4507.1	5/2	0.678	0.910	-25	$\frac{5}{2}^+,\frac{7}{2}^+,\frac{7}{2}^-,\frac{9}{2}^+$
4580.4			0.303		$\frac{1}{2}^+\frac{1}{2}^-\frac{3}{2}^+\frac{3}{2}^-(\frac{11}{2}^+\frac{11}{2}^-)$
4812.6	5/2	0.562	0.462	+22	$\frac{3}{2}^+\frac{5}{2}^+\frac{5}{2}^-(\frac{7}{2}^+\frac{7}{2}^-\frac{9}{2}^+\frac{9}{2}^-)$
5153.6			0.220		$\frac{3}{2}^+\frac{3}{2}^-(\frac{9}{2}^-\frac{11}{2}^+\frac{11}{2}^-)$
5248.0	5/2	0.492	0.440	+12	$\frac{5}{2}^+,\frac{7}{2}^+,\frac{7}{2}^-,(\frac{9}{2}^+)$
5431.0			0.410		$\frac{5}{2}^+,\frac{7}{2}^+,\frac{7}{2}^-,\frac{9}{2}^+$
5551.2			0.221		$\frac{3}{2}^+\frac{3}{2}^-\frac{5}{2}^+\frac{5}{2}^-\frac{9}{2}^+\frac{9}{2}^-(\frac{11}{2}^+)$
6640.7			0.181		$\frac{5}{2}^+,\frac{5}{2}^-,\frac{7}{2}^+,\frac{7}{2}^-$

The present experimental results are in agreement with prior J values. The value of the spin of the 4056 keV level is 3/2. This value was used in calculating the spins for higher levels. Any predicted spin value more than two angular momentum units above the spin of a level to which there is a strong decay mode is listed in brackets as an unlikely value.

In addition to inelastic neutron scattering, evidence for three other less prominent fast neutron reactions was

observed. The $^{27}Al(n,\alpha\gamma)^{24}Na(\beta^-,\gamma)^{24}Mg$ series of reactions led to the 2754 and 1368 keV gamma rays being observed due to de-excitation of ^{24}Mg levels. There were also 867 and 472 keV gamma ray lines observed as a result of the decay of the 1341 keV level in ^{24}Na. Evidence for the $^{27}Al(n,p\gamma)^{27}Mg(\beta^-,\gamma)^{27}Al$ reactions was found. Gamma rays belonging to this set of reactions were found at 953, 984, 1692 and 1701 keV. Figure 4-3B gives the decay schemes showing the placement of these gamma rays. Since they led to the population of the 843 and 1014 keV levels of ^{27}Al, a small correction for the population of these levels was necessary.

As shown in figure 4-3C a gamma ray line 35 keV above the 7725 keV ground state transition in ^{28}Al was observed. This was interpreted as being a ground state transition from capture in the 35 keV resonance state of ^{28}Al. This effect was weakly observed by two previous investigators[64,65]. The aluminum target was studied at both the front and back edge of the reactor core in order to determine the energy shift due to the use of fast neutrons. The cadmium filter was not as effective at the front edge of the core since it was not designed to overlap as far on this side of the core. As a result the thermal capture gamma ray lines were enhanced by a factor of two over lines due to fast neutron reactions. The 7725 + 35 keV line was reduced in intensity compared to thermal capture lines indicating it is not the result of a

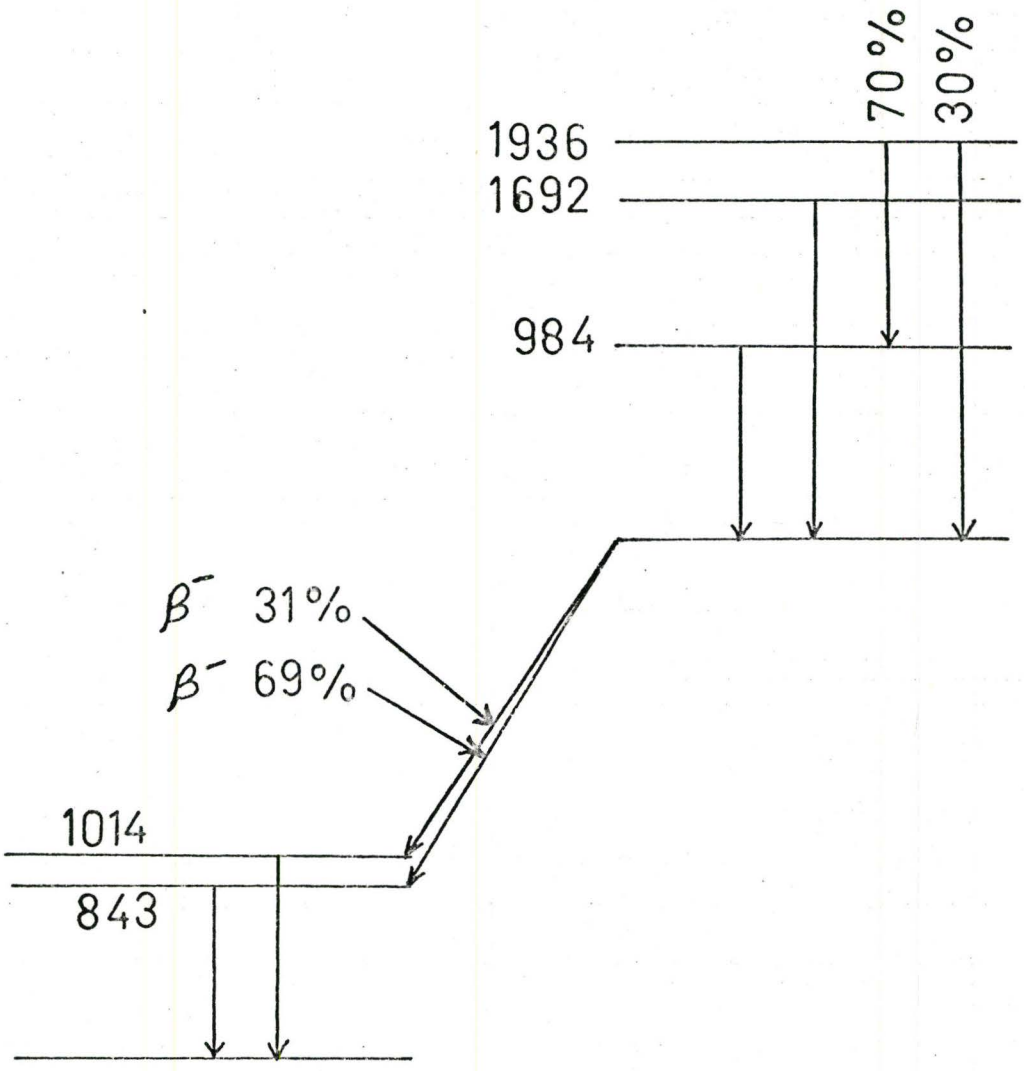

Figure 4-3B ^{27}Mg contribution to ^{27}Al spectrum. ^{27}Mg states can be populated by fast neutrons by the (n,p) reaction.

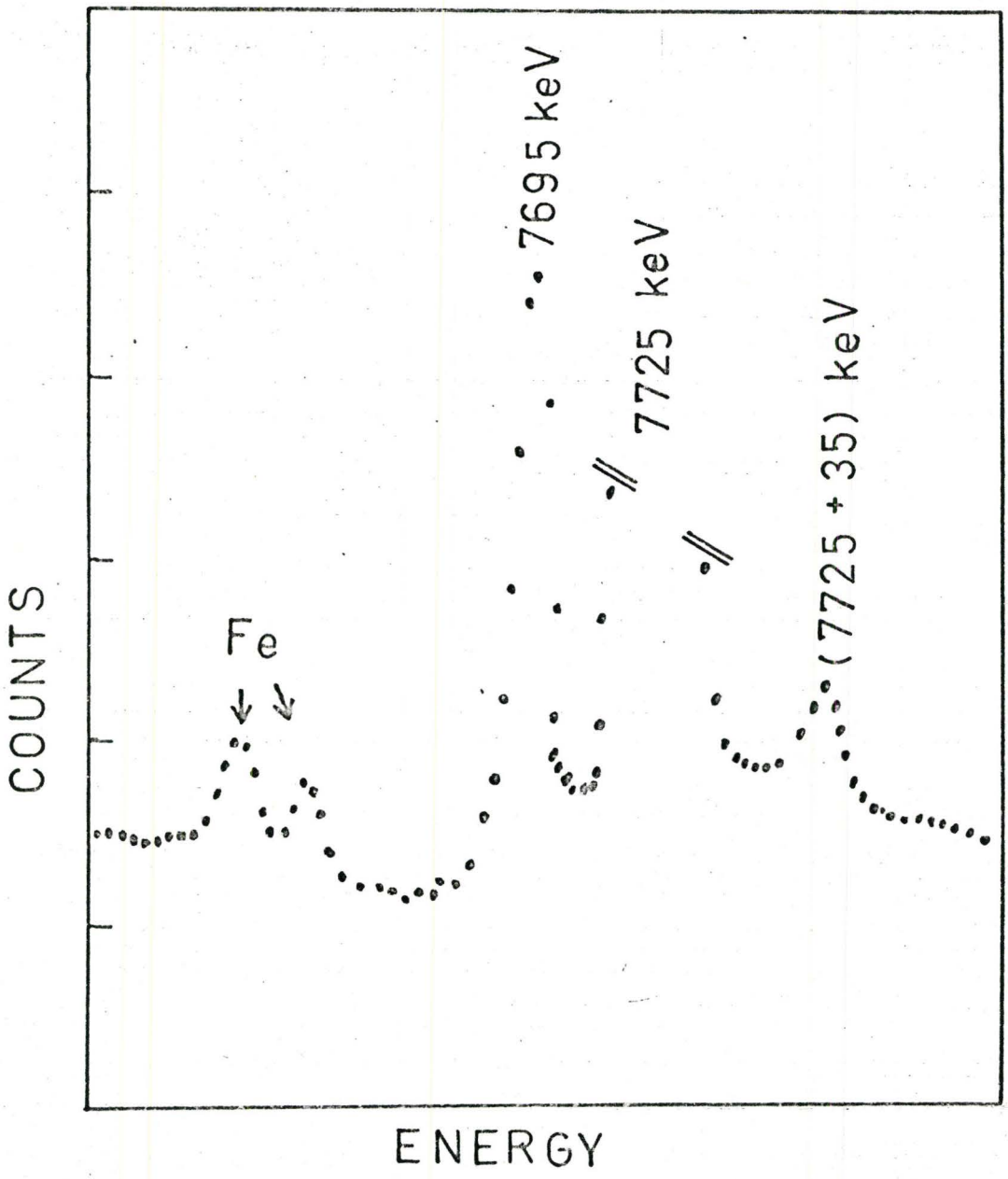

Figure 4-3C The 35 keV resonance state in ^{27}Al. The line at 7725 + 35 keV is evidence for the population of the 35 keV resonance in ^{27}Al. The iron doublet in the background gives an indication of the resolution obtained.

thermal neutron reaction. The width of the peak implied that it was produced by an interaction with a relatively low energy neutron since it showed no Doppler broadening. A check was made to see if other resonance capture effects could be observed with negative results. A ground state transition from capture in the 6 keV resonance would have been difficult to observe due to the intense 7725 keV transition.

4-4 Sodium Results

Sodium was studied using a sodium fluoride sample. As was the case with the other fluorides the fluorine component of the spectrum was easily identified. Sodium is monoisotopic in nature so that all lines produced by inelastic scattering of neutrons on sodium belong to ^{23}Na. The energy scale was calibrated using the $^{23}Na(n,\gamma)^{24}Na$ reaction[61] and also by known background lines. Prior results for ^{23}Na have been summarized by Endt and Van der Leun[66].

Table 4-4A lists the gamma rays due to inelastic neutron scattering on ^{23}Na. Table 4-4B gives the branching ratios. Table 4-4C gives the experimental population values and compares them to calculated values and also gives predicted values of spins and parities for the various levels. Figure 4-4 gives a proposed decay scheme for ^{23}Na. Normalization of the calculated values to the experimental population values was done using the 2640 keV level. This level was chosen because it decays 100% to the ground state and has a small correction due to population from higher energy states.

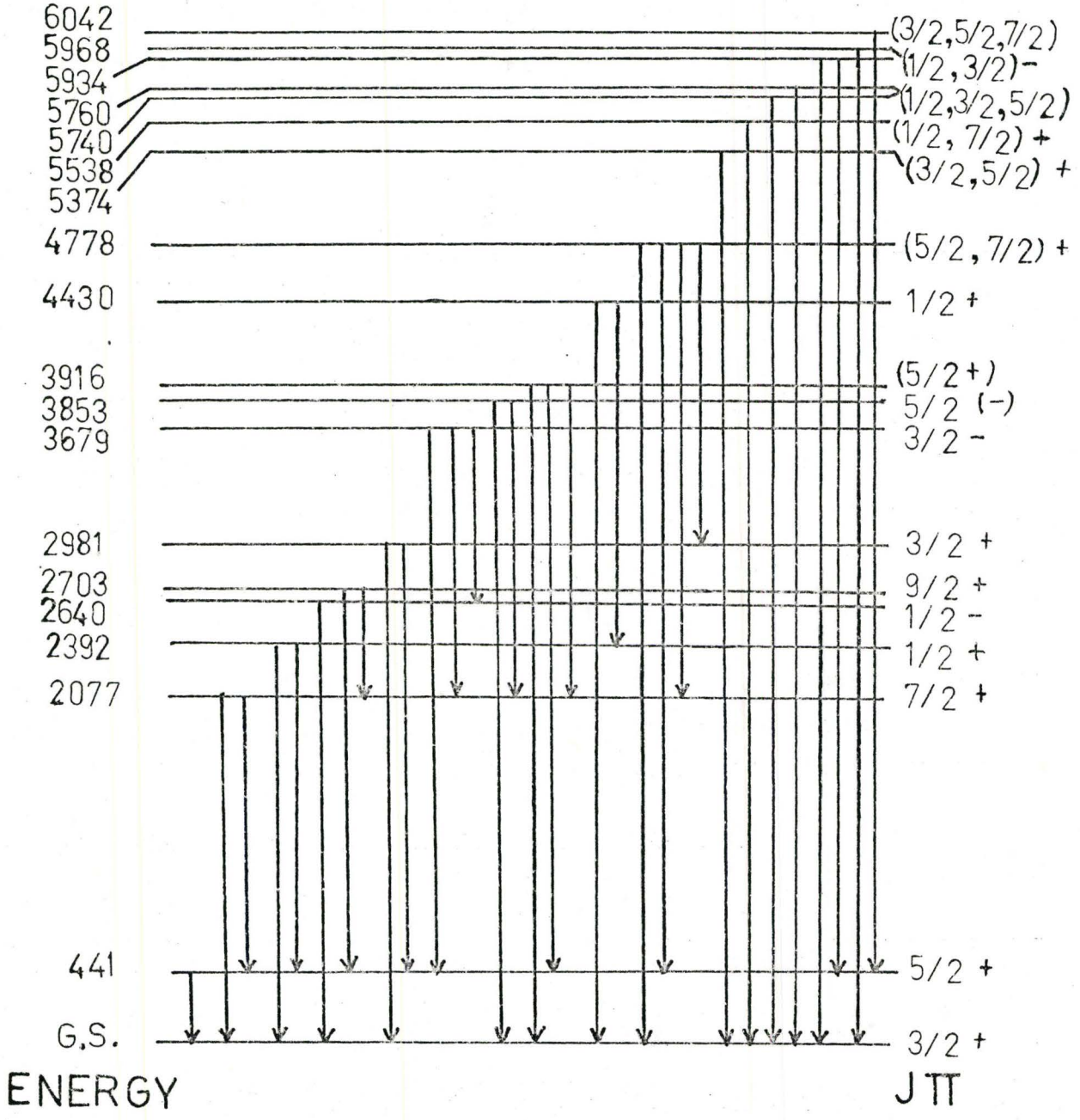

Fig. 4-4 ^{23}Na Decay Scheme

The 2077 keV level was unsuitable for normalization since it decayed by a 1635 keV (92%) transition which occurs at the low energy end of the pair response. The 2391 keV level was not as suitable for normalization since its decay is split between two gamma rays.

Table 4-4A

Gamma Rays Produced by the $^{23}Na(n,n'\gamma)^{23}Na$ Reaction

Energy (keV)	Relative Intensity	Energy (keV)	Relative Intensity
441.1	28.05	2981.5	0.960
624.5	0.521	3238.2	0.572
1038.8	0.0713	3474.3	0.148
1096	0	3679	0
1601.8	0.0714	3852.7	0.355
1636.3	4.511	3916.0	0.450
1777.3	0.355	4337.2	0.179
1797.5	0.0456	4430.3	0.281
1838.0	0.149	4777.9	0.0300
1951.4	0.770	5374.2	0.312
2038.4	0.0198	5493.0	0.004
2077.3	0.431	5538.0	0.111
2263.8	0.812	5600.4	0.0400
2390.5	1.300	5739.7	0.0712
2539.4	0.960	5760.1	0.199
2640.1	1.402	5934.2	0.0358
2701.2	0.0451	5967.8	0.0350

Table 4-4B

Branching Ratios for ^{23}Na Levels

Energy Initial Level (keV)		Final Level (keV)	Branching Ratio (%)	
Present Work	Endt and Van der Leun		Present Work	Endt and Van der Leun
441.1	440	g.s.	100	100
2077.4	2078	g.s.	8	10
		441	92	90
2391.5	2393	g.s.	63	65
		441	37	35
2640.1	2641	g.s.	100	100
2703.4	2705	441	61	60
		2077	39	40
2981.0	2983	g.s.	50	55
		441	50	45
3679.2	3678	g.s.	-	5
		441	80	70
		2077	10	10
		2640	10	15
3852.7	3850	g.s.	50	50
		2077	50	50
3915.8	3915	g.s.	60	70
		441	20	15
		2077	20	15
4430.3	4431	g.s.	92	95
		2392	8	5
4777.9	4775	g.s.	10	5
		441	60	60
		2077	15	20
		2981	15	10
		3679	-	5
5374.2	5378	g.s.	100	-
5538.0	5538	g.s.	100	-

Energy Initial Level		Final Level	Branching Ratio	
Present Work	Endt and Van der Leun		Present Work	Endt and Van der Leun
5739.7	5738	g.s.	100	-
5760.1	5762	g.s.	100	-
5934.2	5935	g.s. 441	90 10	- -
5967.8	5967	g.s.	100	-
6041.5	6042	441	100	-

Table 4-4C

Experimental Population Values and Calculated Values for ^{23}Na

Level Energy (keV)	Previous $J\pi$	Calculated Population	Experimental Population	% Difference	Possible $J\pi$ Values
441.1	5/2+	36.501	20.1	+82	-
2077.4	7/2+	4.508	3.81	+18	$\frac{3}{2}^-, \frac{7}{2}^+, \frac{7}{2}^-$
2391.5	1/2+	1.852	1.87	-11	$\frac{1}{2}^+, \frac{1}{2}^-, \frac{9}{2}^+, \frac{9}{2}^-$
2640.1	1/2-	1.334	1.334	0	$\frac{1}{2}^+, \frac{1}{2}^-, (\frac{9}{2}^+, \frac{9}{2}^-)$
2703.4	9/2+	1.211	1.33	-9	$(\frac{1}{2}^+, \frac{1}{2}^-), \frac{9}{2}^+, \frac{9}{2}^-$
2981.0	3/2+	1.86	1.87	$-\frac{1}{2}$	$\frac{3}{2}^+ \frac{3}{2}^- \frac{5}{2}^+ \frac{5}{2}^- \frac{7}{2}^+$
3679.2	3/2-	0.903	0.712	+27	$\frac{1}{2}^-, \frac{3}{2}^-$
3852.7	5/2(-)	0.908	0.715	+27	$\frac{1}{2}^+ \frac{3}{2}^+ \frac{3}{2}^- \frac{5}{2}^- \frac{7}{2}^+ \frac{7}{2}^-$
3915.8	(5/2+)	0.836	0.752	+11	$\frac{3}{2}^+ \frac{3}{2}^- \frac{5}{2}^+ \frac{5}{2}^- \frac{7}{2}^+ \frac{7}{2}^-$

Level Energy	Previous JΠ	Calculated Population	Experimental Population	% Difference	Possible JΠ
4430.3	1/2+	0.281	0.300	-6	$\frac{1}{2}^+,\frac{1}{2}^-,(\frac{9}{2}^+,\frac{9}{2}^-)$
4777.9	$(\frac{5}{2},\frac{7}{2})^+$	0.342	0.316	+14	$\frac{3}{2}^+,\frac{3}{2}^-,\frac{5}{2}^+,\frac{5}{2}^-,\frac{7}{2}^+,$
5374.2	$(\frac{3}{2},\frac{5}{2})^+$	0.235 $(\frac{5}{2}^+)$	0.316	-25	$\frac{5}{2}^+,\frac{5}{2}^-$
5538.0	$(\frac{1}{2},\frac{7}{2})^+$	0.092 $(\frac{1}{2}^+)$	0.111	-17	$\frac{1}{2}^+,\frac{1}{2}^-,(\frac{9}{2}^+,\frac{9}{2}^-)$
5739.7	$(\frac{1}{2},\frac{3}{2},\frac{5}{2})$	0.0762$(\frac{1}{2}^+)$	0.0718	+6	$\frac{1}{2}^+,\frac{1}{2}^-,(\frac{9}{2}^+,\frac{9}{2}^-)$
5760.1	$(\frac{1}{2},\frac{3}{2},\frac{5}{2})$	0.161 $(\frac{5}{2}^+)$	0.204	-21	$\frac{5}{2}^+,\frac{5}{2}^-$
5934.2			0.0401		$\frac{1}{2}^+,\frac{1}{2}^-,(\frac{9}{2}^+,\frac{9}{2}^-)$
5967.8	$(\frac{1}{2},\frac{3}{2})^-$	0.0627$(\frac{1}{2}^-)$	0.0358	+75	$\frac{1}{2}^+,\frac{1}{2}^-,(\frac{9}{2}^+,\frac{9}{2}^-)$
6041.5	$(\frac{3}{2},\frac{5}{2},\frac{7}{2})$	0.113 $(\frac{5}{2}^+)$	0.0407	+64	$\frac{5}{2}^+,\frac{5}{2}^-,\frac{7}{2}^+,\frac{7}{2}^-$

The value of the spin used in the final calculated value for the population of levels whose previously measured spins have more than one value is given in brackets in the column along with the population value.

There were a number of problems in dealing with the sodium spectrum. The 3853 keV level decays partially by means of a 1777 keV gamma ray which was unresolved from the 1778 keV background and its Compton continuum. The value found by subtracting the known background led to agreement with prior measurements of the branching ratio for the level. The error

in this value could be as high as 40% however. The 5740 and 5760 keV levels were assumed to both decay by means of ground state transitions producing a broad doublet. Thus, the error in the relative population of these two levels could be quite large. Finally, the 5934 and 5970 keV ground state transitions were not completely resolved. In this case the overlap did not cause any large possible error.

The sodium results gave reasonable agreement with prior results used to calculate population values except for the lowest level at 441 keV and for higher energy states at 5970 and 6045 keV. In the case of the 441 keV level the probable reason for the discrepancy is the fact that the neutron flux was assumed to have a simple exponential distribution. The upper levels could be in error due to the presence of a number of higher levels in the range 6 to 7 MeV.

The 5374 keV level which was listed as a 5/2 or 3/2 level is a 5/2 level. The 5538 keV level which was listed as a 1/2 or 7/2 level is a 1/2 level. The 5740 and 5760 keV levels are somewhat coupled in their decay modes due to the doublet nature of the gamma rays depopulating them. However, the 5740 keV level appears to be a 1/2 level and the 5760 keV level a 5/2 level. The remainder of the levels have a limited number of choices for their spins. Predicted spin values which are unlikely due to the decay mode are indicated in brackets in table 4-4C.

4-5 Fluorine Results

Fluorine was studied using a series of compounds, namely: lithium fluoride, sodium fluoride, calcium fluoride, and lead fluoride. The common lines to all these spectra were attributed to inelastic neutron scattering on ^{19}F except for background lines. The various spectra were calibrated using thermal capture lines which occurred as background. The efficiency calibration was checked using the fluorine lines as well as the capture gamma ray lines in the various spectra and found to be constant throughout the various runs with a given detector in spite of the radiation damage which occurred. Previous results for ^{19}F have been summarized in the Nuclear Data Sheets(67).

Table 4-5A lists the gamma rays due to inelastic neutron scattering on ^{19}F and table 4-5B gives the branching ratios. Table 4-5C gives the experimental population values and compares them to the calculated values based on previous spin and parity measurements. Due to the nature of the decay modes and resultant spectrum of fluorine, normalization of the data presented a problem. This occurred because of the lack of states in the 2 MeV region which is usually the most populous region of the spectrum. The 1555 keV level was chosen for the normalization. The low energy of the level means it is not a good one to choose for normalization but it is the best available. Numerous doublets in the spectrum also limit the the accurracy of the results. Figure 4-5 gives the proposed

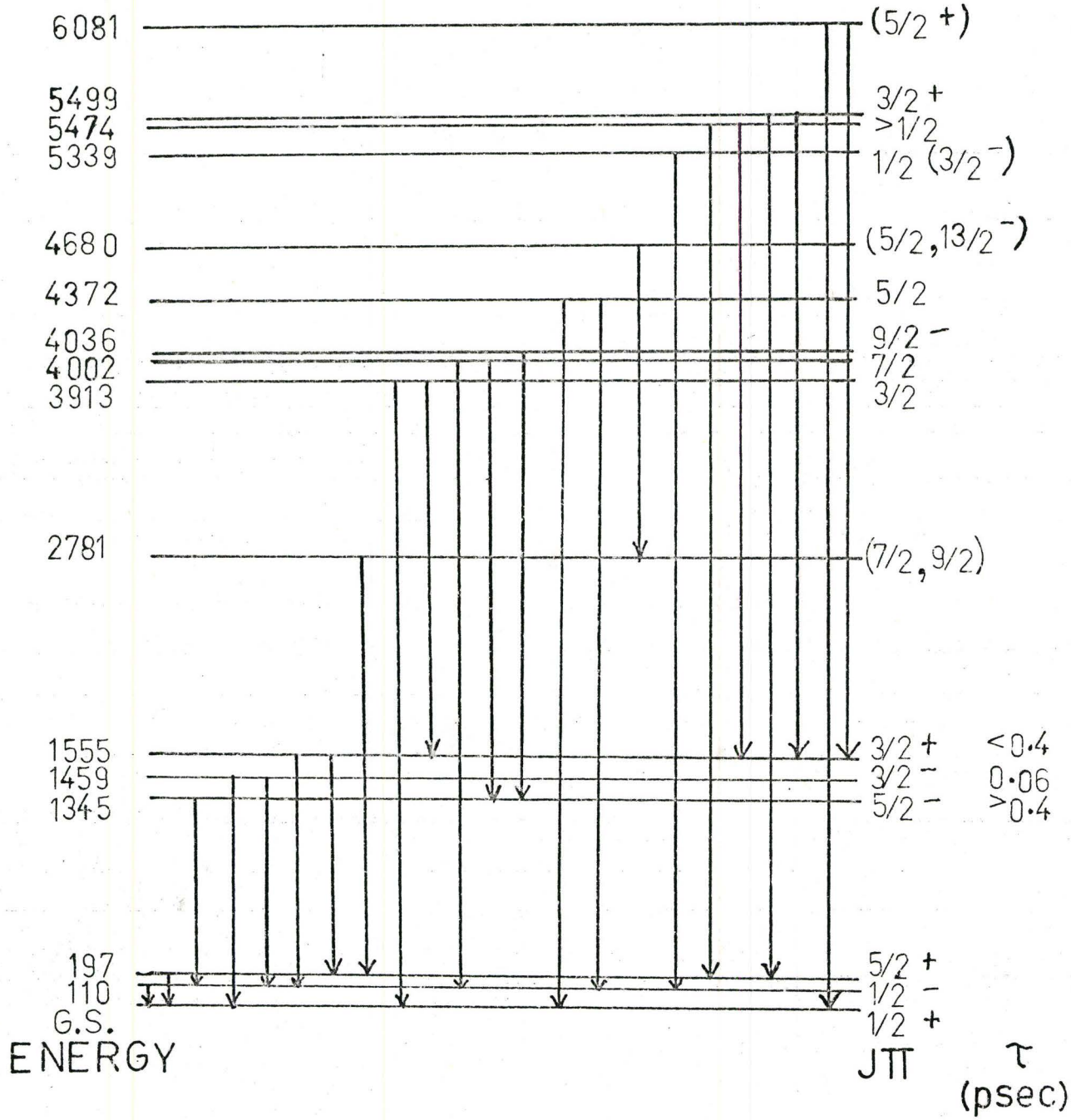

Fig. 4-5 ^{19}F Decay Scheme

decay scheme for ^{19}F.

Table 4-5A

Gamma Rays Produced by the $^{19}F(n,n'\gamma)^{19}F$ Reaction

Energy (keV)	Relative Intensity	Energy (keV)	Relative Intensity
110.1	not measured	3891.9	0.0400
197.2	not measured	3914.0	0.283
1234.8	3.341	3920.0	0.072
1348.9	3.232	3944.5	0.072
1357.7	6.623	4262.4	0.151
1445.0	0.264	4370.9	0.0500
1458.2	0.812	4525.4	0.0200
1898.9	0.0321	5228.9	0.782
2358.3	0.0700	5277.4	0.0384
2589.2	0.721	5301.4	0.0485
2656.5	0.159	6081.5	0.0600
2690.5	0.0798		

Table 4-5B

Branching Ratios for ^{19}F Levels

Energy Initial Level		Final Level	Branching Ratio (%)	
Present Work	Other Work		Present Work	Other Work
110.1	109.8+	g.s.	100	100+
197.2	197.1+	g.s.	100	100+
1344.9	1345.8+	110	100	100+

+ White[68]

Energy Initial Level		Final Level	Branching Ratio	
Present Work	Other Work		Present Work	Other Work
1458.8	1458.2+	g.s. 110	20 80	20+ 80+
1554.9	1554.0+	110 197	4 96	3+ 97+
2781.4	2783*	197	100	100*
3913.2	3913*	g.s. 1555	80 20	
4001.6	4002*	110 1345	20 80	
4035.8	4038*	1345	100	
4372.1		g.s. 110	25 75	
4680.3		2781	100	
5339.0	5338.8*	110	100	100*
5474.6	5473.7*	197 1555	35 65	
5499.0	5498.2*	197 1555	40 60	60* 40*
6081.2		g.s. 1555	75 25	

+ White (68) * Nuclear Data Sheets (67)

Table 4-5C

Experimental Population Values and Calculated Values for ^{19}F

Level Energy (keV)	Previous $J\pi$	Calculated Population	Experimental Population	% Difference	Possible $J\pi$ Values
110.1	1/2-	13.47	-	-	-
197.2	5/2+	12.83	-	-	-
1344.9	5/2-	3.45	3.10	+11	$\frac{1}{2}^+,\frac{1}{2}^-,\frac{5}{2}^+,\frac{5}{2}^-$
1458.8	3/2-	4.036	4.04	0	$\frac{1}{2}^+\frac{1}{2}^-\frac{3}{2}^+\frac{3}{2}^-\frac{5}{2}^+\frac{5}{2}^-$
1554.9	3/2+	6.34	6.34	0	$\frac{1}{2}^+\frac{1}{2}^-\frac{3}{2}^+\frac{3}{2}^-\frac{5}{2}^+\frac{5}{2}^-$
2781.4	$(\frac{7}{2},\frac{9}{2})$	0.596$(\frac{7}{2}^+)$	0.690	-14	$\frac{1}{2}^+,\frac{1}{2}^-,\frac{7}{2}^+,\frac{7}{2}^-$
3913.2	3/2	0.344	0.350	-17	$\frac{3}{2}^+,\frac{3}{2}^-,\frac{5}{2}^+,\frac{5}{2}^-$
4001.6	7/2	0.213	0.199	+7	$\frac{1}{2}^+,\frac{1}{2}^-,(\frac{7}{2}^+,\frac{7}{2}^-)$
4035.8	9/2-	0.096	0.080	-20	$\frac{9}{2}^+,\frac{9}{2}^-$
4372.1	5/2	0.231	0.201	+15	$\frac{1}{2}^+\frac{1}{2}^-\frac{3}{2}^+\frac{3}{2}^-\frac{5}{2}^+\frac{5}{2}^-$
4680.3	$(\frac{5}{2},\frac{13}{2}^-)$	0.0310$(\frac{13}{2}^-)$	0.0322	-3	$\frac{13}{2}^+,\frac{13}{2}^-$
5339.0	$\frac{1}{2}(\frac{3}{2}^-)$	0.0682$(\frac{1}{2})$	0.0784	-13	$\frac{1}{2}^+\frac{1}{2}^-\frac{3}{2}^+\frac{3}{2}^-\frac{5}{2}^+\frac{5}{2}^-$
5474.6	$\frac{1}{2}$		0.114		$\frac{3}{2}^+,\frac{3}{2}^-,\frac{5}{2}^+,\frac{5}{2}^-$
5499.0	3/2+	0.0965	0.119	-19	$\frac{3}{2}^+,\frac{3}{2}^-,\frac{5}{2}^+,\frac{5}{2}^-$
6081.2	(5/2+)	0.0521	0.0800	-35	$\frac{1}{2}^+,\frac{1}{2}^-,\frac{5}{2}^+,\frac{5}{2}^-$

The present results are in agreement with previous measurements. The population of the two lowest states was not measured due to difficulties in observing the low energy decay of these levels. The state at 2783 keV which was previously listed as 9/2 or 7/2 appears to be a 7/2 level. The 4681 keV level which was reported as a 5/2 or 13/2 level is a 13/2 level. The fact that this level only decays to a high spin level (7/2 level at 2783 keV) is additional confirmation of this fact.

The possible error in a number of the experimental population values is very high due to the doublets in the spectrum. The level at 6080 keV appears to have a population value two times higher than any calculated possible spin values suggesting the possibility that the level may in fact be a doublet with unresolved gamma rays decaying to the ground state.

4-6 Nitrogen Results

Nitrogen was studied in order to test the Hauser Feshbach formalism and assumed model for very light elements. The authors of the table of neutron transmission coefficients point out that the optical model and the coefficients have limited validity for $A < 20$. The nitrogen spectrum was obtained using a melamine ($C_6N_3H_6$) target. Only the cadmium neutron filter was used and as a result there was a significant contribution to the spectrum due to the $^{14}N(n,\gamma)^{15}N$ reaction[48] which was used for calibration. Nitrogen occurs in nature

as 99.6% ^{14}N so that it is almost monoisotopic. Ajzenberg-Selove[69] has summarized the prior results for nitrogen in a review article.

Table 4-6A lists the gamma rays due to the $^{14}N(n,n'\gamma)^{14}N$ reaction and table 4-6B gives the branching ratios. Table 4-6C gives the experimental population values and compares them to the calculated values. Figure 4-6 gives the proposed decay scheme for ^{14}N. Normalization of the data to the calculated values was a problem. Initial attempts to normalize the 2312 keV level led to all experimental values being low compared to the calculated values. It was found that the only reasonable results occurred if the 3946 keV level was used for normalization.

Table 4-6A

Gamma Rays Produced by the $^{14}N(n,n'\gamma)^{14}N$ Reaction

Energy (keV)	Relative Intensity	Energy (keV)	Relative Intensity
727.2	0.0982	3946.8	0.0300
1338.8	0.0045	4914.0	0.0544
1633.4	0.472	5104.4	0.272
2312.4	1.820	5693.0	0.0263
2498.0	0.00896	5830.5	0.0328
2793.6	0.0590	6197.6	0.0131
3381.4	0.0487	6444.2	0.0314
3884.6	0.0394		

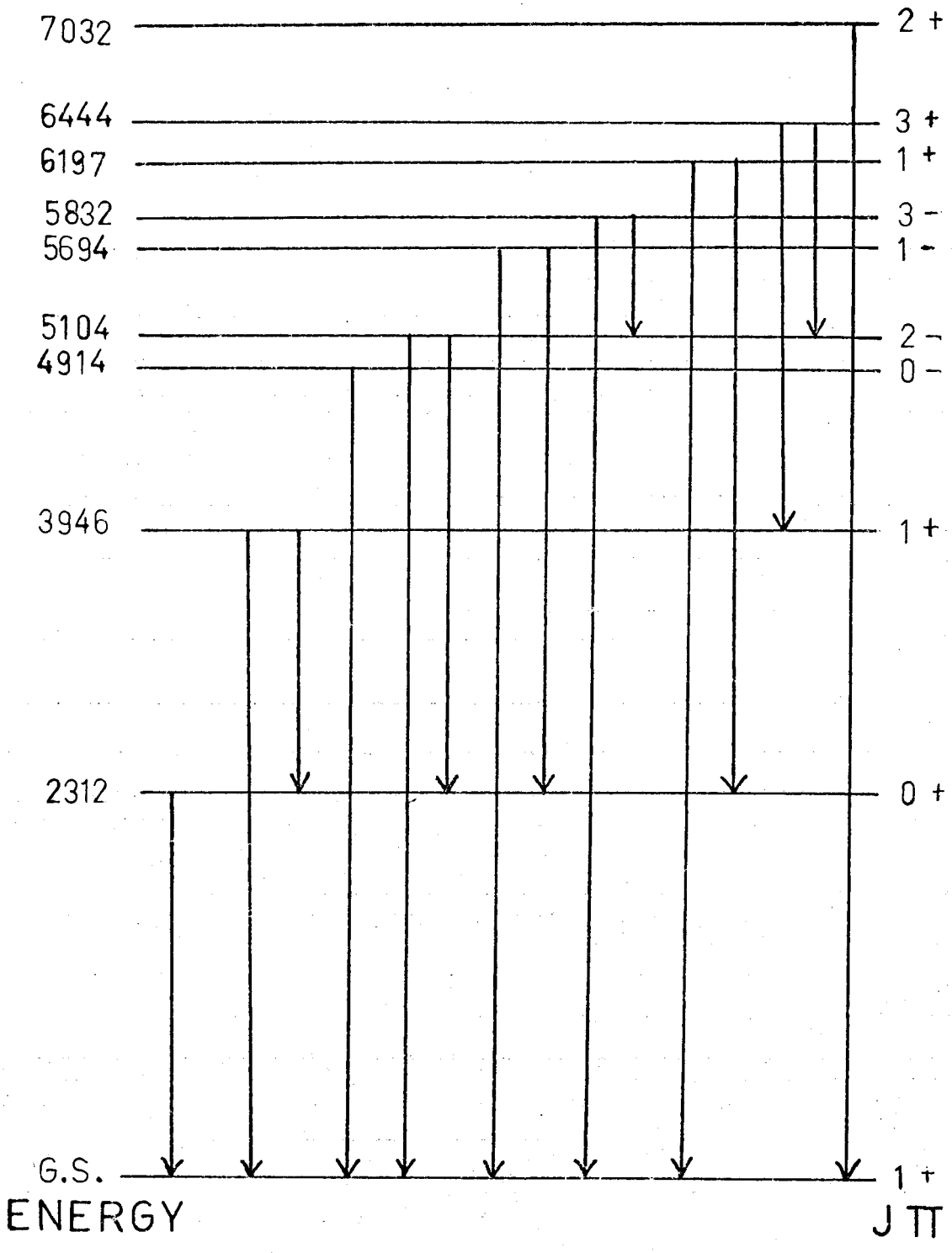

Fig. 4-6 ^{14}N Decay Scheme

Table 4-6B

Branching Ratios for ^{14}N Levels

Energy Initial Level		Final Level	Branching Ratio (%)	
Present Work	Ajzenberg-Selove		Present Work	Ajzenberg-Selove
2312.4	2312.81	g.s.	100	100
3945.8	3944.7	g.s.	6	3.9
		2312	94	96.1
4914.0	4913.4	g.s.	100	100
		2312	-	0.4
		3945	-	1.3
5104.4	5105.87	g.s.	82	79.9
		2312	18	19.7
		3945	-	0.8
5693.5	5691	g.s.	35	38.1
		2312	65	61.9
		3945	-	2
		4913	-	2
5831.5	5833	g.s.	25	21.3
		5104	75	78.8
6197.2	6197.6	g.s.	25	23.8
		2312	75	75.2
6444.2	6443.6	g.s.	70	73.1
		3945	20	18.9
		5104	10	6.8
		5833	-	2

Table 4-6C

Experimental Population Values and Calculated Values for ^{14}N

Level Energy (keV)	Previous $J\pi$	Calculated Population	Experimental Population	% Difference	Possible $J\pi$ Values
2312.4	0+	0.797	1.20	-33	0+,4+,4-
3945.8	1+	0.493	0.493	0	1+1-2-3-4+4-
4914.0	0-	0.0680	0.0544	+24	0-,1-
5104.4	2-	0.220	0.228	-4	2+,2-,3+,3-
5693.5	1-	0.0998	0.0750	+33	1+,1-,4+,4-
5831.5	3-	0.112	0.131	-15	2+,2-,3+,3-
6197.2	1+	0.0579	0.0525	+10	1+,1-,4+,4-
6444.2	3+	0.0652	0.0448	+45	1+,1-,2+,2-, 3+,3-,4+,4-

The experimental population values for nitrogen led to the poorest agreement with previous results of all the isotopes studied. The experimental problems for nitrogen were more severe than for the other isotopes studied largely because of the large (n,γ) component of the spectrum. The coefficients may also have been of limited value. There was evidence of the $^{14}N(n,\alpha)^{11}B$ reaction since a 2141 keV gamma ray which could de-excite the first state in boron was observed. No corrections were made in the calculated values for fast neutron reactions other than inelastic scattering.

4-7 Boron Results

Boron was studied in addition to nitrogen in order to test the model used in this work on light elements. Boron was studied using a boron phosphide sample and also using a boron powder sample. Both samples were encapsulated in aluminum and aluminum capture gamma rays were used for calibration. Natural boron consists of 19.6% ^{10}B and 80.4% ^{11}B. ^{10}B has a very large cross section for the (n,α) reaction and as a result there was no evidence of the $^{10}B(n,n'\gamma)^{10}B$ reaction. The $^{10}B(n,\gamma)^{11}B$ reaction populates states in ^{11}B. All broadened lines appeared to belong to the $^{11}B(n,n'\gamma)^{11}B$ reaction. The inelastic neutron reaction was enhanced for the heavier isotope compared to the lighter one for several reasons. The heavier one is four times more abundant in the sample. The ground state spin leads to almost a factor of two times in favour of the ^{11}B case due to the $1/(2I+1)$ term in the Hauser Feshbach formalism. Finally the large (n,α) cross section limits the $(n,n'\gamma)$ reaction. The capture lines due to the lighter isotope overlapped the lines due to inelastic scattering on ^{11}B. The 7006 keV, 5+% transition[70] which occurs as a transition from the capture state in ^{11}B was used to correct the intensities of overlapping lines. In addition the peak widths in the two reactions were quite different allowing them to be separated. The correction due to the overlap was relatively small. This was primarily due to the competition of the (n,α) reaction on ^{10}B.

Table 4-7A lists the gamma rays due to the $^{11}B(n,n'\gamma)^{10}B$ reaction and table 4-7B gives the branching ratios. Table 4-7C gives the experimental population values and compares them to the calculated values. Figure 4-7 gives the proposed decay scheme for ^{11}B. The lowest energy level in ^{11}B (2141 keV) was used for normalization of the data.

Table 4-7A

Gamma Rays Produced by the $^{11}B(n,n'\gamma)^{11}B$ Reaction

Energy (keV)	Relative Intensity	Energy (keV)	Relative Intensity
2141.2	2.006	5028.4	0.281
2275.8	0.0024	5845.0	0.0050
2294.0	0.0300	6431.2	0.0054
2861.3	0.00122	6738.6	0.0710
2888.4	0.0700	6808.0	0.0369
4125.1	0.00179	7305.7	0.0244
4445.1	0.546	7987.2	0.0050
4472.8	0.0007	8571.5	0.0090
4668.1	0.0123	8919.4	0.0156

Table 4-7B

Branching Ratios for ^{11}B Levels

Energy Initial Level		Final Level	Branching Ratio (%)	
Present Work	Thomas[70] et al		Present Work	Olness[71] et al
2141.2	2140	g.s.	100	100
4445.1	4445	g.s.	100	100
		2141	-	0.5

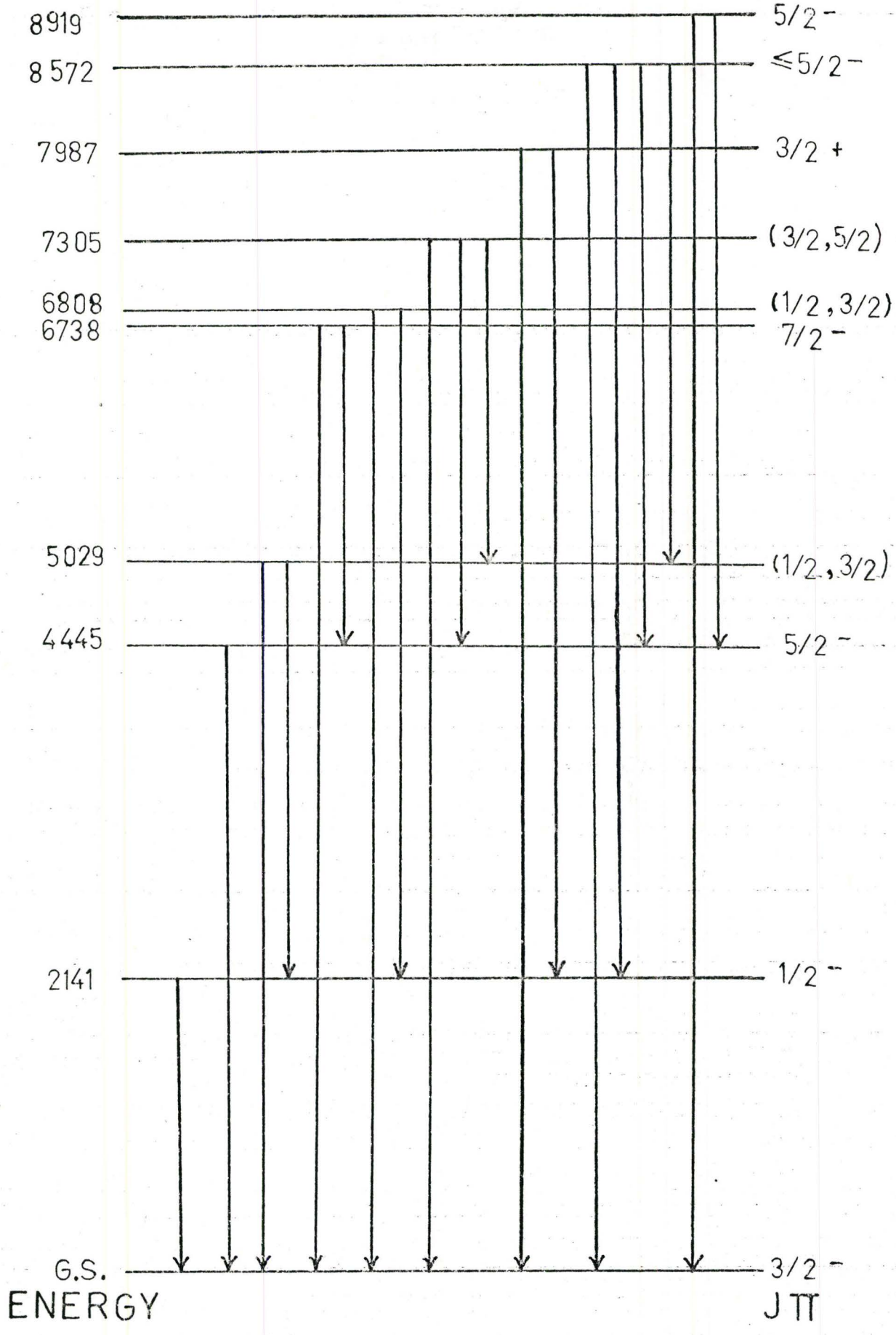

Fig. 4-7 ^{11}B Decay Scheme

Energy Initial Level		Final Level	Branching Ratio (%)	
Present Work	Thomas et al		Present Work	Olness et al
5028.8	5030	g.s.	80	85
		2141	20	15
		4445	-	0.3
6738.7	6739	g.s.	70	70
		2141	-	3
		4445	30	30
		5029	-	1
6808.2	6810	g.s.	75	71
		2141	25	29
		4445	-	8
		5029	-	8
7305.7	7300	g.s.	85	87
		2141	-	1
		4445	5	5.5
		5029	10	7.5
7986.7	7990	g.s.	50	47
		2141	50	53
		4445	-	1
		5029	-	1
8571.5	8570	g.s.	50	56
		2141	30	30
		4445	10	5
		5029	10	9
8919.4	8920	g.s.	96	95
		2141	-	1
		4445	4	4.5

Table 4-7C

Experimental Population Values and Calculated Values for ^{11}B

Level Energy (keV)	Previous $J\pi$	Calculated Population	Experimental Population	% Difference	Possible $J\pi$ Values
2141.2	1/2-	1.914	1.914	0	$\frac{1}{2}+,\frac{1}{2}-,\frac{9}{2}+,\frac{9}{2}-$
4445.1	5/2-	0.613	0.512	+20	$\frac{3}{2}+\frac{3}{2}-\frac{5}{2}+\frac{5}{2}-\frac{7}{2}+\frac{7}{2}-$
5028.8	$(\frac{1}{2},\frac{3}{2})$	0.285(3/2) 0.144(1/2)	0.347	-18	$\frac{3}{2}-\frac{5}{2}+\frac{5}{2}-\frac{7}{2}-$
6738.8	7/2-	0.0787	0.101	-22	$\frac{5}{2}+,\frac{5}{2}-,\frac{7}{2}-$
6808.2	$(\frac{1}{2},\frac{3}{2})$	0.0553(3/2) 0.0290(1/2)	0.0492	+12	$\frac{3}{2}+,\frac{3}{2}-,\frac{9}{2}+,\frac{9}{2}-$
7305.7	$(\frac{3}{2},\frac{5}{2})$	0.0331(5/2) 0.0448(3/2)	0.0244	+30	$\frac{5}{2}+,\frac{5}{2}-$
7986.7	3/2+	0.0197	0.0190	+4	$\frac{1}{2}+,\frac{1}{2}-,\frac{3}{2}+$
8571.5	5/2-	0.0166(5/2) 0.0126(3/2)	0.0179	-7	$\frac{3}{2}+,\frac{3}{2}-,\frac{5}{2}+,\frac{5}{2}-,\frac{7}{2}$
8919.4	5/2-	0.0114	0.0163	-31	$\frac{5}{2}+,\frac{5}{2}-,\frac{7}{2}+,\frac{7}{2}-$

The present experimental and calculated results yielded better agreement than the nitrogen results. The 5029 keV level appears to be a 3/2 spin state, the 6808 keV level a 3/2 state and the 7306 keV level a 5/2 state. The 8572 keV level is either a 3/2 or 5/2 level with the 5/2 value

more likely. One of the problems in handling the experimental data for both nitrogen and boron is the extreme broadening which occurred especially at high gamma ray energies. For both boron and nitrogen the (n,γ) reaction limits the accurracy of the population values.

CHAPTER 5

STOPPING POWER CALCULATIONS

5-1 Introduction

When a fast neutron ($\sim$ 2 MeV) interacts with an atom (A$\sim$19) in a solid, it gives the atom on the average approximately 100 keV of recoil energy. If the atom then emits a gamma ray before slowing down as the result of collisions in the medium, it will be Doppler shifted due to the motion of the nucleus. If the lifetime of the excited state is in a reasonable range ($\sim$ 0.1 psec), then the resultant Doppler shift effect, which leads to a broadening of the gamma ray due to the geometry of the target and reactor, will be less than the maximum possible if there was no slowing down. The reduced width of the peak gives a measure of the stopping power of the medium or the half life of the nucleus depending on which is known previously. From figure 4-5 it can be seen that ^{19}F has several states with lifetimes in the required region. The purpose of this chapter is to demonstrate the feasibility of measuring the stopping power of different media or the lifetimes of states using the internal target facility.

Northcliffe and Schilling have compiled tables[72] of stopping powers for various ions and media based on experimental data up to 1970 and have extrapolated the tables using the theory given in a 1963 review article[73] to cover

all mass and energy ranges. The slowing down of energetic atoms in matter is determined by two processes: electronic and nuclear. At high energy the electronic process, which varies as the velocity of the atom, dominates. At low energy (< 100 keV) the nuclear process, which varies inversely with the velocity of the atom, dominates. In the energy region 10-200 keV, figure 1 of Northcliffe's work[72] indicates that the stopping power for a ^{19}F atom is approximately constant. This occurs as a result of the fact that the electronic and nuclear components of the stopping power are equal in magnitude at approximately 100 keV.

The effect of the Doppler broadening can be calculated for this work by defining a Doppler attenuation factor (F)

$$F = \frac{\Delta E_\gamma(\langle v \rangle)}{\Delta E_\gamma(\langle v_o \rangle)} \quad ,$$

where $\Delta E_\gamma(\langle v_o \rangle)$ is the maximum broadening obtained by calculating the average initial velocity ($\langle v_o \rangle$) of the recoiling atom, and $\Delta E_\gamma(\langle v \rangle)$ is the actual broadening observed. $\langle v \rangle$ is the average velocity of the ion at the time of emission of the gamma ray. In section 2-8 of this work it was shown that $\Delta E_\gamma(\langle v_o \rangle) = \frac{E_\gamma}{c}(V_A + V_C)$. For the purpose of this work it will be assumed that the broadeninng

$$\Delta E_\gamma(\langle v \rangle) \propto \langle v \rangle \quad ,$$

where $v = V_C$. Thus the attenuation factor becomes

$$F = \frac{\langle v \rangle}{\langle v_o \rangle} \quad .$$

If a lifetime τ is assumed for the excited state, then

$$\langle v \rangle = \frac{1}{\tau} \int_0^\infty v(t).\exp(-\frac{t}{\tau}).dt,$$

where v(t) is the velocity of the ion at the time of emission of the gamma ray. In section 2-8 the average initial center of mass velocity was calculated to be

$$\langle v_o \rangle = \sqrt{\frac{2.(E_x + \Delta)}{M.A.A}}.$$

If the stopping power is a constant in the region of interest then $v(t) = \langle v_o \rangle - \alpha.t$,

where $\alpha = \frac{10^6.\rho.c^2}{103.A.931} . \frac{dE}{dx}$ and

$\frac{dE}{dx}$ is the stopping power measured in units of keV-cm^2/μg.

A is the mass of fluorine and ρ is the density of the medium.

Thus $\langle v \rangle = \frac{1}{\tau} . \int_0^{\alpha/v_o} (\langle v_o \rangle - \alpha.t).\exp(-\frac{t}{\tau}).dt.$

$= \langle v_o \rangle - \alpha.\tau + \alpha.\tau.\exp(-\beta)$ where $\beta = \frac{\langle V_o \rangle}{\alpha.\tau}$.

The upper limit of integration in this equation is $\frac{\alpha}{v_o}$

since v(t) = 0 for t greater than this value of t. Thus

$$F = 1 - (\frac{1}{\beta}) + (\frac{1}{\beta}).\exp(-\beta) \quad .$$

Figure 5-1 gives a graphical representation of this equation. If a density of 2 g/cc and a stopping power of 2 keV-cm^2/μg for a medium is assumed, then a lifetime in the range 0.1 to 1 psec is required for a state at 1.5 MeV in an element of mass 19 to give a value of F in a reasonable range to be measured (0.2 to 0.8).

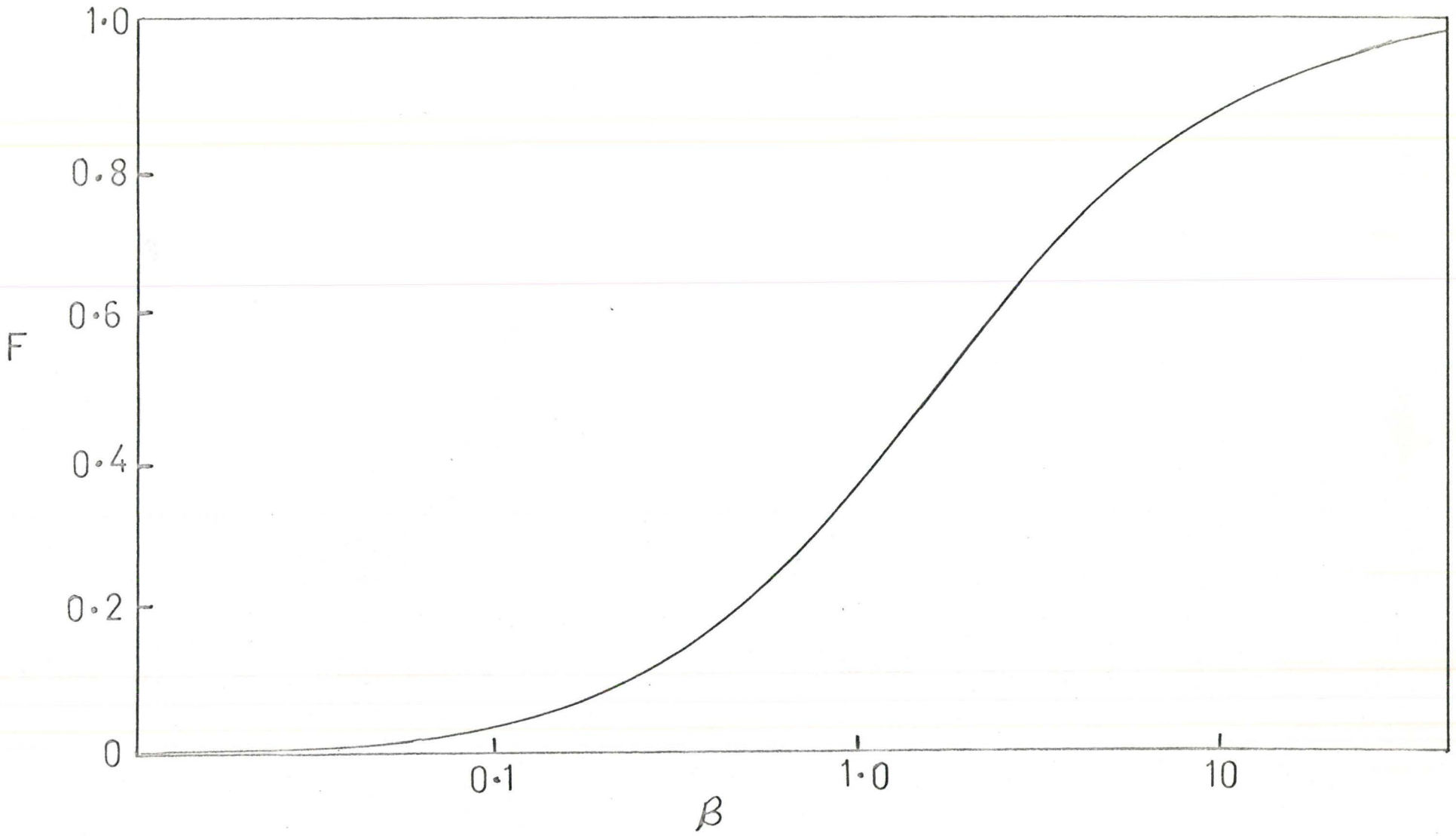

Figure 5-1 A plot of the equation $F = 1 - \frac{1}{\beta} + \frac{1}{\beta}.\exp(-\beta)$.

5-2 Experimental Results

The width of the peaks was measured using three different techniques: hand fitting, using a Gaussian computer fitting program and using probability graph paper. Figure 5-2A and 5-2B show the result of plotting a typical thermal capture line and a broadened line on probability paper. If the peaks were Gaussian shaped a straight line would result. Both lines appeared to be Gaussian if the points in the lower 10% of the peak are neglected. The 1348-1356 keV doublet in ^{19}F was analyzed by hand. The remaining lines in fluorine were analyzed by all three methods giving similar results. The widths of the broadened lines were corrected for the response of the Ge(Li) detector system. Figure 5-3 gives the typical resolution of the detector for capture lines after subtracting the electronic noise out. The slope of one indicates that the charge collection efficiency varies as E^1 as it should.

Table 5-1 gives the results obtained for the stopping power of various media. For each compound, the widths of gamma rays de-exciting the 1458 keV level of ^{19}F were measured. The lifetime[68] of this level was known to be 0.06 psec. F was found using the definition given by the ratio of the actual broadening divided by the calculated maximum broadening. The value for $\frac{dE}{dx}$ was obtained by substituting in the equation given on page 105, for F, τ, V_o and solving for α and in turn for

$\frac{dE}{dx}$ of the compound. The tabulated values of the stopping power were obtained using the relation(74)

$$\frac{dE}{dx}(\text{compound}) = n_1 \cdot \frac{dE}{dx})_1 + n_2 \cdot \frac{dE}{dx})_2 + \ldots$$

where n_k is the atomic fraction of the k^{th} element and $\frac{dE}{dx})_k$ is the stopping power of that element obtained from Northcliffe's tables.

Table 5-1

Stopping Power Results

Compound	Line (keV)	τ (psec)	E(exp't) (keV)	F	$\frac{dE}{dx}$(exp't)	$\frac{dE}{dx}$(table)
LiF	1458	0.06	11.7	0.97	0.39	2.39
	1348	0.06	11.4	0.95	0.64	
NaF	1458	0.06	9.5	0.79	2.70	1.99
	1348	0.06	10.0	0.83	2.18	
CaF_2	1458	0.06	8.1	0.68	3.10	1.81
	1348	0.06	7.9	0.66	3.50	
PbF_2	1458	0.06	0	0	4.9	1.46
	1348	0.06	0	0	4.9	

The lifetime values in table 5-1 are given in the units keV-$cm^2/\mu g$.

Table 5-2 gives the results of measurements used to determine the lifetime of the 1554 and 1346 keV levels in ^{19}F. The 1554 keV level decays by a strong 1356 keV gamma ray and by an extremely weak 1444 keV line. The 1346 keV level decays by a 1235 keV gamma ray. In table 5-2 the value of $\frac{dE}{dx}$ was set equal to the average value obtained experimentally in

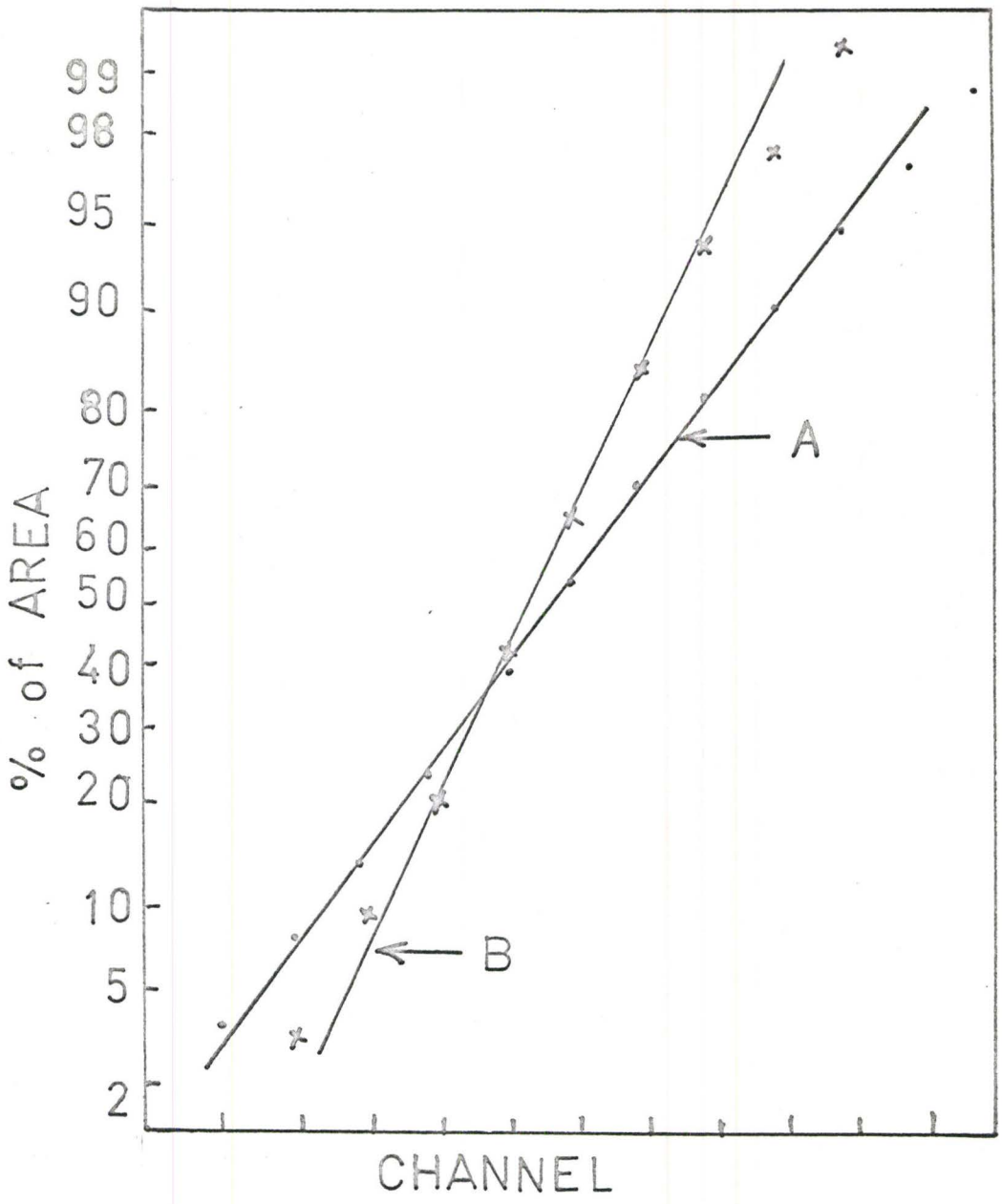

Figure 5-2 Peak Shape. The curves show the result of plotting an inelastic peak (A) and a capture gamma ray peak (B) on a Gaussian probability graph. A Gaussian response would give a straight line on this graph.

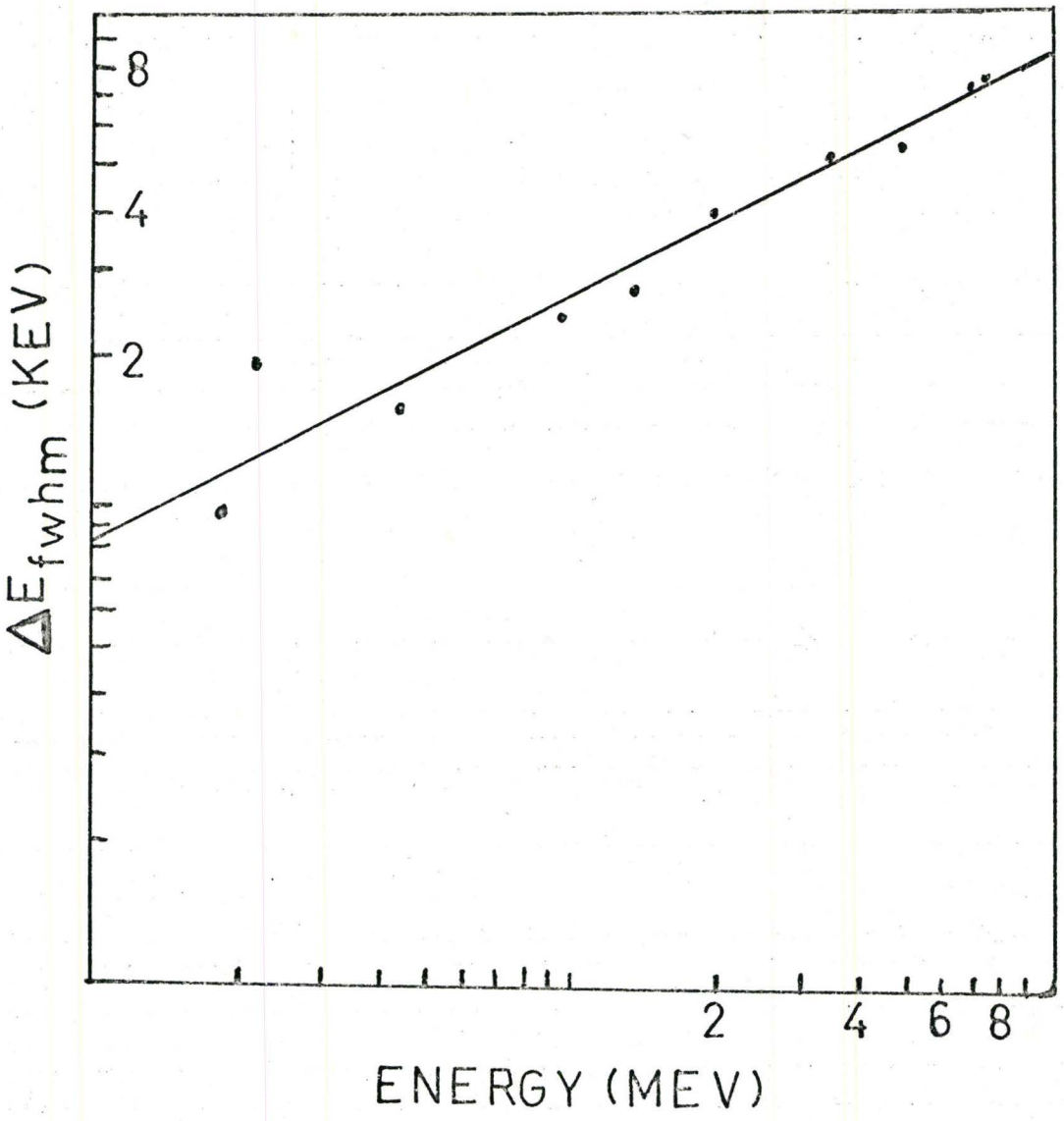

Figure 5-3 Detector Resolution Versus Energy. The curve has been corrected for the electronic noise of the system.

table 5-1. The value for τ was obtained by solving the equation for F given on page 105.

Table 5-2

Lifetime Measurements

Compound	Line (keV)	$\frac{dE}{dx}$	E(exp't) (keV)	F	τ(exp't) (psec)	(White[68]) (psec)
LiF	1235	0.52	1.73	0.14	1.3	0.4
	1356	0.52	9.8	0.79	0.31	0.4
NaF	1356	2.44	8.5	0.71	0.09	0.4
CaF_2	1356	3.30	6.0	0.50	0.44	0.4

The possible experimental errors for the measured values of the stopping power in table 5-1 and of τ in table 5-2 are of the order of 20 to 40%. This arises primarily because of the unresolved 1348-1356 keV doublet in the decay scheme.

5-3 Discussion of Stopping Power Results

The results obtained in tables 5-1 and 5-2, although somewhat limited in value, demonstrate the feasibility of using the facility to obtain information regarding stopping power and lifetimes. The results for PbF_2 were meaningless since the value of F was in a region where it was not very sensitive to the value of β.

There are a number of severe experimental limitations on the use of the facility for stopping power and lifetime experiments. The fact that there is a continuous energy spectrum of neutrons interacting with the target over a wide range of incident angles implies that the target nuclei recoil

with a wide range of velocities. This means that the stopping power obtained is an average value over a wide range of energies. No correction was made for the fact that the atoms change direction as they slow down. This is particularly important at low energies, when nuclear collisions predominate. Another problem is that the energy levels which have reasonable lifetimes for use in measuring the stopping power usually have a 1-2 MeV gamma ray decay mode. This region is the one of lowest sensitivity for the pair mode of the detection system. In addition there is a reasonably large scattered gamma ray background at lower energies. In addition to the reduction of the broadening due to slowing down effects, the energy shift is also reduced. In the case of ^{19}F, two of the levels which have a reasonable lifetime produce a doublet which is only poorly resolved. One other limitation in the calculation is the assumption that the stopping power is constant in the energy region used, and that $\Delta E_\gamma(\langle v \rangle) \propto V_c$. Some of these problems could be eliminated by doing this type of experiment using an external beam port facility. The Doppler shift could be measured instead of the broadening in this case.

CHAPTER 6

DISCUSSION OF RESULTS

6-1 General Conclusions

This work has demonstrated that the $(n,n'\gamma)$ reaction can be profitably studied using a light water, enriched fuel reactor source of neutrons. In particular it has been demonstrated that spin information can be obtained from studying the cross section of the $(n,n'\gamma)$ reaction for each level. The Doppler broadening and energy shift effects have been adequately explained by kinematic arguments. Chapter 5 has shown that stopping power and lifetime experiments can be performed using the facility. Table 6-1 gives some idea of how well the present experimental results and the calculated values for the population values based on previous measurements agree.

Table 6-1

Comparison of Calculated and Experimental Population Values

Isotope	Number of Levels of Known J	Difference Between Calculated and Exp'l Valu			
		<11%	11-20%	21-30%	>30%
^{28}Si	11	5	3	2	1
^{40}Ca	12	6	4	2	0
^{31}P	10	4	3	2	1
^{27}Al	13	6	3	4	0
^{23}Na	17	5	5	4	3
^{19}F	13	4	7	1	1

Isotope	Number of Levels	11%	11-20%	21-30%	30%
^{14}N	8	2	2	1	3
^{11}B	9	3	2	2	2
Total	92	34	29	18	11

The results given in this work are for elements in the mass range A = 11 to 40 and cover an energy range from approximately 1 to 6 MeV with a few higher levels in nitrogen, boron and silicon. The results show excellent agreement in general with previous work as well as giving information regarding spins of unknown levels. The light elements boron and nitrogen gave the poorest agreement with prior work. This was probably due to experimental difficulties with these elements and may also have been due to limitations of the neutron transmission coefficients used. The results do however suggest that the model has some validity even for very light elements. The fact that very few levels were observed above 6 MeV means that the effect of a possible direct reaction component at higher energy could not be evaluated.

6-2 Limitations of the Experiment

From table 6-1 one can see that the predicted population values of 60% of the known levels agreed within 20% error with the experimental results obtained in the present work. Of the remainder some may have had a larger error due to incorrect values of spins being assigned and some have a larger

error due to experimental problems. The possible error in this work due to statistical effects and intensity calibrations would be of the order of 10 to 15%. One of the limits on the sensitivity of the system was the large neutron capture component in the spectra. In future work, this could be reduced by using ^{10}B separated isotope in the boron filter and by extending the cadmium filter to improve the filtering of the neutrons. In addition samples could be encapsulated in carbon rather than aluminum in order to reduce unwanted background radiation. The 7725 keV transition in aluminum in particular limited the sensitivity at higher energy. Probably the next largest source of error was due to using an energy grid to calculate the yield as a function of energy along with a set of tables of neutron transmission coefficients. This meant that the energy of the levels was rounded off to the nearest 100 keV. A possible future extension of this work would be to calculate the transmission coefficients as a function of energy and vary the parameters of the optical model used to obtain the coefficients to obtain the best fit.

There were a number of minor possible corrections that were not allowed for. No correction was made on the cross section for the effect of competing fast neutron reactions. There was no attempt made to correct for attenuation of the gamma rays in the targets themselves. The neutron flux was assumed to be isotropic which was not strictly true. There

may also have been minor effects on the neutron flux distribution due to resonance effects in the filters and aluminum tubing. All of these effects were considered to introduce small errors compared to other sources of error so that no attempt was made to correct for them.

In addition to obtaining spin information, future possibilities for extending the present work include an investigation of Moldauer's theory and the possibility of explaining the results by a direct reaction mechanism especially at higher energies. The work concerning lifetimes and stopping powers could also be extended.

REFERENCES

(1) M. Mayer, Phys. Rev. 75, 1969 (1949).

(2) H. Feshbach, C. E. Porter and V. F. Weisskopf, Phys. Rev. 96, 448 (1954).

(3) V. F. Weisskopf, Phys. Rev. 52, 295 (1937).

(4) W. Hauser and H. Feshbach, Phys. Rev. 87, 366 (1952).

(5) J. B. Marion and J. L. Fowler, Fast Neutron Physics, Part II, P 1538, Interscience Publishers, John Wiley and Sons, New York (1963).

(6) Progress in Fast Neutron Physics based on Proceedings of the International Conference on Fast Neutron Physics held at Rice University, Feb. 1963, G. C. Phillips, J. B. Marion and J. R. Risser (editors), University of Chicago Press (1963).

(7) Nuclear Structure Study with Neutrons based on Proceedings of the International Conference on the Study of Nuclear Structure with Neutrons, Antwerp, July 1965, M. Neve de Mevergnies, P. Van Assche and J. Vervier (editors), North-Holland Publishing Co., Amsterdam (1966).

(8) Ibid. 2, P 450.

(9) M. Walt and J. R. Beyster, Phys. Rev. 98, 677 (1955).

(10) R. D. Woods and D. S. Saxon, Phys. Rev. 95, 577 (1956), M. A. Melkanoff, S. A. Moszkowski, J. Nodvik and D. S. Saxon, Phys. Rev. 101, 506 (1956).

(11) R. G. Schrandt, J. R. Beyster, M. Walt and E. W. Salmi, Report LA-2099 Physics, Los Alamos Scientific Laboratory of the University of California (1957).

(12) F. Bjorklund and S. Fernbach, Phys. Rev. 109, 1295 (1958).

(13) F. Perey and B. Buck, Nucl. Phys. 32, 353 (1962).

(14) P. B. Jones, The Optical Model in Nuclear and Particle Physics, John Wiley and Sons, New York (1963).

(15) D. J. Hughes, Pile Neutron Research, P. 14, Addison-Wesley Publishing Co., Reading Massachusetts (1953).

(16) BNL 765 (T-286), Physics-TID-4500, 18th edition.

(17) Ibid. 5, P. 1538.

(18) L. Wolfenstein, Phys. Rev. 82, 690 (1951).

(19) B. T. Feld, Final Report of the Fast Neutron Data Project, US Atomic Energy Commission Report NYO-636, unpublished (1951).

(20) A. M. Lane and R. G. Thomas, Rev. Mod. Phys. 30, 257 (1958)

(21) H. Feshbach, Nuclear Spectroscopy, Part B, P 625, editor F. Ajzenberg-Selove, Academic Press, New York (1960).

(22) G. K. O'Neil, Phys. Rev. 95, 1235 (1954).

(23) J. H. Towle and R. O. Owens, Nucl. Phys. A100, 257 (1967).

(24) L. Rosen and L. Stewart, Phys. Rev. 99, 1052 (1955), Phys. Rev. 107, 824 (1957).

(25) S. C. Mathur, R. S. Tucker, R. W. Benjamin and I. L. Morgan, Nucl. Phys. 73, 561 (1965).

(26) G. R. Satchler, Proc. Phys. Soc. 66A, 1081 (1953), Phys. Rev. 94, 1304 (1954), Phys. Rev. 104, 1198 (1956) and errata 111, 1747 (1958).

(27) A. M. Lane and J. E. Lynn, Proc. Phys. Soc. London A70, 557 (1957).

(28) L. Dresner, Proceedings of the International Conference on Neutron Interactions with the Nucleus, Columbia University, CU-175, P 71, unpublished (1957).

(29) C. E. Porter and R. G. Thomas, Phys. Rev. 104, 483 (1956).

(30) P. Moldauer, Phys. Rev. 123, 968 (1961), Phys. Rev. 129, 754 (1963), Phys. Rev. 135, B642 (1964), Rev. Mod. Phys. 36, 1078 (1964).

(31) L. Torop, Nucl. Phys. A111, 513 (1968).

(32) S. C. Mathur, P. S. Buchanan, and I. L. Morgan, Phys. Rev. 160, 816 (1967).

(33) S. C. Mathur, R. S. Tucker, R. W. Benjamin, and I.L. Morgan, Nucl. Phys. 73, 561 (1965).

(34) R. W. Benjamin, P. S. Buchanan, and I. L. Morgan, Nucl. Phys. 79, 241 (1966).

(35) D. J. Donahue, Phys. Rev. 128, 1231 (1962).

(36) J. B. Guernsey and A. Wattenberg, Phys. Rev. 101, 1516 (1956).

(37) Ibid. 6, P 143.

(38) P. I. C. Ernst, Master's Thesis, McMaster University (1968).

(39) Research Reactors, P 107, United States Atomic Energy Commission, McGraw Hill, New York (1955).

(40) L. Nichol, A. Lopez, A. Robertson, W. V. Prestwich, T. J. Kennett, Nucl. Inst. and Meth. 81, 263 (1970).

(41) G. E. Thomas, D. E. Blatchley and L. M. Bollinger, Nucl. Inst. and Meth. 56 325 (1967).

(42) D. T. Stewart and P. W. Martin, Nucl. Phys. 60, 349 (1964).

(43) N. P. Archer, H. Lycklama and T. J. Kennett, Nucl. Phys. 100A, 33 (1967).

(44) H. J. Fiedler, L. B. Hughes, T. J. Kennett, W. V. Prestwich, and B. J. Wall, Nucl. Inst. and Meth. 40, 229 (1966).

(45) B. J. Wall, Master's Thesis, McMaster University (1966).

(46) M. Strauss, Private Communication, Argonne National Lab., Chicago.

(47) Ibid. 39, P

(48) B. E. Watt, Phys. Rev. 87, 1037 (1952).

(49) J. B. Marion, Nucl. Data 4, 316 (1968).

(50) P. M. Endt and C. Van der Leun, Nucl. Phys. A105, 134 (1967).

(51) E. G. Gibson, K. Battleson and D. K. McDaniels, Phys. Rev. 172, 1004 (1968).

(52) Ibid. 38, P 50.

(53) Ibid. 50, P 313.

(54) J. R. MacDonald, D. F. H. Start, R. Anderson, A. G. Robertson and M. A. Grace, Nucl. Phys. A108, 6 (1968).

(55) Ibid. 49, P 311.

(56) A. R. Poletti, A. D. W. Jones, J. A. Becker and R. E. McDonald, Phys. Rev. 181, 1606 (1969).

(57) Ibid. 50, P 183.

(58) Ibid. 38, P 62.

(59) A. E. Antropov, D. L. Gurnalnik, P. P. Zarubin, B. N. Orlov, A. V. Plavko and B. I. Saprykin, Izv. Akad. Nauk. SSSR, Ser Fiz. 32, 1754 (1968), Bull. Acad. Sci. USSR Phys. Ser. 32, 1616 (1969).

(60) H. Lycklama and T. J. Kennett, Can. J. Phys. 45, 3039 (1967).

(61) L. Nichol, A. H. Colenbrander and T. J. Kennett, Can. J. Phys. 47, 953 (1969).

(62) Ibid. 50, P 107.

(63) Ibid. 38, P 28.

(64) Bergqvist, Biggerstaff, Gibbons and Good, Nuclear Structure Study with Neutrons (Proceedings of the International Conference, Antwerp, July 1965) P 129, edited by M. Neve de Mevergnies, P Van Assche and J. Vervier, North-Holland Publishing Co., Amsterdam (1966).

(65) M. J. Martin, J. A. Harvey and G. G. Slaughter, Proceedings of the Conference on Slow-Neutron-Capture Gamma-ray Spectroscopy, Argonne National Laboratory, Nov. 1966 P. 14.

(66) Ibid. 50, P 26.

(67) Nuclear Data Sheets (A=19), National Research Council, Washington 25, DC.

(68) D. H. White, Bull. Am. Phys. Soc. Ser II, 14, 1214 (1969), and private communication.

(69) F. Ajzenberg-Selove, Nucl. Phys. A152, 51 (1970).

(70) Ibid. 41, P 325.

(71) J. W. Olness, E. K. Warburton, D. E. Alburger and J. A. Becker, Phys. Rev. 139, B512 (1965).

(72) L. C. Northcliffe and R. F. Schilling, Nucl. Data Tables Section A 7 (1970).

(73) L. C. Northcliffe, Ann. Rev. Nucl. Sci. 13, 67 (1963).

(74) R. D. Evans, The Atomic Nucleus, P 646, McGraw-Hill Book Co., New York, Toronto, London (1955).